

Copyright
by
Aale R. Naqvi
2014

**The Dissertation Committee for Aale R. Naqvi Certifies that this is the approved
version of the following dissertation:**

Radar Signature Characterization from Wind Turbine Scattering

Committee:

Hao Ling, Supervisor

Andrea Alu

Mark Hamilton

Mircea Driga

Surya Santoso

Lance Manuel

Radar Signature Characterization from Wind Turbine Scattering

by

Aale R. Naqvi, B.S.; M.S.E.

Dissertation

Presented to the Faculty of the Graduate School of

The University of Texas at Austin

in Partial Fulfillment

of the Requirements

for the Degree of

Doctor of Philosophy

The University of Texas at Austin

May, 2014

To my entire family

Acknowledgements

It is my pleasure to express my gratitude to all the people responsible for the successful completion of my dissertation. First, I would like to express my thanks to my supervisor, Dr. Hao Ling, for overseeing the successful completion of this work. I would also like to thank Dr. Andrea Alu, Dr. Mark Hamilton, Dr. Mircea Driga, Dr. Surya Santoso, and Dr. Lance Manuel for their time in being part of my committee.

I would also like to thank my fellow research group members. I gained a lot through my interactions with Dr. Shobha Sundarram, Dr. Yang Li, Dr. Ickjae Yoon, Dr. Nicholas Whiteloni, Mr. Shang-te Yang, and Mr. Chenchen Li.

Finally, I would like to thank all of my family for all their support. I'm extremely grateful to them for instilling in me a love of knowledge and believing in my ability to accomplish my goals.

AALE NAQVI

The University of Texas at Austin

May 2014

Radar Signature Characterization from Wind Turbine Scattering

Aale R. Naqvi, Ph.D.

The University of Texas at Austin, 2013

Supervisor: Hao Ling

The growth in the number of wind farms has raised significant concerns in the radar community due to their potential interference on radar systems. The motion of the turbine blades creates unwanted Doppler clutter that can interfere in the tracking of moving targets. Large turbine structures can also produce electromagnetic shadows that may make observing objects behind a wind farm difficult. Detailed characterization of the clutter is the first step towards effective mitigation techniques. The goal of this dissertation research is to gain a better understanding of the dynamic radar signatures resulting from scattering by wind turbines. First, the scattering characteristics of turbines in the presence of ground surface are studied. Image theory in conjunction with a shooting-and-bouncing ray code, Ahilo, is used to carry out the dynamic signature simulation. The observed features in the simulation are corroborated with laboratory model measurements. Second, the effects of higher order motions of a turbine undergoing rotation on the radar signatures are investigated and characterized. Mathematical models for the motions are proposed and used to simulate the joint time-frequency and inverse synthetic aperture radar characteristics of the turbine undergoing these motions. The motions are studied for an isolated turbine as well as for a turbine rotating above a ground. Selected motions are corroborated by laboratory model measurements. Next, a method to remove the dynamic clutter produced by wind turbines

is presented. A physics-based basis is constructed to model the radar backscattering from a wind turbine. This basis is used in conjunction with the matching pursuit algorithm to iteratively remove the Doppler clutter due to wind turbines. The algorithm is tested using radar return generated using Ahilo. Finally, radar features of wind turbines are simulated and studied in the HF (high frequency) band. The features are presented in the range-Doppler plane for single as well as arrays of turbines. Doppler aliasing due to the limited pulse repetition frequency of HF radars is examined. Shadowing characteristics of arrays of turbines are simulated and analyzed. Electromagnetic modeling details including effects of thin-wire modeling, non-conducting turbine components, and the presence of a conducting ground surface are discussed.

Table of Contents

List of Figures	x
Chapter 1 Introduction.....	1
Chapter 2 Basic Scattering Phenomenology of a Wind Turbine	11
2.1 Introduction	11
2.1.1 Data Collection and Processing	11
2.2 Doppler Feature Analysis.....	14
2.2.1 1:160 Scaled Model.....	14
2.2.2 3-Arm Wire Model.....	17
2.2.3 Bergey Windpower Turbine	24
2.3 Summary	27
Chapter 3 Doppler Features from Wind Turbines in the Presence of Ground	29
3.1 Introduction	29
3.2 Doppler Feature Analysis.....	30
3.3 Experimental Corroboration.....	36
3.4 Ground Motion	38
3.5 Summary	43
Chapter 4 Time Frequency and ISAR Characteristics of Wind Turbines with Higher Order Motions	45
4.1 Introduction	45
4.2 Motion Models	46
4.3 Turbine JTF Characteristics	50
4.4 Turbine ISAR Characteristics.....	56
4.4.1 Composite ISAR Images-Simulation and Measurement.....	57
4.4.2 Composite ISAR Images with Higher Order Motions	59
4.4 Turbine ISAR Characteristics in the Presence of Ground	64
4.4.1 Higher Order Motions in the Presence of a Stationary Ground.	65

4.4.2 Higher Order Motions in the Presence of Moving Ground	68
4.5 Summary	70
Chapter 5 A Signal Filtering Technique to Remove Doppler Clutter Caused by Wind Turbines	72
5.1 Introduction	72
5.2 Basis Parameterization Via Matching Pursuit	73
5.3 MP Using Point Scatterer Training Data	75
5.4 MP Using Chirplet Basis.....	78
5.5 Ahilo Simulations	81
5.6 Basis Construction	84
5.7 Results and Discussion.....	86
5.8 Summary	91
Chapter 6 Radar Features of Wind Turbines at HF Frequency Region	93
6.1 Introduction	93
6.2 Range-Doppler Features.....	94
6.3 Doppler Aliasing.....	100
6.4 Electromagnetic Shadowing.....	102
6.5 Modeling Discussion	105
6.6 Summary	112
Chapter 7 Conclusions and Future Work	113
7.1 Conclusions	113
7.2 Future Work	115
References.....	116
Vita	123

List of Figures

Figure 1.1:	Pictorial representation of electromagnetic shadowing and Doppler clutter produced by wind turbines.....	2
Figure 2.1:	Graphical illustration of the discrete short time Fourier transform .	13
Figure 2.2:	1:160 scaled model turbine measurements. (a) Photo of the model turbine. (b) Backscattered spectrogram after STFT processing	15
Figure 2.3:	Mechanism giving rise to positive and negative flash for clock wise rotating blades. (a) positive flash. (b) negative flash	15
Figure 2.4:	AFRL simulated and measurement spectrograms [20]. The lengths of the blade and tower are 34 m and 65 m, respectively. Radar frequency is 1.5 GHz. (a) Measured result. (b) Simulated using Xpatch. (c) Measurement showing possible multiple interactions taking place in the blades.....	16
Figure 2.5:	The 3-arm wire model.....	17
Figure 2.6:	Single-arm wire model. (a) NEC-simulated backscattering. (b) NEC-simulated forward scattering. (c) Measured backscattering. (d) Measured forward scattering	18
Figure 2.7:	Illustration of Doppler-inducing mechanisms seen in Figure 2.6. (a) Backscattering mechanism (i). (b) Forward scattering mechanisms (ii) and (iii)	19
Figure 2.8:	In the absence of multiple interactions within the target, the path length change is 0 and therefore causes no Doppler	20
Figure 2.9:	Pictorial representation showing the specular point walk as the blade rotates leading to tilted flashes in the backscattering spectrograms	21

Figure 2.10: 3-arm wire model. (a) NEC-simulated backscattering. (b) NEC-simulated forward scattering. (c) Measured backscattering. (d) Measured forward scattering	23
Figure 2.11: Illustration of additional Doppler-inducing mechanisms seen in Figure 2.10. (a) Backscattering mechanisms (i) and (ii). (b) Forward scattering mechanisms (iii) and (iv).....	24
Figure 2.12: (a) Photo of the Bergey Windpower turbine. (b) Measured backscattering. (c) Measured forward scattering.....	25
Figure 2.13: Blade shape effect based on a simple triangular blade model. (a) θ degrees before a blade flash occurs. (b) After 60 degrees of rotation. (c) Resulting irregular blade flashes as shown in black	27
Figure 3.1: Pictorial representation of airborne radar illuminating ground and turbines	29
Figure 3.2: NEC simulation for a rotating wire above an infinite ground plane. (a) stationary ground. (b) moving ground	31
Figure 3.3: Turbine CAD model. (b) Ground interactions.....	32
Figure 3.4: CAD model of turbine with its image	33
Figure 3.5: Spectrogram from turbine backscattering. (a) Without ground. (b) In the presence of ground.....	34
Figure 3.6: Image theory applied to simulate and explain the observed flashes. (a) Direct return flash. (b) Single-ground-bounce flash. (c) Double-ground-bounce flash.....	36
Figure 3.7: (a) Measurement setup. Spectrogram from measurement data. (a) Without ground. (b) In the presence of ground	38

Figure 3.8: Fresnel zone comparison. (a). stationary ground. (b) larger ocean wavelength. (c) smaller ocean wavelength.....	41
Figure 3.9: Backscattering from a turbine in the presence of a sinusoidally vibrating ground. (a) Spectrogram from backscattered data. (b) Single-ground-bounce return corresponding to track (ii) in (a). (c) Double-ground-bounce return corresponding to track (iii) in (a).....	44
Figure 4.1: Pictorial representation of the blade motions. (a) uniform rotation motion. (b) in-plane vibrations. (c) out-of-plane vibrations. (d) blade flexing. (e) tower vibration.....	50
Figure 4.2: Point scatterer simulated JTF characteristics of the turbine motion. (a) uniform circular motion. (b) in-plane vibrations. (c) out of plane vibrations. (d) blade flexing. (e) tower vibrations	52
Figure 4.3: Measurement results. (a) Uniformly rotating turbine. (b) With in-plane vibrations injected.....	55
Figure 4.4: ISAR images of turbine at various blade angular positions. (a), (c), and (e) are simulated using point scatterer model. (a) Positive flash. (c) Blades in a non-flashing position. (e) Negative flash. (g) Composite image. (b), (d), (f), and (h) are corresponding measured results	58
Figure 4.5: Composite ISAR images of turbine. (a) Uniform circular rotation. (b) In-plane vibrations. (c) Out-of-plane vibrations. (d) Blade flexing. (e) Tower vibrations	60
Figure 4.6: Measured composite ISAR image. (a) Uniformly rotating turbine. (b) With in-plane vibrations injected.....	61
Figure 4.7: Measurement set-up to cause physical in-plane vibrations	62

Figure 4.8: Measured ISAR images of turbine rotating clockwise with aluminum bulbs on blades that undergoes physical in-plane vibrations. (a) A snapshot before the turbine motion is impeded. (b) A snapshot at the onset of the impedance. (c) Undergoing in-plane vibrations that shows up as blade ghosts due to large disturbance relative to the imaging window. (d) After the blades go back to rotating in a uniform circle..... 63

Figure 4.9: Composite ISAR images of turbine in the presence of ground. (a) Uniform circular rotation. (b) In-plane vibrations. (c) Out-of-plane vibrations. (d) Blade flexing. (e) Tower vibrations 66

Figure 4.10: Measured composite ISAR images of turbine in presence of ground. (a) Measurement set up. (b) Uniform circular rotation. (b) In-plane vibrations injected..... 67

Figure 4.11: Composite ISAR images of turbine in the presence of moving ground. (a) uniform circular rotation. (b) in-plane vibrations. (c) out-of-plane vibrations. (d) blade flexing. (e) tower vibrations 69

Figure 5.1: Spectrogram for four turbines with a weak target moving at constant velocity 75

Figure 5.2: MP using point scatterer basis on itself. Residual after: (a) 1st iteration. (b) 2nd iteration. (c) 3rd iteration. (d) 4th iteration. (e) 10th iteration. (f) Residual energy as a function of iteration 77

Figure 5.3: Simulated signals. (a) Point scatterer basis. (b) periodic chirplet.... 78

Figure 5.4: Iterative subtraction using chirplet basis. (a) 1st residual. (b) 10th residual. (c) 50th residual. (d) 100th residual. (e) Residual magnitude vs. residual iteration..... 81

Figure 5.5: Simulation of a single turbine rotating at 12 rpm. (a) Turbine CAD model. (b) Spectrogram of the backscattered signal with WGN	83
Figure 5.6: Simulated spectrogram of backscattering from a cluster of 10 turbines. Eight of the turbines are rotating at 12 rpm and the other two at 10 rpm	84
Figure 5.7: Time-frequency characteristics of the turbine basis	86
Figure 5.8: Single turbine backscattering, after high-pass filtering. (a) Ahilo data. (b) Turbine basis	86
Figure 5.9: Signal filtering applied to the backscattering from a single turbine. (a) Spectrogram after MP filtering. (b) Signal energy as a function of iteration number	87
Figure 5.10: Signal filtering applied to the backscattering from a cluster of ten turbines. (a) Original signal after high pass filtering. (b) 1 st residual. (c) 4 th residual. (d) 9 th residual. (e) 25 th residual. (f) Signal energy as a function of iteration number	89
Figure 5.11: Introducing blade shape into the point scatterer basis. (a) Linearly shaped blade. (b) Curved blades. (c) Triangular shaped blade	91
Figure 6.1: Radar features of a wind turbine rotating above an infinite ground plane. The turbine rotation speed is 15rpm and the radar frequency range is between 12 and 14MHz. (a) Simulation set-up using a thin-wire model. (b) Range-Doppler image	95
Figure 6.2: Radar features of a 3x1 wind turbine array. (a) Simulation set-up using thin-wire models. (b) Range-Doppler image	96
Figure 6.3: Radar features of a 1x3 wind turbine array. (a) Simulation set-up using thin-wire models. (b) Range-Doppler image	97

Figure 6.4: Radar features of a 3x3 wind turbine array. (a) Simulation set-up using thin-wire models. (b) Range-Doppler image under edge-on incidence. (c) Range-Doppler image under 45° oblique incidence.....	99
Figure 6.5: Doppler spectra of a rotating turbine at 13MHz. (a) 13rpm rotation speed sampled at 30Hz. (b) 13rpm rotation speed sampled at 2Hz. (c) 13.1rpm sampled at 2Hz. (d) 13.2rpm sampled at 2Hz. (e) 13.333rpm sampled at 2Hz.....	101
Figure 6.6: Shadowing effect of wind turbines. (a) Field without wind turbines. (b) Field with a 3x1 wind turbine array. (c) Difference in field strength with and without the turbines	103
Figure 6.7: Shadowing effect of wind turbines. (a) Field without wind turbines. (b) Field with a 3x3 wind turbine array. (c) Difference in field strength with and without the turbines	104
Figure 6.8: Shadowing effect of wind turbines under 45° oblique incidence. (a) Field without wind turbines. (b) Field with a 3x3 wind turbine array. (c) Difference in field strength with and without the turbines	104
Figure 6.9: Comparison between the full surface-mesh model and the approximate thin-wire model computed using FEKO. The blades and tower of the model have a radius of 0.26m. (a) Range profile from the surface-mesh model. (b) Range profile from the thin-wire model. (c) Range-Doppler plot from the surface-mesh model. (d) Range-Doppler plot from the thin-wire model.....	106
Figure 6.10: Effect of increasing the cylinder radius in the surface-mesh model on the range profile of a 90m tower. The frequency range is from 12 to 14MHz	107

Figure 6.11: Effect of decreasing the wire radius in the thin-wire model on the range profile of a 90m tower. The frequency range is from 12 to 14MHz108

Figure 6.12: Effect of turbine material on the RCS. (a) Dielectric cylinder frequency response. (b) PEC cylinder frequency response.(c) Dielectric cylinder range profile. (d) PEC cylinder range profile109

Figure 6.13: Effect of the conducting ground surface on the turbine RCS. (a) Possible ground bounce mechanisms. (b) RCS versus range and blade angle in the presence of ground. (c) RCS versus range and blade angle without ground. (d) Difference between the with-ground case and four times the without ground case111

Chapter 1: Introduction

Wind energy is becoming an increasingly attractive option in today's world that is searching for alternative energy sources to reduce greenhouse gas emission. The world's wind energy supply has steadily increased in the past several years. With increasing interest in the wind energy arena, the number of wind farms worldwide can be expected to increase dramatically in the near future. This clean energy source can provide a solution to a potential future energy crisis and can possibly lead to cleaner air for current and future generations. With these benefits however, this new technology has also been observed to hinder performance of existing communications and radar systems.

The first concerns regarding the effects of wind turbine on electromagnetic waves were raised by the television community in the late 1970s. Sengupta and Senior [1, 2] found, using in-situ measurement and theoretical calculations, that the rotation of the wind turbine blades can cause amplitude modulation of the received electromagnetic signal. The effect of this modulation is to distort the received signal and is greater on antennas situated close to wind turbines. The modulation is more prominent at higher frequencies, and therefore is degrading to the signal at UHF and VHF frequencies. More recently in the early 2000s, Salema et. al [3, 4] showed using theoretical analysis that tower diffraction causes attenuation in the received antenna signal that does not exceed 3dB beyond 100 m away from the tower at 100 MHz and the attenuation increases with frequency. Furthermore, they set criteria for clearance distance that can minimize TV

signal interference. Recently the effects of the wind turbines situated in the near field of UHF band radar systems were studied; the motion of the blades was found to have a degrading effect on OFDM (orthogonal frequency-division multiplexing) signals [5]. Also, electromagnetic interference on communication systems due to turbine's electronic components has been brought up in the literature recently [6-8].

The growth in the number of wind farms has also raised significant concerns in the radar community. The large size of wind turbines and relative spacing may potentially cause deep electromagnetic shadows behind wind farms. These effects may potentially hinder the ability of air traffic control and air defense radars in detecting objects flying inside the shadow region, and have been investigated in [9-24]. Moreover, the rotation of the turbine blades can produce Doppler frequencies of more than 2.5 kHz in the C-band and higher frequencies, which can coincide with the Doppler returns of aircraft.

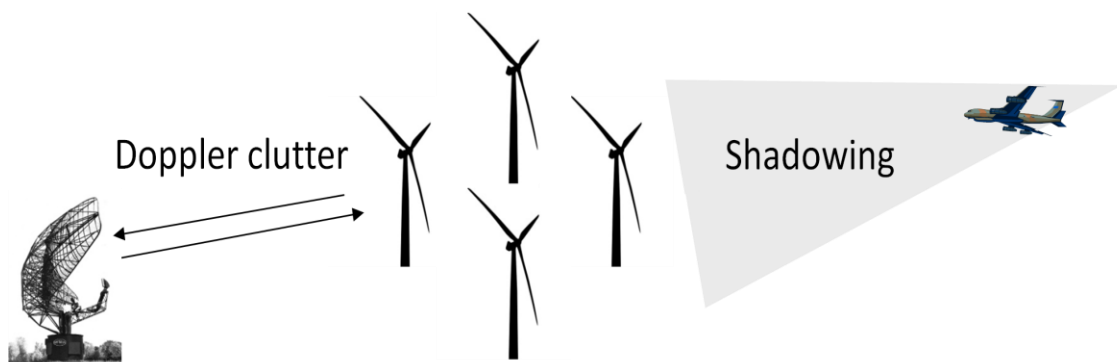


Figure 1.1: Pictorial representation of electromagnetic shadowing and Doppler clutter produced by wind turbines.

Radar clutter from wind farms can make differentiating the Doppler from the turbine blades and an aircraft a difficult task for air traffic control and air defense radars as demonstrated in Figure 1.1.

Recently, wind farms have also caused concerns in the weather radar community. The best sites for both weather radars and wind turbines are at high altitudes and in unobstructed terrain. As a result, established weather radar sites are also potentially optimal locations for wind farms. Due to the wind speeds generated close to the wind farms, weather signatures close to the wind farms resemble storms. The wind farm clutter can also adversely affect the weather radar's internal processing algorithm. Maintaining large distances between the radars and turbines keeping the radar line-of-sight clear have been suggested to potentially alleviate some of the adverse affects on radars [25-33].

Another class of radars adversely affected by the presence of wind turbines is coastal monitoring radars. Coastal monitoring radars collect data from the moving ocean surface to map ocean currents [34, 35]. However, offshore wind farms situated in coastal waters could interfere with the intensity of the key signals features in ocean data. In particular, the longer turbine blades make it difficult to isolate the ocean Doppler features from the ones produced by wind turbines. Typically coastal radars operate in the HF (high frequency) region. As a result, the turbine size is on the order of the radar wavelength. This can produce new scattering features that are not present in turbine signatures in the microwave frequency range [36, 37].

Traditional radar clutter mitigation techniques are not always effective in alleviating the problem caused by wind farms [6, 12]. The available techniques include amplitude threshold, range-azimuth gating, constant false alarm rate (CFAR) filtering, Doppler discrimination, moving target indication (MTI), and automatic tracking. Amplitude threshold has traditionally been used to increase the threshold of detection in order to eliminate small targets such as birds and rain. Amplitude threshold technique is not applicable to the case of turbines due to their large size and therefore large radar return. Range-azimuth gating completely suppresses returns from selected range-azimuth cells. This results in holes on the radar map and targets moving through these cells can go undetected as a result. In CFAR filtering, if the largest return from a range-azimuth cell is greater in an antenna sweep compared to the previous sweep, the threshold is increased. However, this technique runs into the same difficulties described for amplitude threshold. Doppler discrimination processes out velocity of unwanted targets; however, flying aircraft has velocities comparable to the blades of the turbine thus reducing the effectiveness of this approach. MTI compares the phase of several consecutive pulses and can be used to filter out static clutter only. Automatic tracking displays only tracks meeting specified tracking criteria and but encounters problems due to a wide range of the velocities that turbine blades can have. The mitigation of turbine clutter in real-world setting is further complicated by the number of parameters that can potentially affect radar signal propagation through a farm. The radar signal may be affected by the turbine's blade yaw angle relative to the radar, the blade pitch, the material used in the making of turbines, spacing between adjacent turbines, the local

terrain, and the radar antenna pattern, thus making it very difficult to develop a universally applicable methodology for mitigating the effects of potential interference between wind farms and radar.

A number of in-situ studies have been performed in UK as well as US to analyze the effects of wind farms in tracking a flying target around wind farms. The studies were commissioned due to an increase in the number of farms built and commissioned in the 1990s and early 2000s. The first recorded trial to analyze the potential impacts of a wind farm was conducted by UK Ministry of Defence (MoD) in 1994 [12, 13]. The study analyzed the impact of a wind farm situated about 7 km away in the line-of-sight of the radar of an air traffic control (ATC) radar. The study involved flying a helicopter over and around a wind farm and concluded that normal MTI based techniques are unable to suppress the turbine response, which appears as valid targets on the radar display. As a result, MoD decided that all wind farm proposals falling within 60% of a radar's range must be consulted before construction. Due to the stringent restrictions placed on the locations of wind farms, more tests were carried out in 2004 that flew aircrafts in a wind farm's vicinity [12]. The first test utilized air defense radar for testing. The tests found that the primary radar recorded false returns and the quality of the primary returns was degraded. The tests also found missing tracks that were only detected through a high reliance on secondary surveillance radar (SSR), which is an active transponder system that sends an interrogating signal and expects a known "friendly" response from an aircraft in return. The ministry attributed the missing SSR tracks to the shadows created by wind farms. Also, the study found that these effects were independent of the altitude

of the aircraft. MoD also carried out tests on an ATC radar and observed shadowing effects as well as significant clutter using the same methodologies used for the defense radar.

US commissioned the first study to analyze turbine interference in 2002 at King Mountain, TX on Air Route Surveillance Radar-4 (ARSR-4) [9]. Unaware of the results of the UK 1994 trials, the flying targets were located too far from the farm, between 30-155 nmi, to have any significant shadowing or clutter interference. The study erroneously concluded that wind farms have no degrading effects on radar performance. Later analysis revealed the error and a second set of trials was carried out at Tyler, MN in 2004. The test measured the performance of an ARSR-2 radar situated very close to a wind farm. The wind turbines lied along a ridgeline in the NW and SE direction spanning a distance of 60 nmi. The radar's position bifurcated the wind farm and the closest wind turbine in these trials was situated at a distance of 0.75 nmi from the radar. The tests flew aircraft along the NE direction and tracked the target using both primary and SSR radars. The tests found significant degradation of primary radar signal when the target was close to the wind farm.

The results of UK and US trials complement each other; however, they only provided evidence in favor of the adverse effects of wind farms on radars. The first comprehensive study to computationally model the scattering from a wind turbine and perform scale model and field measurements was conducted by QinetiQ in the UK [17]. Their findings were corroborated by a later comprehensive investigation carried out by the Air Force Research Lab (AFRL) in the US, in a study commissioned by the US

Congress in 2006 [18-21]. AFRL collected in-situ measurements of 1.5MW turbines on a wind farm in Fenner, NY. In their work, AFRL successfully established the validity of the computational electromagnetics (CEM) code, Xpatch, to model the returned signal from wind farms in order to lessen the dependence on costly field measurements. The most significant backscattering feature was found to be the blade flashes when the blades are oriented perpendicular to the radar line-of-sight. At all other positions of the blades, the blade tip was observed to trace a sinusoid in the spectrogram as it rotated. These results are quite similar to helicopter rotor blades, whose Doppler characteristics have been well studied previously [38-43]. In addition to these prominent features, other Doppler tracks were also observed in the data. They are potentially caused by higher-order multiple interactions, but were not fully explained. Furthermore, only the backscattered data were taken. The transmission blockage effect due to the wind turbine was not characterized in the study, which would have required a one-way forward scattering measurement with the transmitter and receiver being positioned on the two sides of the turbine.

A number of turbine clutter mitigation techniques have been proposed in the literature [44-62]. Adjusting the spacing of the turbines in order to minimize interference by turbine is suggested in [44]. Radar absorbent material coating the turbine is proposed in [45-48]. RCS reduction by controlling the geometry of the turbine components is presented by [47]. Addition of components for active cancellation of the turbine clutter as well as gap filler radars to maintain visibility in the shadow region are discussed in [49-51]. Furthermore, various signal processing techniques including interpolation,

statistical, and replicating the turbine signatures mathematically for mitigation purposes have been put forward by [52-62]. Although various mitigation measures have been proposed to date, they are currently in their nascent phases. No single measure or a combination thereof has been implemented in radar systems as a definitive solution to the problems caused by wind turbines. Understanding the scattering characteristics in detail is the first step towards effective improvements to the proposed and unexplored mitigation techniques.

The goal of this dissertation is to broaden the understanding of the radar scattering characteristics of wind turbines. The insights into the nature of the scattering characteristics can lead to better clutter removal techniques. The scattering physics can also serve as a guide to detect irregularities in a turbine's blade motion. In order to realize the research goal, four objectives are established. The first objective is to study scattering characteristics of turbines in more complex environments. The second objective is to extend the phenomenological analysis of turbine scattering characteristics by studying higher order turbine motions that may be present due to irregularities in turbine motion. The third objective is to develop a method to remove the clutter produced by wind turbines. Finally, the fourth objective is to investigate the HF frequency scattering characteristics of wind turbines.

The remainder of the dissertation is organized as follows. In Chapter 2, the basic scattering phenomenology of a wind turbine is reviewed [63]. The time-frequency features of both forward and backscattering characteristics of wind turbines are presented and explained. In Chapter 3, we first extend the phenomenological study of isolated

turbines in Chapter 2 to address turbine scattering in the presence of ground [64]. Ground bounce interactions create additional features not present in the case of free-standing turbines. Both the cases of stationary and moving ground are studied. The latter may arise in the scenario where the turbines are situated offshore.

In Chapter 4, the signatures of rotating turbines undergoing higher order motions are examined [65]. Four types of higher order motions are studied including in-plane, out-of-plane, blade flexing, and tower vibration motions. Motion models are proposed for each of type of motions. The time-frequency and inverse synthetic aperture radar (ISAR) characteristics of the motions are simulated. The case of a free-standing and that of a turbine in the presence of ground are studied. Selected simulated motions are corroborated by measurements.

Having studied the turbine scattering characteristics in detail, a backscattering clutter removal technique [66] is developed in Chapter 5. A set of basis functions resembling backscattering from turbine blades is developed and iteratively projected onto the received radar signal using the matching pursuit algorithm [25] to remove turbine clutter. The effectiveness of the procedure is tested using simulated radar data from the high-frequency electromagnetic code Ahilo [26].

Chapter 6 presents the phenomenological study of turbine scattering at HF frequencies [67]. The scattering features are presented in the range-Doppler plane for a single as well as arrays of turbines. We analyze Doppler aliasing caused by the low pulse repetition frequency (PRF) of HF radars. Shadowing characteristics of arrays of static

turbines are studied. The electromagnetic modeling methodology of the turbines is addressed.

Finally, Chapter 7 presents the conclusions of the work performed. Furthermore, future research directions based on this work are proposed.

Chapter 2: Basic Scattering Phenomenology of a Wind Turbine

2.1 INTRODUCTION

In this chapter, the basic radar scattering phenomenology of a wind turbine is reviewed. The review is based on work done to characterize turbine features originally reported in [63]. In contrast with the in-situ measurements in [18-21], Doppler features are detailed and discussed through a series of indoor measurements on scaled model turbines. Both backscattered and forward measurement scattered data are analyzed from the wind turbine models undergoing rotation. The models include a 1:160 scale model turbine, a 3-arm wire model, and a small wind turbine from Bergey Windpower with 2' blades. Detailed accounts of the physics behind the observed phenomena including multiple scattering, near field effects, and blade shape effects are presented. First, the scattering features from the 1:160 scaled model turbine is discussed and it is shown that the scaled model measurements capture the gross Doppler features observed in [18-21]. Next, a larger 3-arm wire model is constructed to provide better resolution in detecting higher order interactions and additional phenomenology in the scattered data. Finally, the wind turbine from Bergey Windpower shows interesting scattering features arising due to the unique shape of the blades.

2.1.1 DATA COLLECTION AND PROCESSING

The process of measurement collection was carried out as follows. A vector network analyzer (*Agilent N5230A*) was used to collect raw measurement data in

continuous wave (CW) mode at 14 GHz. For the 3-arm wire model and the Bergey Windpower turbine, the data were collected for 65.5 seconds, which corresponds to one rotational period of our turn-table, while the sampling rate was set at 22Hz. The data were sampled for a total of 1441 points. The 1:160 scaled model turbine was driven by a motor with a period of 1.67 seconds. Therefore, data were collected for 5 seconds at a sampling rate of 160 Hz which corresponds to 800 total sampled points. The intermediate frequency (IF) bandwidth was set at 200 Hz for the 1:160 model and 30 Hz for the other two models. The instrument dictates that the IF bandwidth must be greater than the pulse repetition frequency. However, higher IF bandwidth results in higher noise level in the collected data. Therefore it was set at the minimum values allowed. Two horn antennas, separated by 4m, were set facing each other and the turbine under test was placed in between, 2 m from each horn. Both S11 and S21 parameters were measured for each turbine model. Background subtraction was also performed for each S-parameter to reduce the effects of reflection within the horn and direct coupling between the horns, which give rise to a very strong zero-Doppler component. The complex scattering data for each parameter were processed using the short-time Fourier transform (STFT).

Unlike with the conventional Fourier transform, the STFT is a good tool to capture the time-varying Doppler characteristics of a signal. Eq. 2.1 gives the mathematical representation of the STFT:

$$STFT\{x(t)\} = X(\tau, \omega) = \int x(t)w(t - \tau)e^{-j\omega t} dt \quad (\text{eq. 2.1})$$

The short-time Fourier transform takes the Fourier transform of the original time domain signal, $x(t)$, multiplied with a sliding finite window function, $w(t)$.

For the discrete time case, the continuous independent variables in (eq. 2.1) are replaced with discrete indexes as evident in (eq. 2.2):

$$STFT\{x[n]\} = X(m, \omega) = \sum x[n]w[n - m]e^{-j\omega n} \quad (\text{eq. 2.2})$$

The discrete form of the STFT takes Fourier transform of a short-time segment of a signal and assigns the magnitude of the result to the time value corresponding to the center of the window function. This procedure is shown in Figure 2.1,

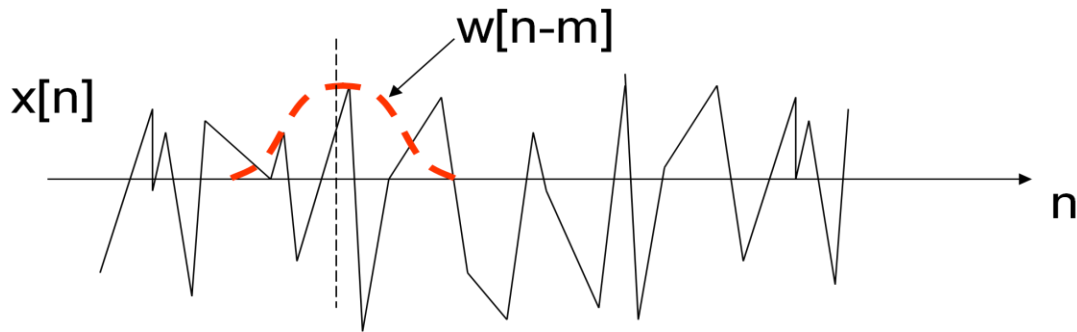


Figure 2.1: Graphical illustration of the discrete short time Fourier transform

where $x[n]$ is the discretized signal. The window function shown in the red dashed curve determines the amount of signal being sampled and the resulting Fourier transform of the segment is assigned to the time value at the black dashed line. The window function is next slid to the right and this process is repeated. Adjacent windows may overlap in the sliding. This process is repeated until the STFT of the complete signal is obtained. The magnitude of the resulting function is referred to as the spectrogram. The spectrogram is plotted on a 2-D time-frequency plot to reveal the Doppler characteristics of the signal as

a function of time. A large time window leads to worse time resolution but better resolution along the frequency dimension. This relationship between time and frequency resolution is swapped for the case of small time window. The size of the time window should be roughly comparable to the periodicity of the signal in order to capture the instantaneous time-varying frequency characteristics of the signal. Under this consideration, a time window of 0.4 second is used to process the 1:160 scaled model turbines and a 6-second window was used for the other two models.

2.2 DOPPLER FEATURE ANALYSIS

2.2.1 1:160 Scaled Model

Figure 2.2(a) shows the 1:160 scaled model turbine (Model Power No. 1583). Each blade is 12 cm in length. The turbine was covered with aluminum tape during the measurement to enhance the strength of the received signal. Figure 2.2(b) shows the resulting spectrogram from the measured backscattered data at 90° yaw angle (edge-on incidence). Clearly seen are the blade flashes that occur when a blade is perpendicular to the radar line-of-sight and occur at every 60° turn of the turbine. The flashes alternate between positive Doppler (as a blade moves toward the radar) and negative Doppler (when the next blade recedes away from the radar). In addition, a set of weaker, sinusoidal Doppler tracks can be vaguely observed. They are due to scattering from the

blade tips and are labeled as “tip halo” in the figure.

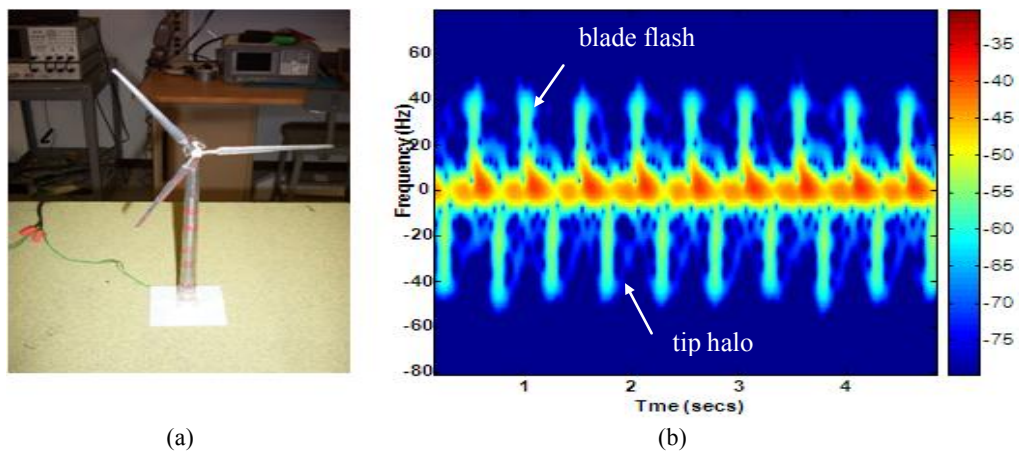


Figure 2.2: 1:160 scaled model turbine measurements. (a) Photo of the model turbine. (b) Backscattered spectrogram after STFT processing.

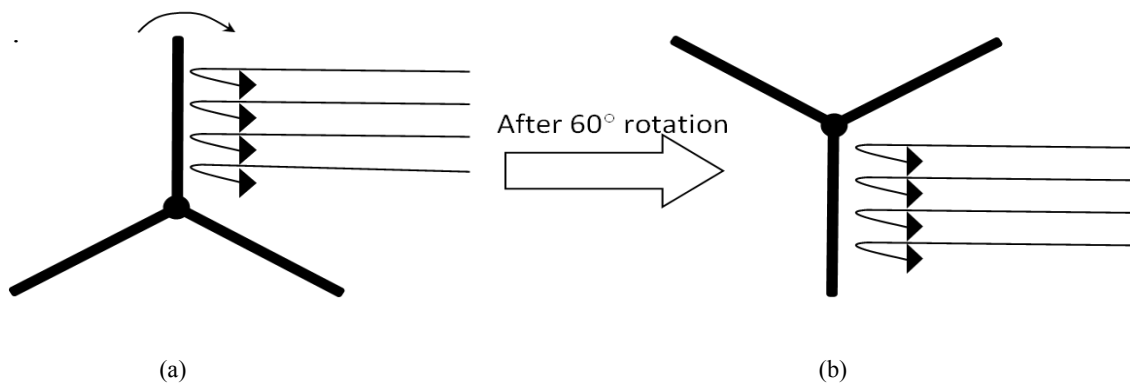


Figure 2.3: Mechanism giving rise to positive and negative flash for clock wise rotating blades. (a) positive flash. (b) negative flash.

Figure 2.3(a) and (b) respectively describe the mechanism that give rise to the positive and negative flash for clock wise rotating blades. It should be pointed out that, since the

model measurement was conducted at 14GHz for the 1:160 scaled model, the results here should correspond to a real turbine at only $14\text{GHz}/160=0.0875\text{GHz}$.

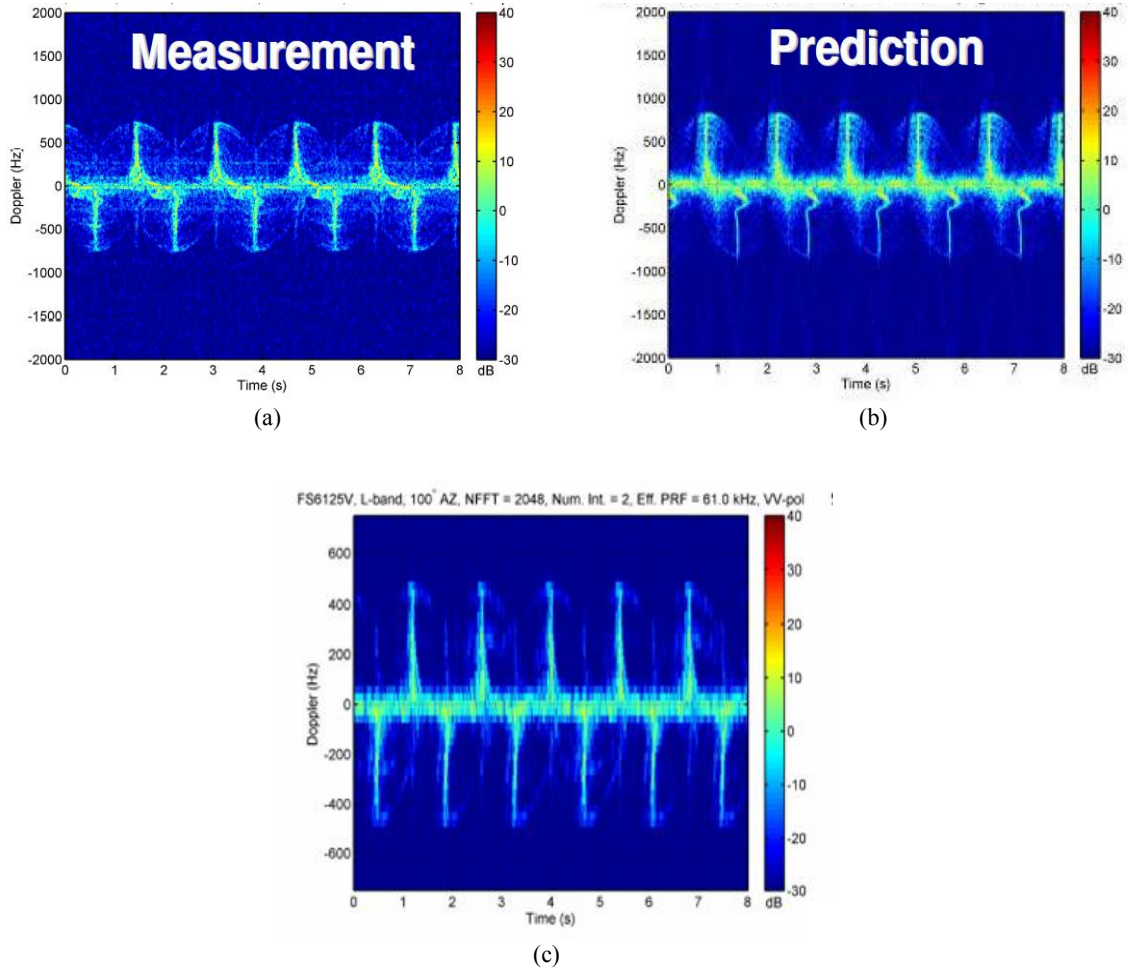


Figure 2.4: AFRL simulated and measurement spectrograms [20]. The lengths of the blade and tower are 34 m and 65 m, respectively. Radar frequency is 1.5 GHz. (a) Measured result. (b) Simulated using Xpatch. (c) Measurement showing possible multiple interactions taking place in the blades.

Nevertheless, when compared to the data from a full-scale 1.5 MW turbine collected between 1 to 10GHz in [20], the same key features are observed. Figure 2.4 shows spectrograms at 1.5GHz acquired by AFRL from their Xpatch simulations and in-situ measurement data from Fenner, NY. Figure 2.4(a) is the spectrogram acquired using measurement data while Figure 2.4(b) is the simulated using Xpatch. Figure 2.4(c) shows a measured case which shows a sinusoidal track that is in phase with that of the tip halo but at half the maximum Doppler. The new track is possibly due to multiple scattering effects but was not explained in the study.

2.2.2 3-Arm Wire Model

Next, the Doppler features of a 3-arm wire model that is 5 times longer than the 1:160 scaled model are discussed in detail.

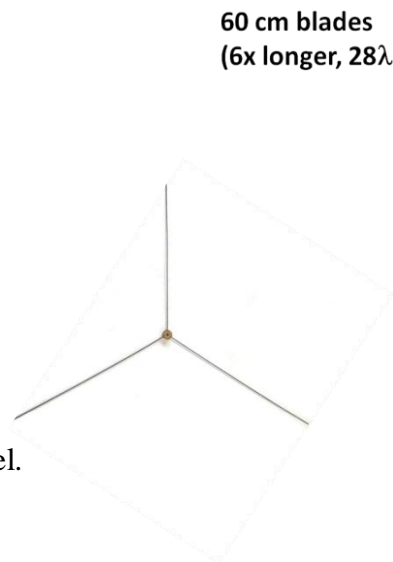


Figure 2.5: The 3-arm wire model.

The 3-arm wire model is shown in Figure 2.5. While the structure is quite simplistic, its scattering can be examined in closer detail by building up the structure one wire arm at a time. Furthermore, the measurement results can be verified through simulations using a

thin-wire modeling code such as the Numerical Electromagnetics Code (NEC). The simulations were performed with the same settings as described for the measurements and were processed in the same manner as well. We start by reviewing the scattered data from a single blade. Figures 2.6(a) and 2.6(b) show the spectrograms from the backscattered and forward scattered data simulated using NEC. Figures 2.6(c) and 2.6(d) are the corresponding measured results.

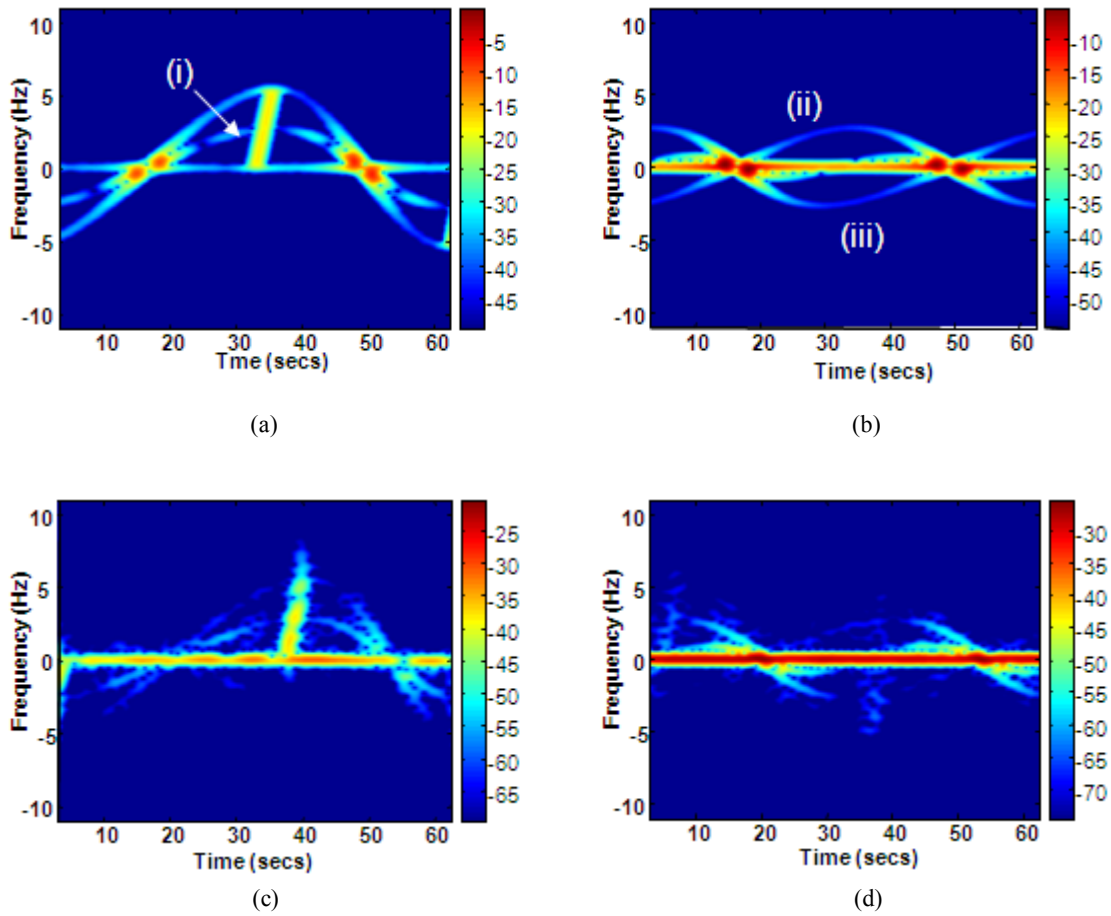


Figure 2.6: Single-arm wire model. (a) NEC-simulated backscattering. (b) NEC-simulated forward scattering. (c) Measured backscattering. (d) Measured forward

scattering.

The simulation and measurement results are plotted over the same dynamic range, although the absolute level of the measurements was not calibrated. Several new features are noted in addition to the blade flashes and tip halos discussed previously. First, the backscattered spectrogram in Figure 2.6(a) contains an additional sinusoid track that is in phase with the tip halo (labeled as (i)). This additional track is due to a traveling wave along the wire from the tip to the hub, and vice versa, as illustrated in Figure 2.7(a).

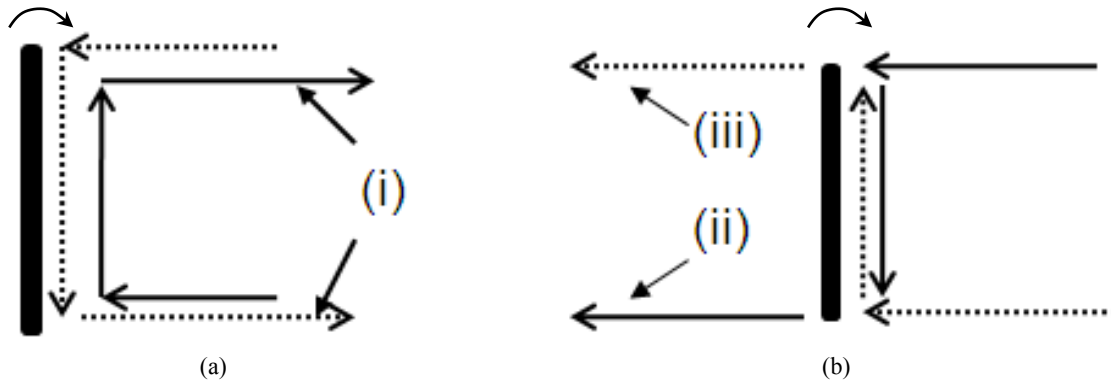


Figure 2.7: Illustration of Doppler-inducing mechanisms seen in Figure 2.6. (a) Backscattering mechanism (i). (b) Forward scattering mechanisms (ii) and (iii).

The blade in Figure 2.7(a) rotates clock-wise and the bottom end of the blade is the center of rotation. Therefore, the two traveling waves along the wire in Figure 2.7(a) experience a path length change versus time that is only half as large as the direct scattering due to the top tip. Hence this interaction results in a Doppler track with a maximum Doppler shift equaling half that of the tip halo.

For the forward scattering case, the sinusoidal tracks labeled (ii) and (iii) in Figure 2.6(b) are the results of the multiple interactions illustrated in Figure 2.7(b). In the interaction labeled as (ii), the wave experiences a decrease in path length as a function of time since the top tip moves toward the transmitter. However, in traveling down to the base of the wire and toward the receiver, no additional path length change is encountered. Therefore, this interaction gives rise to a sinusoid that has a positive Doppler shift with maximum equal to half that from the tip halo backscattering. The case labeled as (iii) Figure 2.7(b) gives rise to a negative sinusoidal peak since the wave experiences an increase in path length as a function of time as it travels from the top tip to the receiver. While the Doppler features in backscattering arise from both single and multiple scattering, forward Doppler can only result from multiple scattering interactions. Any single scattering phenomenon does not cause any path length change and therefore will result in only zero Doppler contribution in the forward direction, as illustrated in Figure 2.8.



Figure 2.8: In the absence of multiple interactions within the target, the path length change is 0 and therefore causes no Doppler.

Lastly, it is observed that the blade flashes in the backscattering data in Figures 2.6(a) and 2.6(c) are tilted. In this case, the NEC simulation is carried out with a near-field source and receiver. As a result, the specular reflection occurs at different times for different points on the blade, as shown in Figure 2.9, which leads to the slanted shape of the flashes.

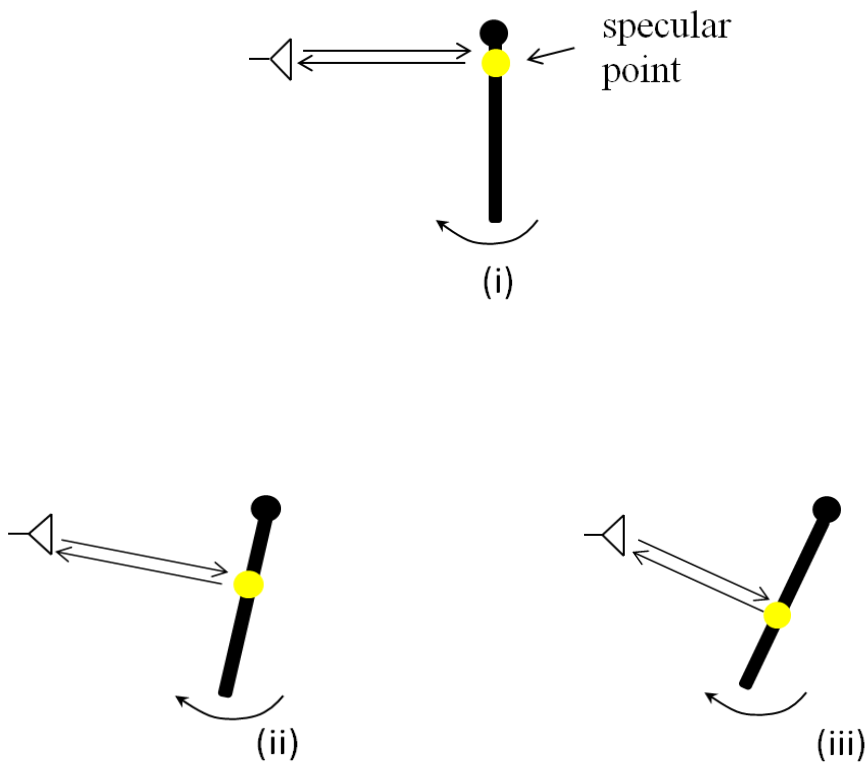


Figure 2.9: Pictorial representation showing the specular point walk as the blade rotates leading to tilted flashes in the backscattering spectrograms.

Near field effect is also the reason behind the sinusoidal Doppler tracks in the forward scattering (features (ii) and (iii) in Figure 2.6(b)) not being exactly 180° out of phase.

Indeed, for a plane wave excitation the blade flashes become straightened and the forward Doppler tracks are perfect sinusoids with 180° phase difference.

The spectrograms of the backscattered and forward scattered data for the complete 3-arm wire model are shown in Figure 2.10. Figures 2.10(a) and 2.10(b) show the spectrograms from respectively the backscattered and forward scattered data simulated using NEC. Figure 2.10(a) shows that in addition to the intra-blade backscattering interaction seen for a single blade, we also observe an additional sinusoidal track, whose maximum Doppler value is labeled (i) in Figure 2.10(a). Figure 2.11(a) shows the turbine position at which this track peaks and the mechanism giving rise to it is illustrated. Figure 2.11(a) also explains why this track peaks on the opposite side of the blade flash. The two blades involved in the interaction are at 30° to the horizontal, hence the maximum Doppler value of v/λ . The mechanism behind the track labeled (ii) in Figure 2.10(a) is explained in Figure 2.11(a) and has already been discussed.

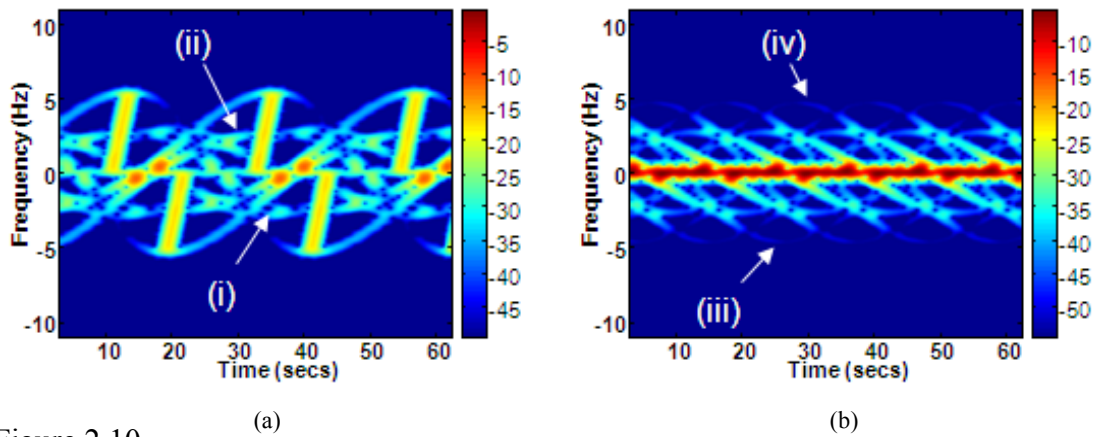


Figure 2.10

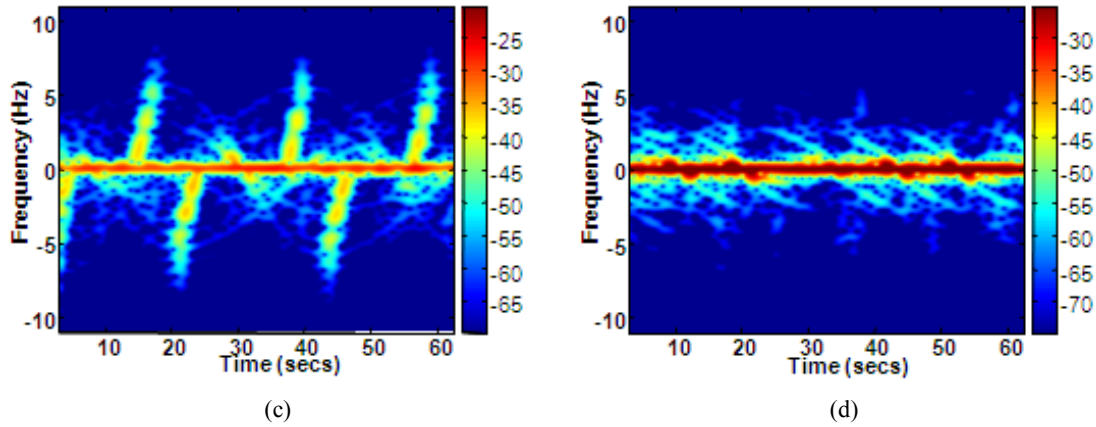


Figure 2.10. 3-arm wire model. (a) NEC-simulated backscattering. (b) NEC-simulated forward scattering. (c) Measured backscattering. (d) Measured forward scattering.

In the forward scattering spectrogram in Figure 2.10(b), we also see inter-blade interactions that result in a maximum Doppler shift of $\sqrt{3}v/\lambda$ along with the tip-to-base interaction described earlier, which gave rise to a maximum Doppler of only v/λ . In Figure 2.10(b), the Doppler tracks labeled (iii) and (iv) are illustrated in Figure 2.10(b). We notice that while tip-to-base interaction tracks peak when the blade is perpendicular to the incident wave, tip-base-tip interaction peaks when the blades are 60° to the horizontal. Because of the three bladed symmetry of the structure, the tracks for the backscattered data change signs every 60° while forward scattered Doppler tracks are repeated after every 60° rotation. Figures 2.10(c) and 2.10(d) are the corresponding measured results. They show fair agreement with the simulations. While we clearly see the tip-to-base interaction in Figure 2.10(d), the weak tip-base-tip interaction seen in

Figure 2.10(b) does not show up very clearly due to insufficient signal-to-noise in the measurement.

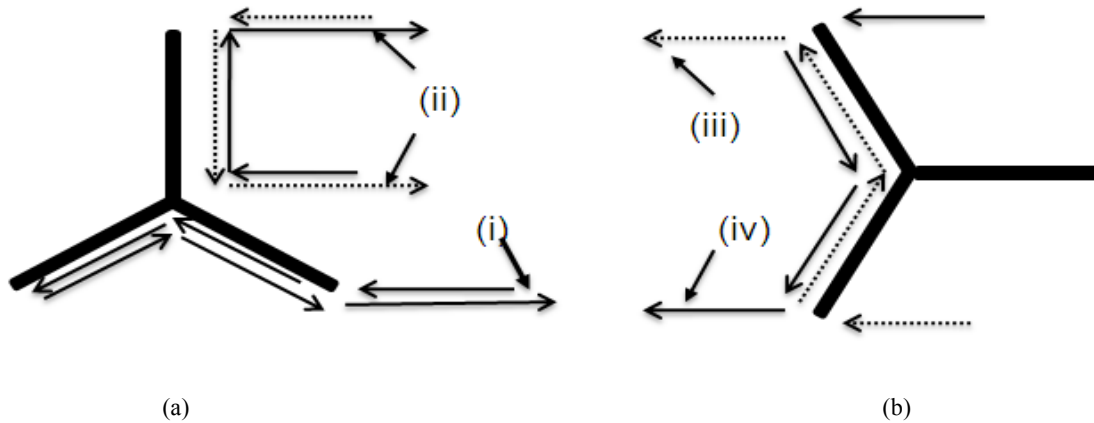


Figure 2.11: Illustration of additional Doppler-inducing mechanisms seen in Figure 2.10. (a) Backscattering mechanisms (i) and (ii). (b) Forward scattering mechanisms (iii) and (iv).

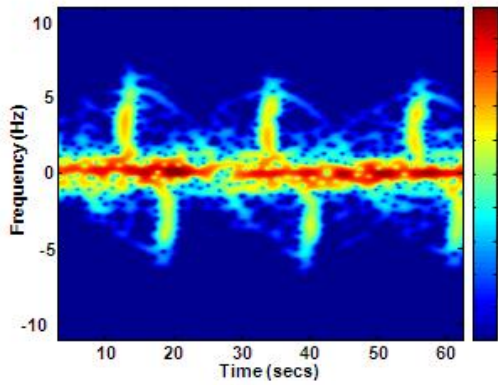
2.2.3 Bergey Windpower Turbine

Finally, the scattering characteristics of a small commercial wind turbine that is the same size as the wire model, shown in Figure 2.12, are described. The backscattering, shown in Figure 2.12(b), shows two interesting features that are distinct from the previous two models, namely, curved flash shape and uneven spacing between the flashes. They are attributable to the unique shape of the turbine blades as can be seen

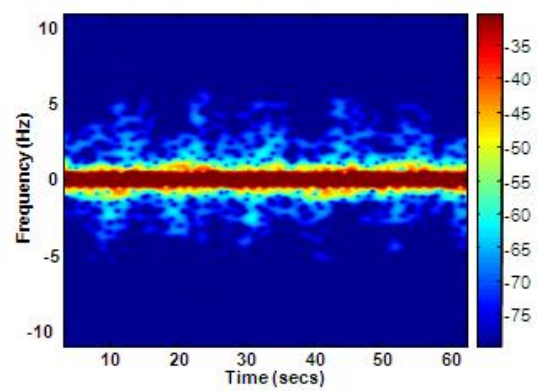
in Figure 2.12(a). The forward scattering spectrogram is shown in Figure 2.12(c). Although forward Doppler can be observed, it does not show any clear tracks.



(a)



(b)



(c)

Figure 2.12: (a) Photo of the Bergey Windpower turbine. (b) Measured backscattering. (c) Measured forward scattering.

The irregular flashing behavior in the backscattering can be explained by considering a simpler model comprising triangular-shaped turbine blades shown in Figure

2.13. In Figure 2.13, the blades are assumed to rotate clockwise. For this simple model, the edge of the triangular turbine blade does not become perpendicular to the radar in the orientation shown in Figure 2.13(a), but at θ degrees later (where 2θ is the inscribed angle of the blade). This results in a delayed flash, as marked by the first black line in Figure 2.13(c). The next flash also does not occur in the position shown in Figure 2.13(b) but at θ degrees earlier. Therefore the interval between two flashes is decreased by 2θ . On the other hand, the next interval is lengthened by 2θ . Figure 2.13(c) illustrates this effect. The blue flashes shown are normal equally spaced flashes that are 60° apart. The black flashes shown are from a triangular shaped blade occurring in the angular intervals described above. Note that even for a small θ value of 15° , the adjacent flash spacing becomes 30° - 90° instead of 60° - 60° , i.e., to an interval ratio of 1:3 instead of equally spaced. This can explain why the blade flashes in the real turbine are so unevenly spaced.

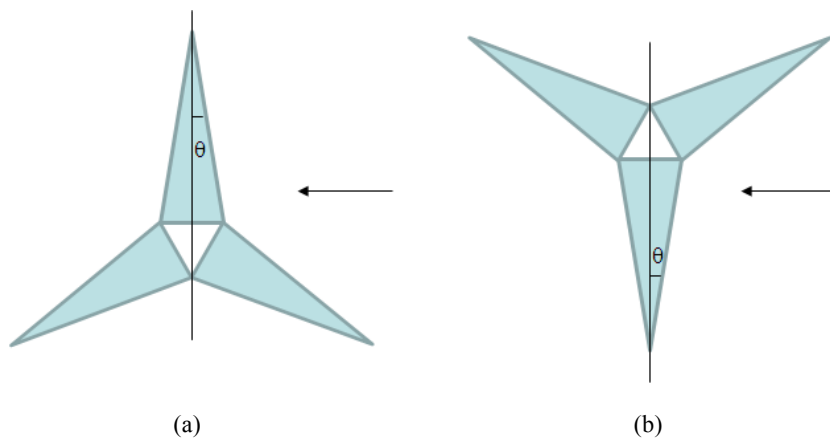


Figure 2.13

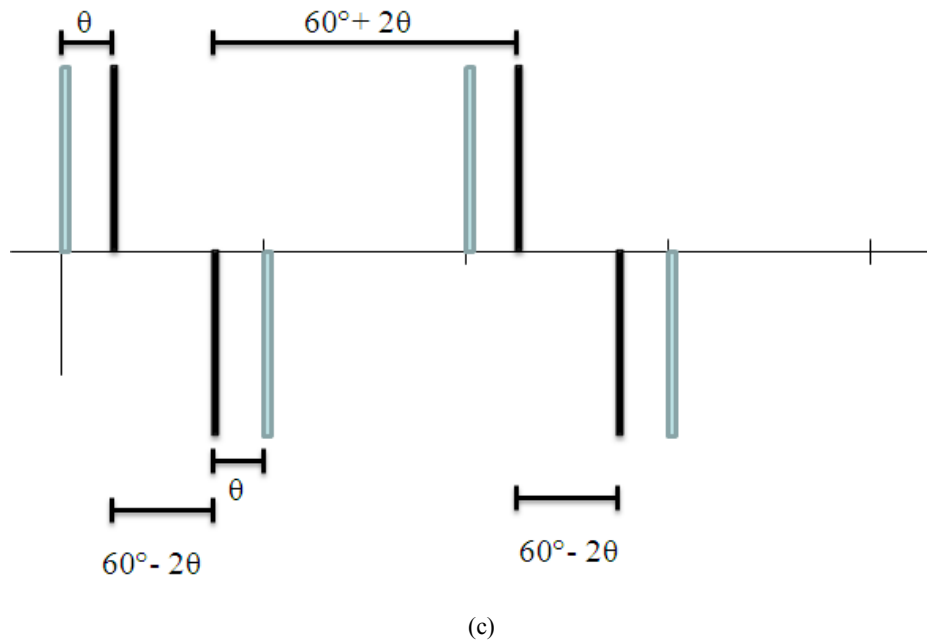


Figure 2.13: Blade shape effect based on a simple triangular blade model. (a) θ degrees before a blade flash occurs. (b) After 60 degrees of rotation. (c) Resulting irregular blade flashes as shown in black.

2.3 SUMMARY

In this chapter, the Doppler phenomenology of wind turbine scattering has been reviewed in detail. Measured scattering data from three different turbine models were examined. In addition to the blade flashes and tip halos observed by in-situ measurement in [18-21], the weaker Doppler features that arise due to multiple scattering effects in the turbine structure were also identified. Doppler features due to backscattering as well as forward scattering, which can only arise due to multiple scattering effects, were shown.

Near field effects were discussed. Finally, scattering features that result from the unique shape of the turbine blades were discussed.

Chapter 3: Doppler Features from Wind Turbines in the Presence of Ground

3.1 INTRODUCTION

In the previous chapter, the basic scattering phenomenology of an isolated rotating wind turbine was reviewed. However, in practice, wind turbines are located in more complex environments. Recently, concerns regarding the effects of ground on turbine scattering and how to account for these effects were raised in [68, 69]. Ground interactions could play an important role in scenarios where the radar is elevated high above the ground, such as those found in airborne surveillance systems as shown in Figure 3.1.

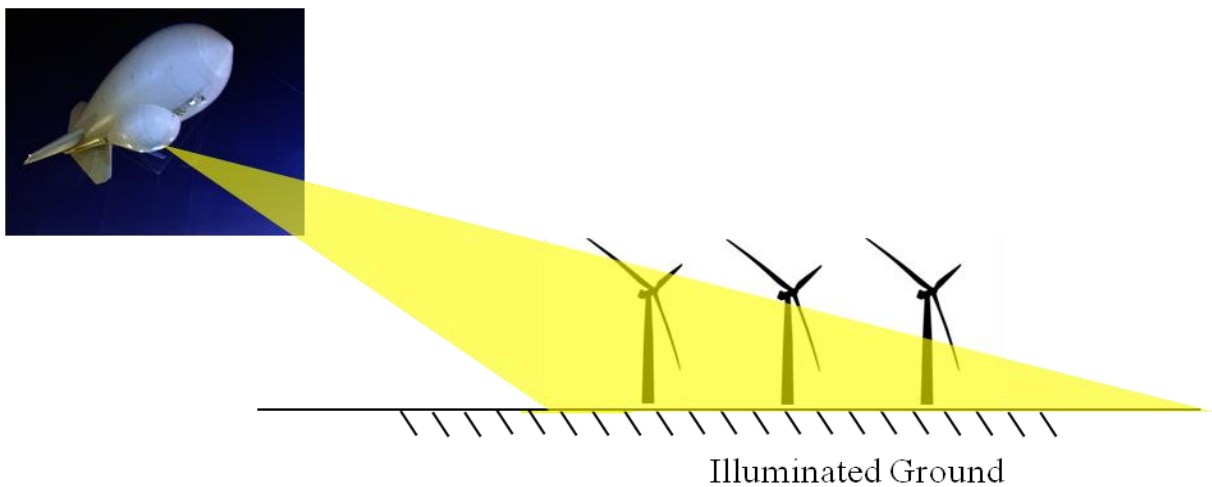


Figure 3.1: Pictorial representation of airborne radar illuminating ground and turbines.

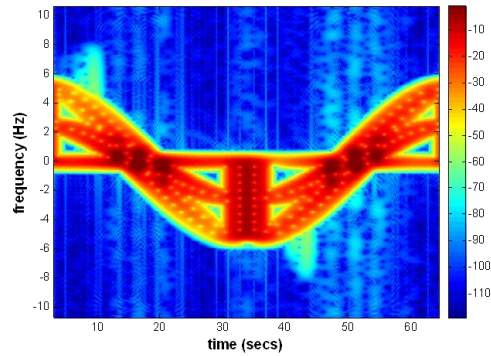
However, the mechanisms behind the presented results in [68, 69] were not described or explained. The physics of ground scattering for targets situated above ground is generally considered well understood in the electromagnetics community, and has been previously applied to simulate Doppler tracks of a moving human above ground [70].

In this chapter, we provide a detailed analysis of the Doppler features that arise in wind turbine scattering due to ground bounces. We first approach this problem by simulating a rotating wire above an infinite ground plane using NEC. However, this approach leads to an extremely crowded spectrogram making it very difficult to classify the signatures for even a single blade. Therefore, the approach is changed subsequently. Simulations are carried out using the high-frequency shooting-and-bouncing-ray code Ahilo [71]. First, we present Doppler features from turbine blades rotating above a stationary ground. The method of images is employed to account for the infinite ground plane. This allows for a rigorous accounting of ground effects without the need to model a large ground plane in the electromagnetic simulation. Doppler spectrograms are obtained using the short-time Fourier transform (STFT) and the tracks that arise from ground effects are identified and interpreted. In addition to the simulations, measurements are carried out on a rotating rod in the vicinity of a large metal ground plane to corroborate the simulation results. Finally, we report on Doppler features that arise in the case of a rotating turbine above a moving ground based on Ahilo simulation.

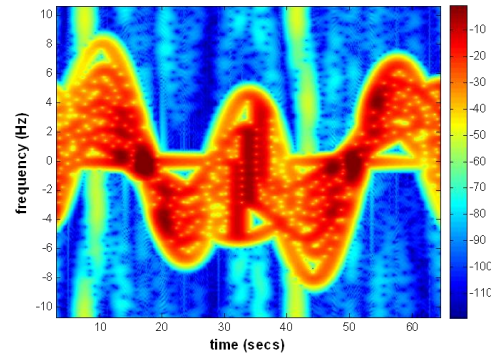
3.2 DOPPLER FEATURE ANALYSIS

The presence of ground introduces complexity to the returned signal due to the target-ground interactions in addition to the direct return from the target. Simulations are performed to investigate the time-varying Doppler features that arise from target-ground

interactions. Figure 1 (a) and (b) respectively show the spectrograms for a single wire rotating above a stationary ground using NEC. The wire size in this case is 60 cm. The frequency is set to 14 GHz and the elevation angle is set to 10 degrees.



(a)



(b)

Figure 3.2: NEC simulation for a rotating wire above an infinite ground plane. (a) stationary ground. (b) moving ground.

Figure 3.2 (a) shows signs of splitting of flashes as well as very weak signatures arising from higher order interactions between blade and the ground. Figure 3.2 (b) shows the spectrogram for the case of moving ground. It is observed that for the simplest case of a single blade, it is very difficult to discretely point out the features and the

mechanism behind the observed features. Therefore, from this point on, we use Ahilo to simulate characteristics of wind turbines in the presence of ground.

Figure 3.3(a) shows the CAD model of the turbine used. It contains the major components in a commercial turbine, including three blades, the nacelle and the tower. The size of the tower is 64 m, the radius of the hub is 2 m, and the length of each blade is 30 m. Figure 3.3(b) depicts the interaction of a turbine with the ground. The solid and dashed arrows in Figure 3.3(b) indicate the incident and scattered waves, respectively. With ground interactions, new Doppler tracks in addition to the strong blade flashes and weak tip halos previously documented in [18-21], [63] are expected in the time-dependent Doppler spectrum.

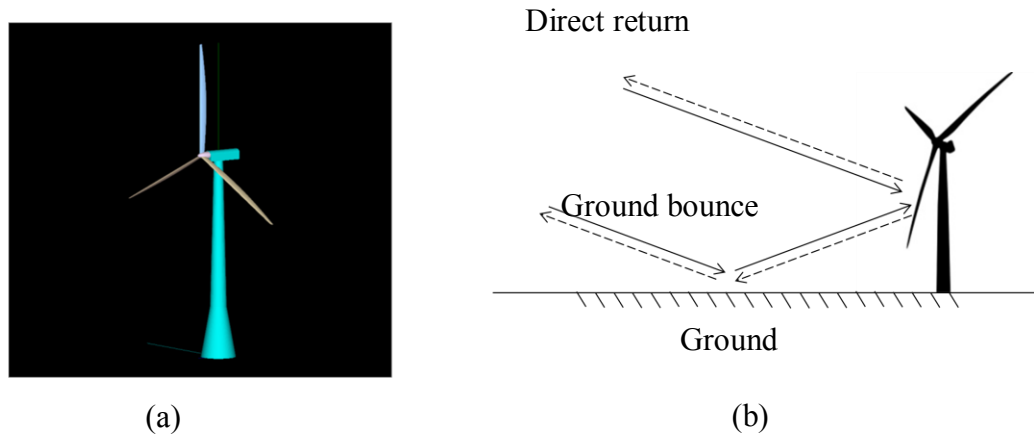


Figure 3.3: (a) Turbine CAD model. (b) Ground interactions.

For simulation, the radar frequency is set to 1 GHz and the radar is located at an elevation angle of 20° with respect to the ground. The polarization is horizontal. The turbine is assumed to be at a 90° yaw angle with respect to the radar (i.e., edge-on incidence). To perform the dynamic simulation, the backscattered data are collected for

each snapshot of the blade orientation, in 0.1° increments, over one complete revolution of the turbine blades. The built-in ‘rotation’ feature of Ahilo for a pre-defined portion of the target provides a convenient means to collect backscattering from the turbine. To simulate far-field backscattering from the turbine rotating above the ground, image theory is used [72]. The image of the real turbine is created and placed so that it forms a mirror image of the real turbine in the CAD model, Figure 3.4.

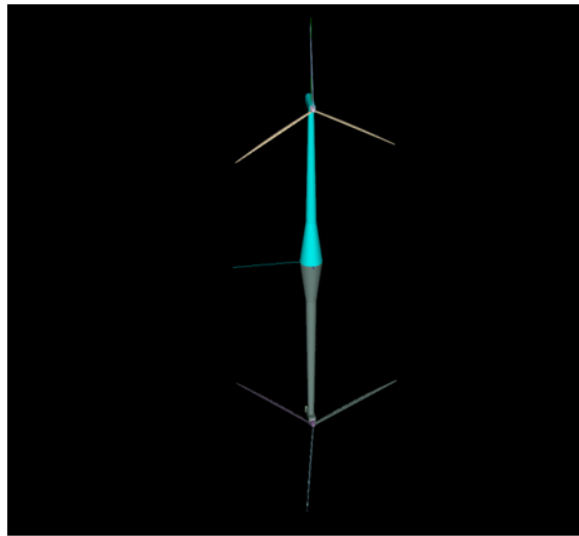


Figure 3.4: CAD model of turbine with its image.

This is done for each snapshot of the blade orientation. Consequently, the blades of the real turbine and those of its image rotate in opposite directions. To generate the total scattered field, first, monostatic data are collected with the source and observer located at the radar position. Second, bistatic data are collected with the incident wave originating from the image source position and the observer located at the real radar position. The superposition of the two simulated data sets gives the total scattered signal from the

turbine in the presence of ground. The data are then processed using the STFT with a time window of 0.3 second for an assumed rotation rate of 12 rpm. Figures 3.5(a) and 3.5(b) show respectively the spectrogram for a turbine rotating in free space and a turbine rotating in the presence of ground. For the turbine in free space, the key Doppler features come from blade flashes, labeled (i) in Figure 3.5(a), that occur every 60° rotation of the turbine blades. Every positive Doppler flash is followed by a negative flash. Weak tip halos can also be observed that are due to scattering from the blade tips. In Figure 3.5(b), two additional flashes accompanied by tip halos are present. These additional features are due to the presence of the ground. Figures 3.6(a), (b), and (c) illustrate

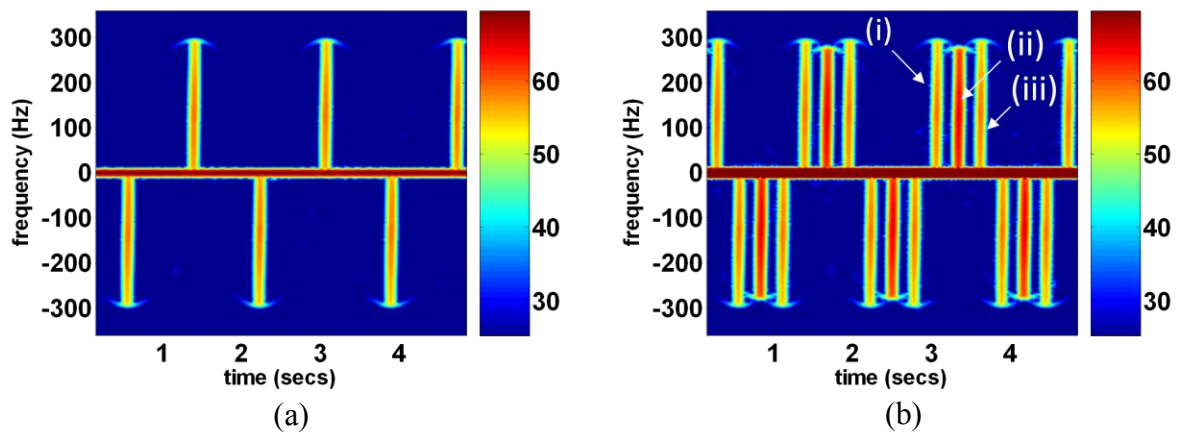


Figure 3.5: Spectrogram from turbine backscattering. (a) Without ground. (b) In the presence of ground.

respectively the mechanisms giving rise to flashes labeled (i), (ii) and (iii) in Figure 3.5(b). Figure 3.6(a) is the direct flash mechanism between the radar and the blade that gives rise to flash (i). Figure 3.6(b) shows the bistatic specular reflection mechanisms between the image source and the blade (or its image). These two mechanisms correspond to the two single-ground-bounce mechanisms and give rise to the flash

labeled (ii) in Figure 3.5(b). It occurs in time after the direct flash for the assumed counter-clock-wise rotation of the blades. The time interval between these flashes is a function of the elevation angle and the rotation speed of the turbine. Figure 3.6(c) shows the specular reflection mechanism between the radar and the image blade that correspond to the double-ground-bounce flash labeled (iii) in Figure 3.5(b). It occurs yet later in time. Note that the maximum Doppler of (ii) is less than that of mechanisms (i) and (iii) because the radial velocity of the blade relative to the source and observer is less than those in the other two cases. On the other hand, the strength of feature (ii) is 3dB higher than flashes (i) and (iii) since there are two single-ground-bounce mechanisms that are reciprocals of each other. They have identical Doppler returns. The single-ground-bounce mechanism also produces a specular reflection from the tower which is the reason for the much stronger DC-frequency component in Figure 3.5(b) relative to Figure 3.5(a). Aside from the single- and double-ground-bounce interactions described, no other Doppler flashes or higher-order features with strong intensities are observed. For example, no noticeable blade-ground-blade interaction is seen. This is due to a combination of the weaker scattering from two bounces off the blades and the shadowing from other blades. While the simulation results presented here are for an elevation angle of 20° , increasing the elevation angle will simply lead to an increase in the time lags between the three flashes and a decrease in the maximum Doppler of the single-ground-bounce flash. Finally, while we have analyzed the highly idealized geometry of a perfect conducting, infinite ground plane, an effective reflection coefficient approach can be used to model non-perfect-conducting, rough, or even non-flat terrains [73, 74]. However, that will only change the intensity of the ground-bounce features.

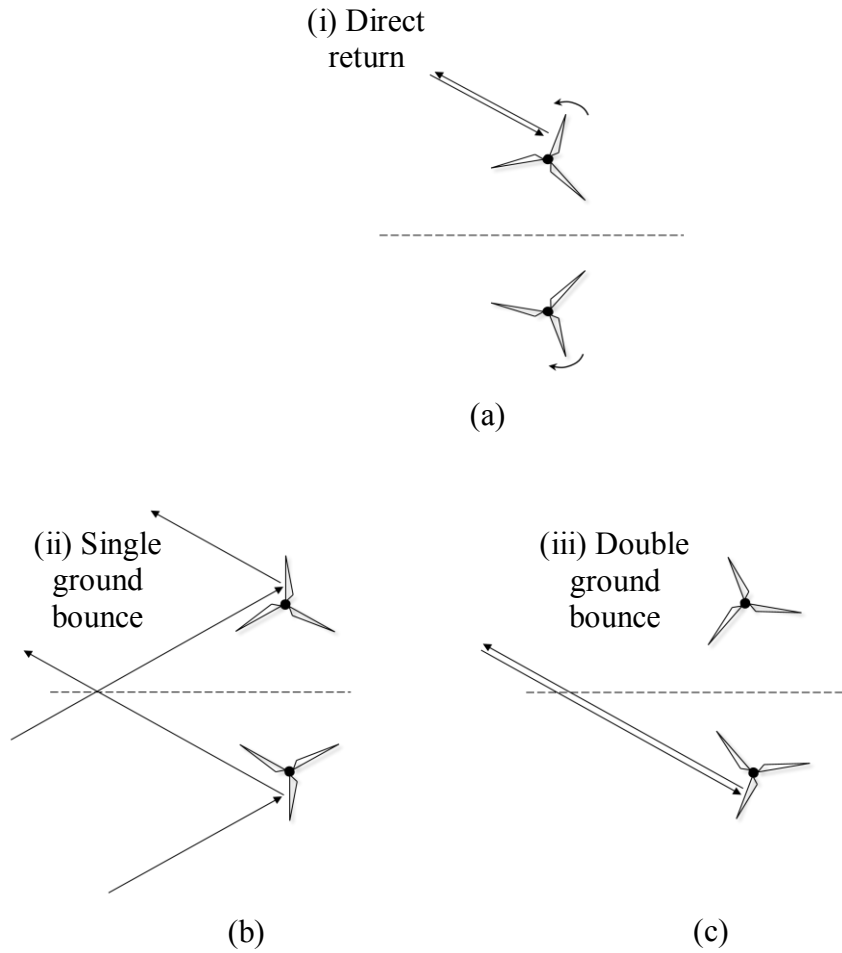


Figure 3.6: Image theory applied to simulate and explain the observed flashes. (a) Direct return flash. (b) Single-ground-bounce flash. (c) Double-ground-bounce flash.

3.3 EXPERIMENTAL CORROBORATION

Having simulated and analyzed the turbine Doppler features in the presence of ground, we next corroborate the simulations with laboratory measurements. A rotating metal rod of length 0.6 m and radius 1.2 mm is rotated about one end on a turn-table with

a large conducting ground plane placed next to the rod. The minimum distance between the rod's end-tip and the ground plane is 0.5 m. Figure 3.7(a) shows the experimental setup while 3.7(b) shows the corresponding measured results. Backscattering measurements are carried out using a vector network analyzer (*Agilent N5230A*) in continuous wave (CW) mode at 14 GHz. Data are collected for 420 seconds, which correspond to one rotational period of our turn-table, while the sampling rate is set at 3.4Hz. This corresponds to backscattering being collected every 0.25° of rotation. The slow sampling rate, 3.4 Hz, allows for a low intermediate frequency (IF) bandwidth setting to minimize the background noise in the data. A horn antenna, separated by 1.6m from the center of rotation for the rod is used to collect S_{11} measurements. The complex scattering data are first processed using a near-field-to-far-field transform algorithm [75] to correct the near-field effect due to the close position of the horn to the target. Subsequently, the data are processed using the STFT with a 30-second time window. Figures 3.7(b) and 3.7(c) respectively show the resulting spectrogram from the measured data for the rotating rod in free space and in the presence of ground. The very strong DC lines in both figures are due to the self-reflection from the mouth of the horn. Figure 3.7(b) shows the direct flashes from the blades whereas Figure 3.7(c) shows two additional blade flashes. It is observed that the measured blade flashes corroborate the simulated blade flashes in Figures 3.5(b) and 3.5(c) very well. The labels (i), (ii), and (iii) are respectively the direct, single-ground-bounce, and double-ground-bounce interactions illustrated in Figure 3.6. Similar to the simulations, the single-ground-bounce feature is stronger in strength than the direct and double-ground-bounce returns.

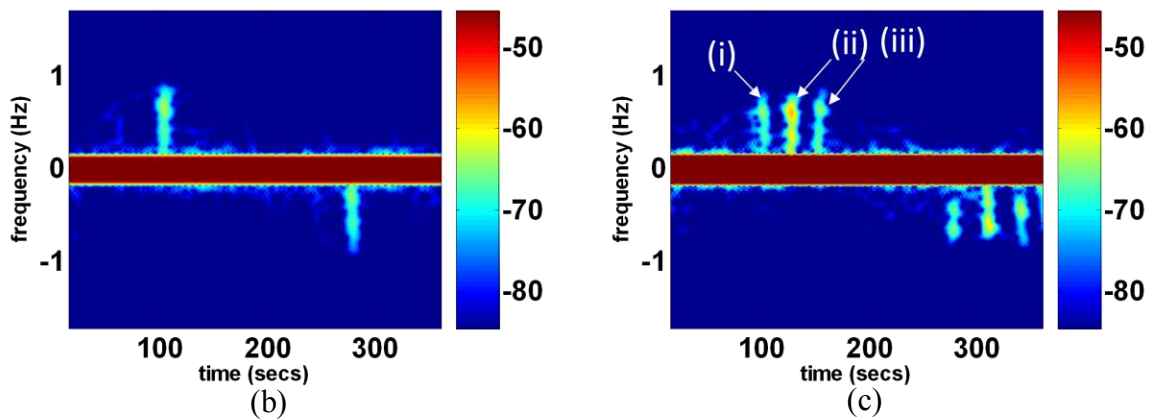
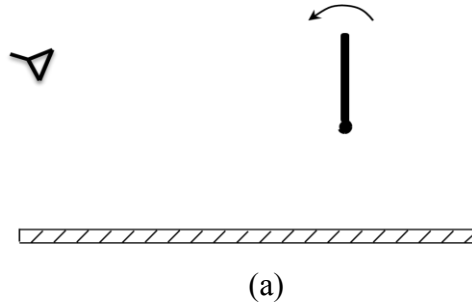


Figure 3.7: (a) Measurement setup. Spectrogram from measurement data. (a) Without ground. (b) In the presence of ground.

3.4 GROUND MOTION

Having analyzed turbine interactions with a stationary ground, we move on to study the case of a moving ground, which may have implications in the Doppler features of offshore turbines situated on a moving sea surface. We assume the entire ground moves sinusoidally in the vertical direction and again apply image theory to simulate this scenario. For this case the turbine and its image can be considered to be a single tower

with twice the length and having rotating blades on each end. Upon motion of the ground, the motion of the “image end” of the tower moves up and down, while the “real end” of the tower remains stationary. This motion is similar to how a mass on a spring moves. With motion of the ground, the image source will also have an up-and-down motion imparted to it. A displacement of ground by an amount d corresponds to a displacement of $2d$ in the image source and the image end. Realizing this dynamic scenario exactly in the Ahilo simulation requires detailed editing of the CAD file for each time snapshot. This is quite laborious, and we instead use an approximate scheme to carry out the simulation.

We assume the major scattering contributions come from: (1) the direct monostatic return from the real turbine shown in Figure 3.6(a), (2) the single-ground-bounce return from the real turbine and its image, which is the bistatic return depicted in Figure 3.6(b), and (3) the double-ground-bounce return from the image turbine shown in Figure 3.6(c). The time-varying returns from the three contributions are computed separately and then summed. In computing the return from each contribution, we neglect the slight change in the tower height as a function of time. The direct return (1) is not affected by the ground motion and is computed first. The bistatic return (2) is computed as follows. Backscattering is collected in the same manner as the stationary ground case with rotating blades. The ground motion is then injected into the signal by adding an extra phase at each snapshot of the turbine position during the course of its rotation. Given the received signal in the case of static ground, E^{stat} , the motion of the ground is incorporated as

$$E(t) = E^{stat}(t) \exp[-j(\bar{k}^i - \bar{k}^{OB}) \cdot \bar{r}'(t)] \quad (3.1)$$

where \vec{k}^i is the incident wave vector, \vec{k}^{OB} is the observation wave vector, and $\vec{r}(t)$ is the time-dependent position vector describing the displacement of the image turbine relative to the hub of the real turbine. The dot product ensures that the radar only registers the radial component of the ground displacement. The double-ground-bounce return (3) is computed from the image turbine in a similar fashion as that for return (2), i.e., the phase shift is added using eq. (3.1). By simulating returns (1) and (3) separately, we assume no interaction between the real turbine and its image takes place. This is a good approximation since no interactions between the two are observed for the stationary ground case, when the exact image theory is used.

For the analysis of moving ground, the wavelength of the ocean wave relative to that of the radar is an important consideration since the Fresnel zone is a function of the radar wavelength. For the case of the ocean wave being on the order of the Fresnel zone, the ocean wave motion may be modeled as simple harmonic in the vertical direction. Figure 3.8 summarizes the different Fresnel zone cases.

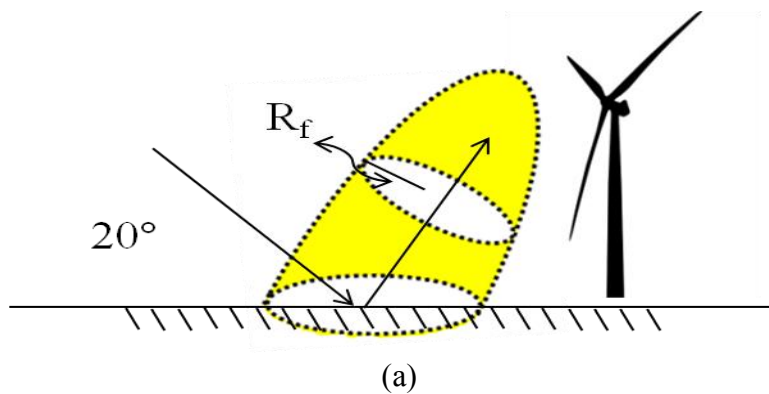
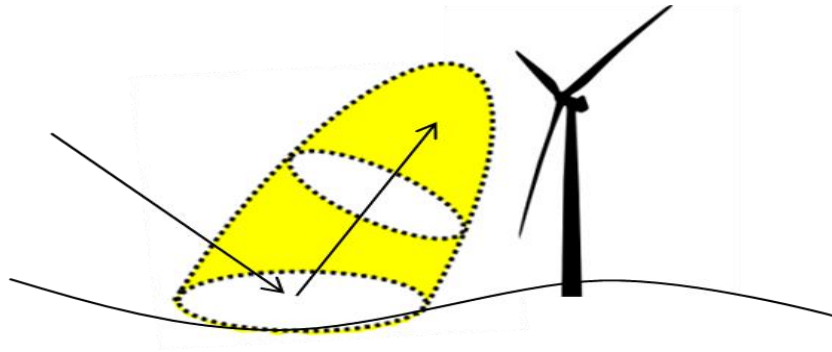
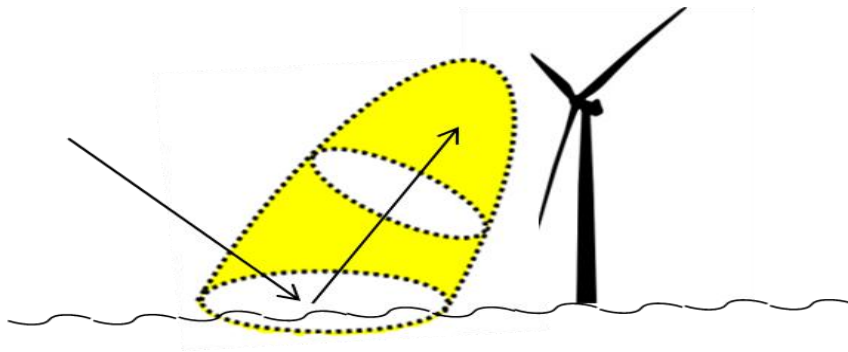


Figure 3.8



(b)



(c)

Figure 3.8: Fresnel zone comparison. (a). stationary ground. (b) larger ocean wavelength. (c) smaller ocean wavelength.

Figures 3.8 (a) – (c) respectively show the Fresnel zone size comparison with that of the different ground cases. Figures 3.8 (a) shows the case of stationary ground analyzed in the previous section. Figures 3.8 (b) and (c) are the moving ground cases for ocean waves with larger and smaller ocean wavelengths. At 20 degree incident angle, the Fresnel radius is 25 m. The wavelength of the water waves in shallow water is on the

order of 100m or more which corresponds to the case shown in Figure 3.8 (b). Therefore, the estimated Fresnel zone spot size on the water surface at 1GHz for the chosen parameters is an order of magnitude smaller. Consequently, the locally flat ground approximation would be an adequate assumption in this case. For the case of Figure 3.8 (c), the locally flat ground approximation may be used but the coherent intensity of the reflected signal will be reduced.

Figure 3.9(a) shows the spectrogram of the backscattered signal generated by the above methodology. In this case, the maximum ground displacement is set to 7 m and the period of the vibration is 9 seconds. In comparison to Figure 2(b), it is observed that the direct blade flash labeled (i) is not affected, while the two ground-bounce-induced blade flashes ride on sinusoidal tracks that result from the ground plane motion. Figures 3.9(b) and 3.9(c) demonstrate the mechanisms responsible for the observed bobbing of the flashes. Figure 3.9(b) shows the single-ground-bounce mechanism that gives rise to the bobbing motion of its corresponding flash labeled (ii) in Figure 3.9(a). Figure 3.9(b) demonstrates the path of the wave from the image source to the turbine blades and back to the observation point. In the interaction labeled (ii-a), the wave encounters a path length change as it travels back towards the observer. For interaction labeled (ii-b), the wave encounters a change in path length when the incident wave hits the real turbine blades. Both interactions give rise to identical Doppler, therefore, their corresponding flashes remain in phase. Figure 3.9(c) shows the double-ground-bounce mechanism responsible for the bobbing motion of the flash labeled (iii) in Figure 3.9(a). Thus, with ground motion, the single- and double-ground-bounce interactions ride on the motion of the ground plane. In addition, the return from the tower also acquires a non-DC return due to the ground motion.

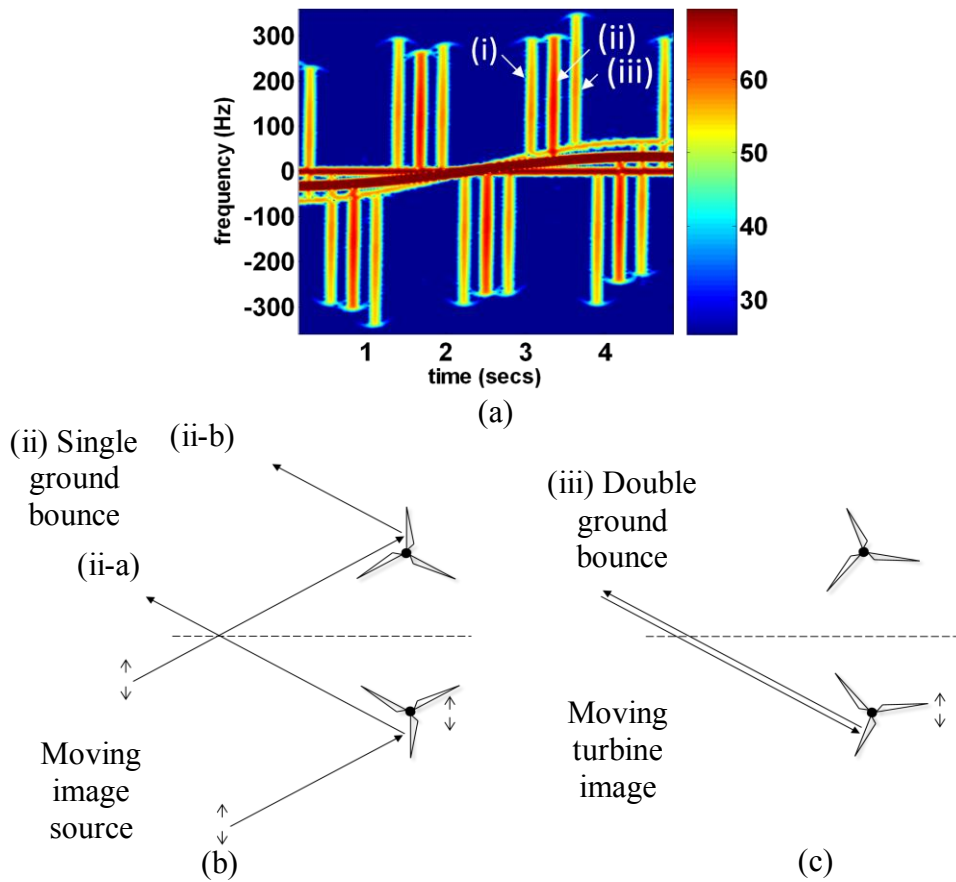


Figure 3.9: Backscattering from a turbine in the presence of a sinusoidally vibrating ground. (a) Spectrogram from backscattered data. (b) Single-ground-bounce return corresponding to track (ii) in (a). (c) Double-ground-bounce return corresponding to track (iii) in (a).

3.5 SUMMARY

This chapter broadened the phenomenological understanding of the turbine scattering features in the presence of ground. The problem was first approached by full

wave simulation, using NEC, of the scattering from a wire in the presence of ground. Due to the presence of multiple interactions in the wire, the ground bounced tracks were difficult to identify and explain. We changed the approach and employed a ray tracing code to study the scattering from a realistic CAD model of a turbine in the presence of ground. We employed image theory to incorporate ground scattering phenomenology. Both the single and double ground bounce give rise to an additional flash in the time-frequency plane. The simulations were corroborated by measurements. Finally, the effects of a moving ground in ground scattering phenomenology were considered. It was observed that the motion of the ground cause the single and double ground flash to ride on top of the motion of the ground.

Chapter 4: Time Frequency and ISAR Characteristics of Wind Turbines with Higher Order Motions

4.1 INTRODUCTION

While the radar Doppler features due to turbine blades undergoing a simple rotation motion have been well examined in Chapter 2, higher order motions such as structural flexing and vibration may also be present under dynamic operating conditions. It is important to understand the various radar features that can arise due to these motions. In this chapter, we simulate the radar features that may arise due to various types of higher order turbine motions and examine their time-varying Doppler characteristics. The motions examined include blade vibrations, blade flexing, and tower vibrations. The resulting Doppler features are then examined in the joint time-frequency (JTF) plane and inverse synthetic aperture radar (ISAR) imagery.

This chapter is organized as follows. In Section 4.2, we propose motion models used to simulate the motions. In Section 4.3, we use the proposed models to examine the JTF characteristics of a free-standing turbine. The short-time Fourier transform (STFT) is used to obtain the JTF representation. Next, we extend our analysis of the higher order motions to the ISAR image plane in Section 4.4. This broadens the motion analysis to include the range dimension in addition to the Doppler characteristics of turbines. In Section 4.5, the ISAR analysis is extended to take into account ground effects. Selected simulated motions are corroborated by laboratory model measurements in Sections 4.3-5. Finally, Section 4.6 provides the conclusions of the presented work.

4.2 MOTION MODELS

In this section, mathematical models to simulate the turbine motions are proposed. The motion models are constructed using a simplified point-scatterer basis. Point scatterer basis is a simple and approximate way to model a radar target [76]. In the particular case of a turbine, each blade of the turbine can be modeled as a set of closely spaced point scatterers. Here we adopt the same approach and extend it to incorporate higher-order turbine motions. Edge-on incidence of the radar wave is assumed as shown in Figure 4.1, as it produces the maximum Doppler extent, and thus the worst-case Doppler clutter. Using the point scatterer approach, the signal from turbine blades can be modeled by equation 1:

$$\phi(t) = \sum_{l=0}^2 \sum_{m=1}^M A_m \exp(-2jk\sqrt{((R - X_m)^2 + Y_m^2)}) \quad (1)$$

where A_m is the reflectivity strength of each point scatterer and the phase of the exponential represents the two-way path length of the wave from the radar to the turbine and back towards the radar. The variables in the exponential are as follows: k is the free-space propagation constant, R is the position of the radar relative to the hub of the blades along the x-axis, X_m and Y_m are respectively the x and y coordinates of each point scatterer. The inner summation controlled by the subscript, m , controls the position and the strength of each point scatterer along a single blade while the outer summation, over l , controls the angular spacing between the blades, which is $2/3$.

The various motions of the turbine can be modeled by choosing appropriate expression for X_m and Y_m . For uniform circular turbine motion, X_m and Y_m can be written as:

$$X_m = R_m \cos (\omega t + \theta_o + 2\pi l / 3) \quad (2)$$

and

$$Y_m = R_m \sin (\omega t + \theta_o + 2\pi l / 3) \quad (3)$$

where R_m is the magnitude of the distance of a point scatterer from the hub of the blades.

Four types of higher order motions that may exist on top of the uniform rotation motion of the blades are considered. The higher order motions include in-plane vibrations, out-of-plane vibrations, blade flexing, and tower vibrations. The five motions described are pictorially represented in Figure 4.1. Figure 4.1 (a) represents the turbine blades moving in a uniform circular motion. Figures 4.5.1 (b)-(e) respectively are the blades undergoing additional in-plane vibration, out-of-plane vibration, blade flexing, and tower vibration motions in addition to the circular motion of the turbine.

We refer to the blade vibrations that may occur within the plane of the rotating blades as in-plane vibrations. The proposed motion model incorporating in-plane vibrations is described by equations (4) and (5):

$$X_m = R_m \cos (\omega t + \theta_o + 2\pi l / 3 + \Delta\theta \cos(\omega_{vib} t)) \quad (4)$$

and

$$Y_m = R_m \sin (\omega t + \theta_o + 2\pi l / 3 + \Delta\theta \cos(\omega_{vib} t)) \quad (5)$$

where $\Delta\theta$ is the angular amplitude of the vibration and ω_{vib} is the angular frequency of the in-plane vibrations.

A motion model of out-of-plane vibrations is shown in equations (6) and (7):

$$X_m = R_m \cos (\omega t + \theta_o + 2\pi l / 3) \sin (\pi / 2 + \Delta\phi \cos(\omega_{vib} t)) \quad (6)$$

and

$$Y_m = R_m \sin (\omega t + \theta_o + 2\pi l / 3) \sin (\pi / 2 + \Delta\phi \cos(\omega_{vib} t)) \quad (7)$$

where the out-of-plane motion along the z-direction has been projected into the xy-plane by the second sine term. The z-displacement can be ignored since it does not result in any Doppler shift detected by the radar. The argument of the second term models out-of-plane vibrations while the additional $\pi/2$ phase keeps the motion centered about the xy-plane.

This model can also incorporate blade flexing motion. It can be accomplished by varying the angular position of each point scatterer. Curvature can be introduced into the blade by appropriately assigning values of the starting angle, θ_m , to each point scatterer

and varying the values appropriately with time. A model of blade flexing is given by equations (8) and (9):

$$X_m = R_m \cos (\omega t + \theta_o + \theta_{amp} \sin(\omega_f t + \theta_m) + 2\pi l / 3) \quad (8)$$

and

$$Y_m = R_m \sin (\omega t + \theta_o + \theta_{amp} \sin(\omega_f t + \theta_m) + 2\pi l / 3) \quad (9)$$

where ω_f is the flexing frequency of the blades and θ_{amp} controls the amplitude of the flexing.

Finally, tower vibrations can be incorporated into our model by varying the range of the turbine relative to the radar, i.e, the ‘R’ that appears in equation (1). The ‘R’ can be rewritten as:

$$R = R_o + A_t \sin(\omega_t t) \quad (10)$$

where A_t and ω_t respectively are the amplitude and the frequency of the tower motion. Although a physical tower is not present in the model, we assume the dominant Doppler contribution will come from the turbine hub—the farthest point from the base of the tower.

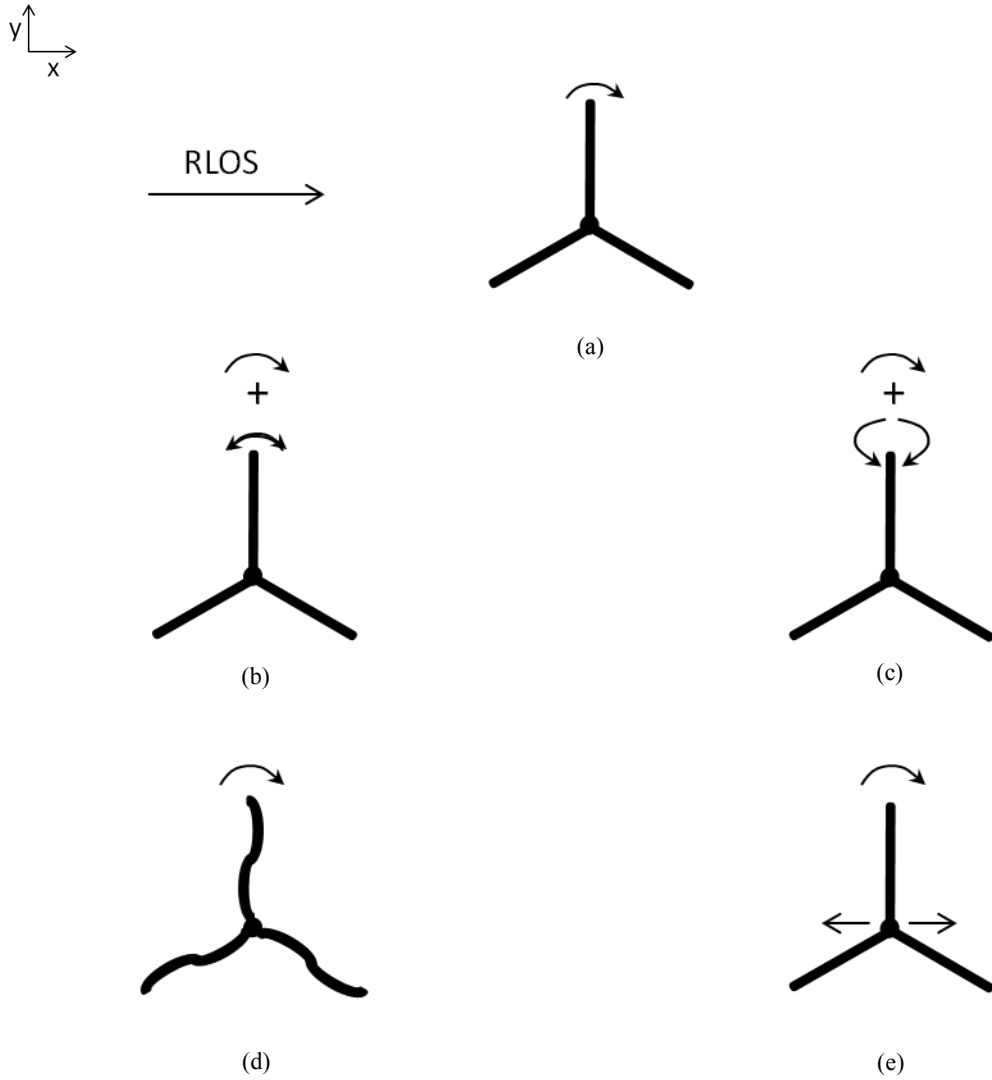


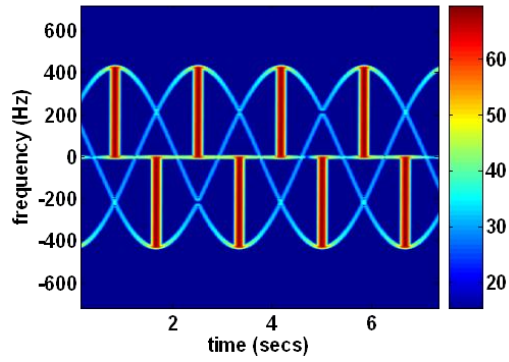
Figure 4.1: Pictorial representation of the blade motions. (a) uniform rotation motion. (b) in-plane vibrations. (c) out-of-plane vibrations. (d) blade flexing. (e) tower vibration.

4.3 TURBINE JTF CHARACTERISTICS

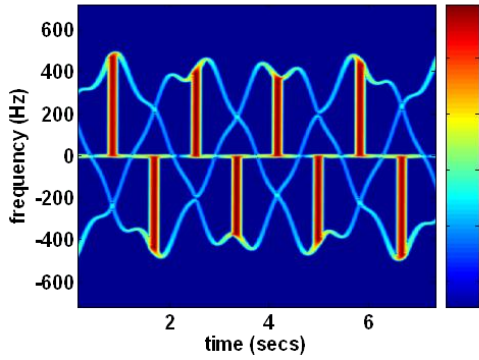
Having proposed the analytical higher-order motion models, their resulting JTF signatures are presented in this section. In the simulations, the blade length is set to 34

m. The spacing between the point scatterers is set to $\lambda/5$ to ensure that the simulated results resemble the real returns from a turbine. The blades are assumed to be rotating at 12 rpm. The radar frequency is at 1.5 GHz, which is typical of long-range surveillance radar. The complex backscattered data as a function of time are processed using the STFT to obtain the spectrogram. A time window of 0.3 second is used in the STFT and a Gaussian window is applied before the Fourier transform. The parameters for the higher order motion are chosen to emphasize and clearly display the new features that may arise based on the proposed models.

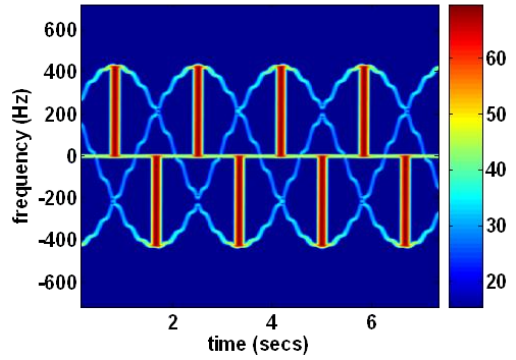
Figure 4.2 shows a set of figures demonstrating the JTF characteristics using the point scatterer model. Figure 4.2 (a) is the spectrogram for uniformly rotating blades acquired using equations (2) and (3). The most prominent features seen are the blade flashes that occur when the blade is perpendicular to the radar line-of-sight. The blade flashes are positive when a blade is approaching the radar and are negative when it is receding away. The blade flashes occur after every 60 degree rotational motion of the blades. The flashes are enveloped by sinusoidal “tip halos” that arise due to tip diffraction. The tip halos are sinusoidal due to the circular motion of the blades. The point scatterer model successfully captures the key Doppler features of the blade motion seen in in-situ measurements reported in [10].



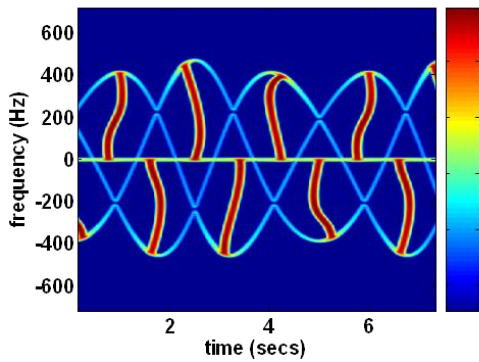
(a)



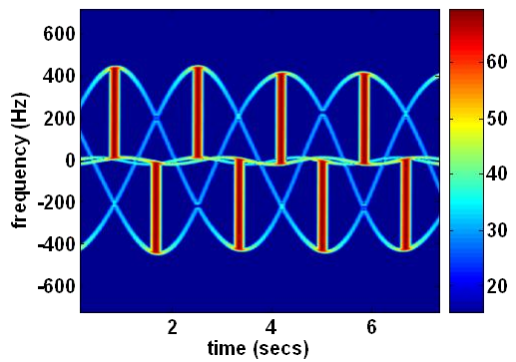
(b)



(c)



(d)



(e)

Figure 4.2. Point scatterer simulated JTF characteristics of the turbine motion. (a) uniform circular motion. (b) in-plane vibrations. (c) out of plane vibrations. (d) blade flexing. (e) tower vibrations.

Figure 4.2 (b) is the spectrogram with in-plane vibrations introduced. In this case, the vibration amplitude, $\Delta\theta$ and ω_{vib} appearing in equations (4) and (5) are set to 0.8 degree and 33 rpm respectively. With in-plane vibrations, the extra motion is evident in several forms. The extra motion is due to $\Delta\theta$ and ω_{vib} that effectively increase or decrease the radial velocity of the blades. The tip halo loses its perfectly sinusoidal shape and is distorted since the radial velocity of the blade relative to the radar varies at various times along the blades' motion. Since the radial velocity of the blade changes, the maximum Doppler of the tip-halos also varies and may be lower or higher than the case without any vibration depending on whether the blade is increasing or decreasing in velocity due to the vibrations. Furthermore, although not immediately evident in the spectrogram, the angular spacing between adjacent flashes is not exactly 60 degrees. This difference is also attributed to the time-varying vibrational changes that the blades undergo.

Figure 4.2 (c) incorporates out-of-plane vibrational motion into the uniform circular motion of the turbine. The $\Delta\phi$ and ω_{vib} in equations (6) and (7) are set to 5 degrees and 50 rpm respectively. The spectrogram shows clear tip distortion. The tip distortion has a unique signature and is rather different from the tip distortion observed for in-plane vibrations. However, the flash Doppler and spacing remains uniform.

In Figure 4.2 (d), the blades are assumed to undergo flexing motion. The flexing frequency, ω_f , in equations (8) and (9) is set to 12 rpm while θ_{amp} is set to 0.1 degree. The most conspicuous feature of the spectrogram is the curved blade flashes. The curved

flashes result because different parts of the blade are perpendicular to the radar at different times and the nature of the flexing manifests itself in the curvature of the flashes. The flexing motion also causes variations in maximum Doppler of the tip halos in the spectrogram.

Finally, Figure 4.2 (e) shows the JTF characteristics of turbine motion with the tower vibrating. Here, the vibration amplitude is set to 1 m which corresponds to a maximum angular displacement of 0.96 degree of the hub for a 60 m long tower. The vibrating frequency is set to 30 rpm. The vibration of the tower adds a Doppler shift to the DC line and in this case, the shift is sinusoidal as modeled in equation (10). The blade flashes and tip halos are observed to ride on the sinusoid from the tower motion, which varies the effective radial velocity of the blades relative to the radar wave.

Having modeled and simulated the JTF characteristics of the various turbine motions, we carry out laboratory model measurements to corroborate the simulations. The measurements were carried out as follows. A vector network analyzer (*Agilent N5230A*) was used to collect measurement data in continuous wave (CW) mode at 11 GHz. The turbine comprises a 3-arm wire model with 60 cm long blades and a wire radius of 1.2 mm. Notice that our model is about 60 times smaller than the simulation while the frequency is scaled up only by a factor of 8. This is due to the limitation of our measurement equipment. The data were collected for 65.5 seconds, which corresponds to one rotational period of our turn-table, while the sampling rate was set at 22Hz. S_{11} parameters were collected from a rotating turbine using a horn antenna placed 2.2 m from the center of the blades. Since the radar was located within the near field of the turbine, a near-field to far-field transform algorithm discussed in [19] was applied to the data to eliminate near-field effects. Background subtraction was performed to reduce the effects of reflection within the horn, which gave rise to a very strong zero-Doppler component.

The complex scattering data versus time were processed using the STFT. A time window of 5-second was used to process our results.

The JTF results of the measurement data are shown in Figure 4.3. Figure 4.3 (a) shows the spectrogram from a uniformly rotating turbine. We observe the blade flashes and the tip halos described earlier. Figure 4.3 (b) shows the spectrogram resulting from “simulated” in-plane vibrations. In order to acquire Figure 4.3 (b), the data were re-sampled from Figure 4.3 (a) at the desired angles dictated by the motion models in equations (4) and (5). In order to resample the data, we first sinc-interpolate our signal to increase the sampling rate. Next, we set $\Delta\theta$ and ω_{vib} to 1.5 degrees and $8/66*2^*$, respectively, to acquire the measured data under the assumed motion. Clearly seen in Figure 4.3 (b) are the tip distortion and non-uniform max flash Doppler that are similar in nature to those seen in Figure 4.2 (b). Also, due to the difference in the speeds of the two cases, Figure 4.3 (b) only contains four while Figure 4.3 (a) contains five flashes.

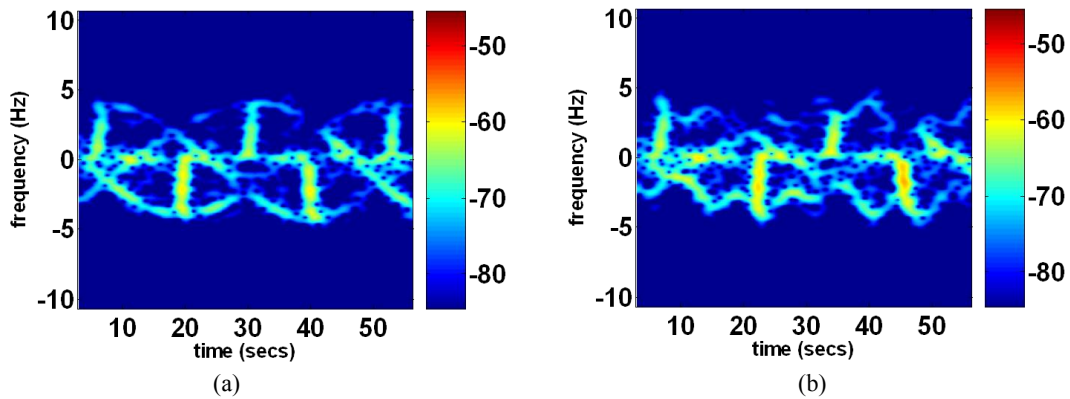


Figure 4.3: Measurement results. (a) Uniformly rotating turbine. (b) With in-plane vibrations injected.

4.4 TURBINE ISAR CHARACTERISTICS

The JTF analysis in the last section allows us to observe the time-varying Doppler characteristics of the turbine motion. However, it does not provide down-range information of the turbine structure. In this section, we introduce the range dimension into our feature analysis and study the turbine features in the (range)-(cross range) plane, or its ISAR image. The results are presented as a single composite image of all the images acquired in the course of rotation of turbine blades.

4.1 COMPOSITE ISAR IMAGES – SIMULATION AND MEASUREMENT

In this section, we focus first on a turbine undergoing regular rotation to illustrate the process of forming a composite ISAR image. Simulations and measurements were carried out for a turbine model with 60 cm blades. To form an ISAR image, backscattered data over a finite frequency bandwidth and target rotation angles are needed. In the measurements, we swept over a range of frequencies from 10-12 GHz in increments of 33.3 MHz. The turbine motion was sampled at every 0.5 degree of rotation. Each image of the turbine was formed by processing 24 degrees of data. The point scatterer basis was modified to take into accounts the above parameters. The simulations were performed in the far-field while the near-field to far-field algorithm [19] was used to eliminate near-field effects in the measurements.

First, the ISAR images of a single turbine at selected positions are presented. Figure 4.4 shows the simulated and measured ISAR images of a turbine at three different angular positions. Figure 4.4 (a) shows a simulated image of a turbine for the case of a positive flash. The other two blade tips are observed as the two points seen in the figure.

Figure 4.4 (c) shows a snap shot of the blades for the case when none of them are in a flashing position and we only observe the tips of each blade. Figure 4.4 (e) shows the case of a negative flash. Figures 4.4 (b), (d), and (f) are the corresponding measured results corroborating the simulations. For the measurements, the actual collected data result in images with a cross range between -0.7 m and 0.7 m. The images are zero-padded in cross range for an easier comparison with the simulations. Figure 4.4 (g) and (h) are the corresponding composite ISAR images, which are formed as follows. First, a single image is generated as described above. Subsequently, the imaging window is slid by 2 degrees to obtain a sequence of images of the turbine as it rotates until both a positive and a negative flash are captured in the image. Finally, the images are summed in intensity to obtain a complete composite ISAR image of the blades. Other than the intensity difference, the key features in the simulation and measurement images agree.

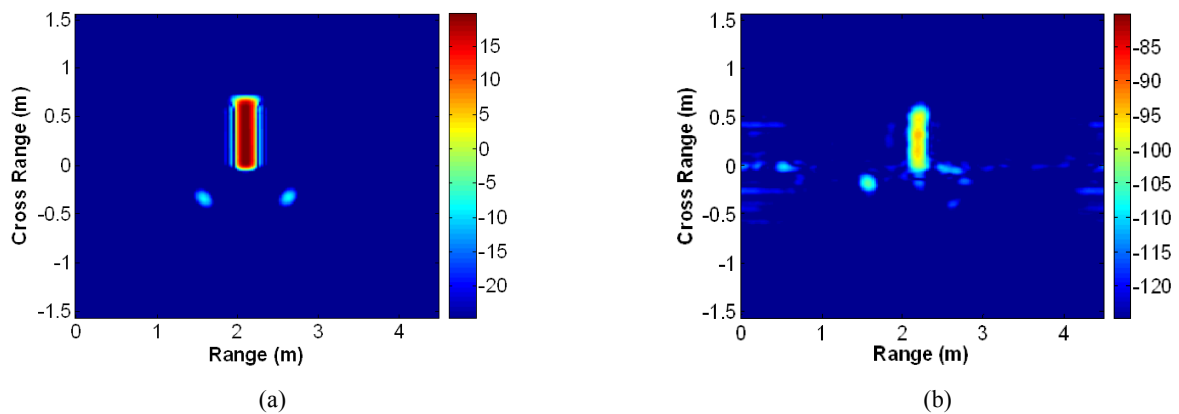


Figure 4.4

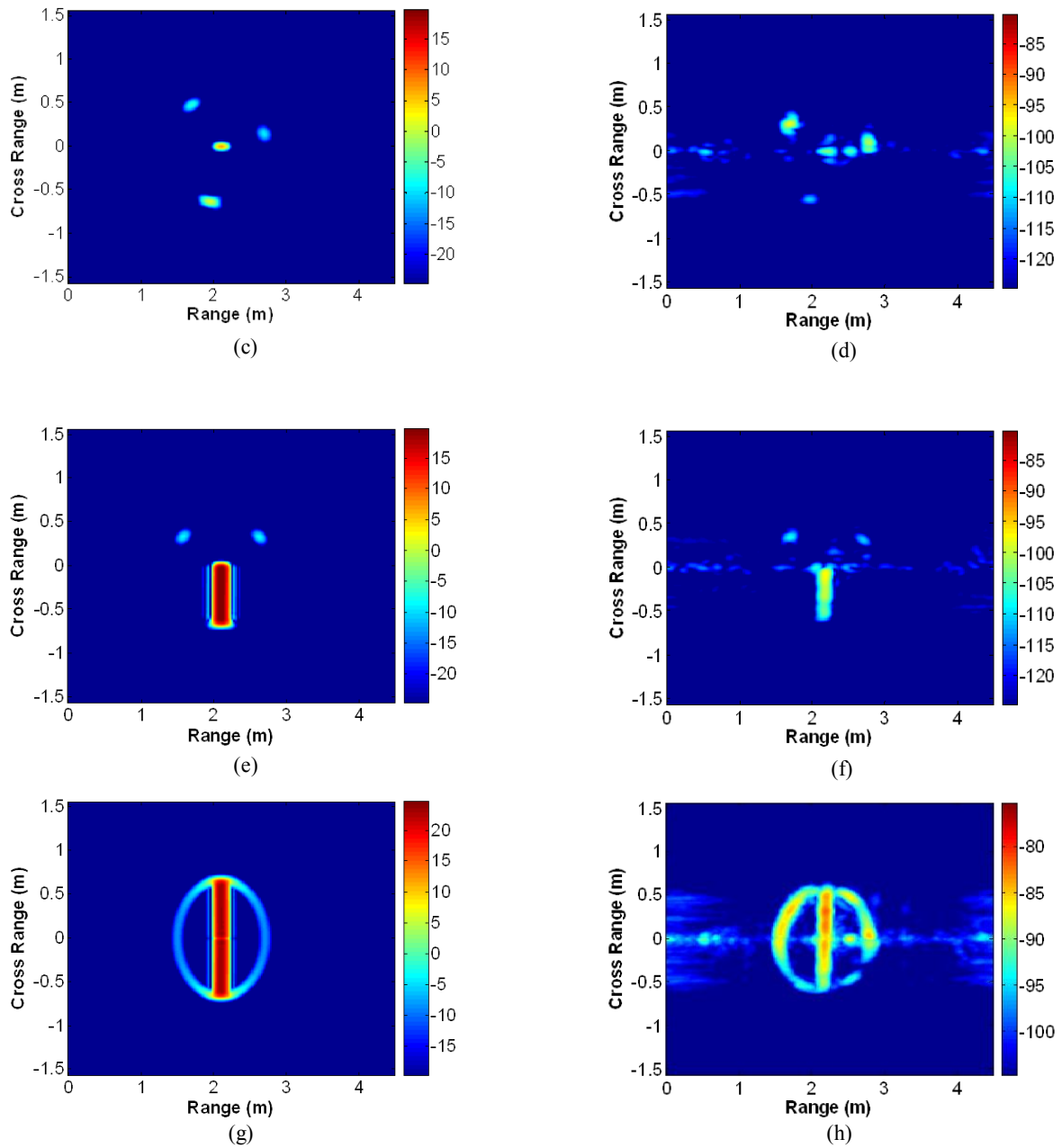


Figure 4.4: ISAR images of turbine at various blade angular positions. (a), (c), and (e) are simulated using point scatterer model. (a) Positive flash. (c) Blades in a non-flashing position. (e) Negative flash. (g) Composite image. (b), (d), (f), and (h) are corresponding measured results.

4.4.2 COMPOSITE ISAR IMAGES WITH HIGHER ORDER MOTIONS

Having demonstrated how single-snapshot images can be combined to form a meaningful composite ISAR image of a uniformly rotating turbine, we shall use this representation to study different higher order motions for a full size turbine.

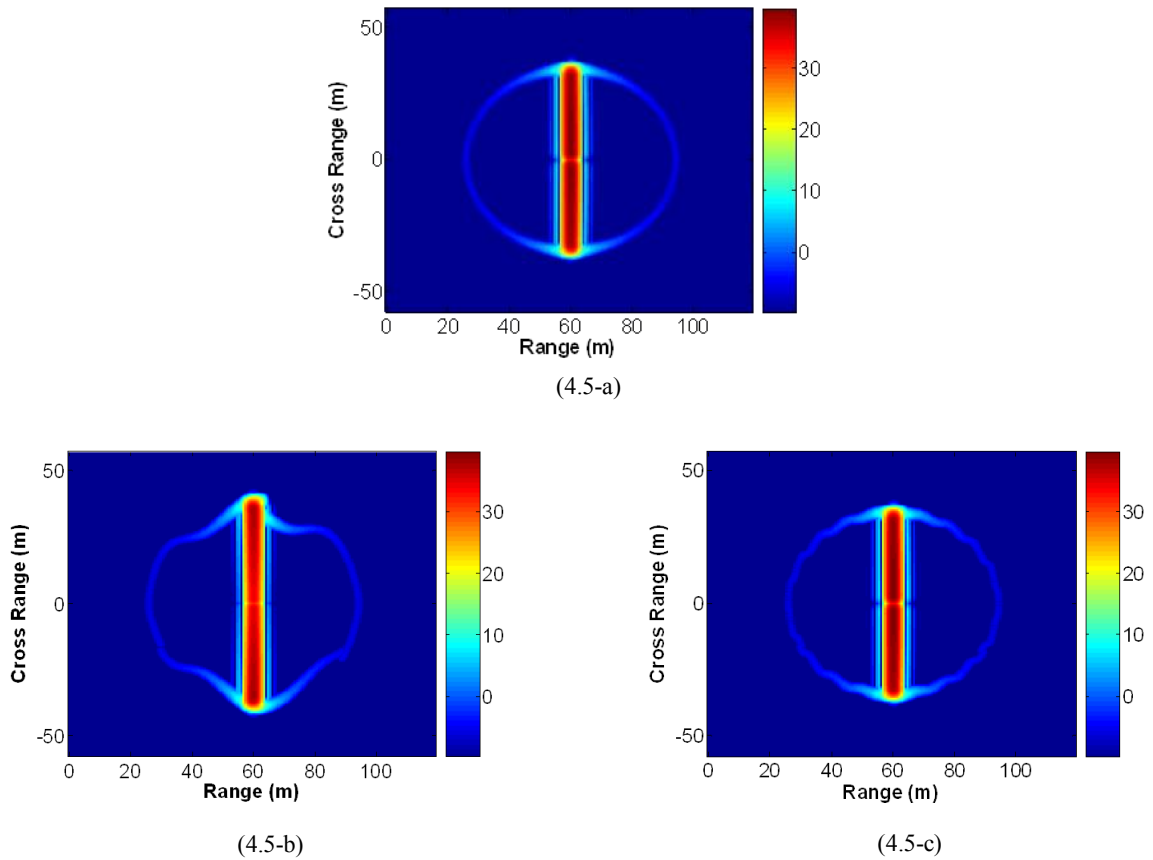


Figure 4.5

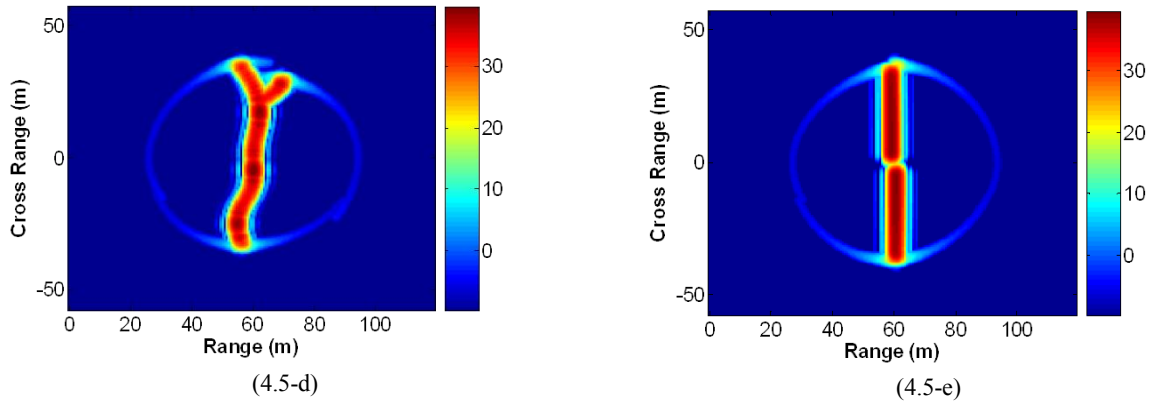


Figure 4.5: Composite ISAR images of turbine. (a) Uniform circular rotation. (b) In-plane vibrations. (c) Out-of-plane vibrations. (d) Blade flexing. (e) Tower vibrations.

The size of the turbine blade is the same as that in Section 3, or 34 m. In order to obtain ISAR for full size turbines, the point scatterer basis is modified to sweep over a bandwidth of 75 MHz with the center frequency set at 1.5 GHz at increments of 1.25 MHz. The simulated turbine motion is sampled at every 0.05 degree of rotation. Each image of the turbine is formed by processing 3 degrees of data. Subsequently, the imaging window is slid 1.5 degrees to obtain the image sequence of the turbine as it rotates until both a positive and a negative flash is captured in the image.

Figure 4.5 (a) shows the ISAR for a uniformly rotating turbine. As seen previously, the key features in the image are the positive and negative blade flashes and the circular tip centered between the flashes. The tip halos seen in the JTF plane become circle in the ISAR plane due to the circular motion of the blades. Figure 4.5 (b) is the ISAR composite image for the case where the blades undergo in-plane vibrations. It is observed that the tip wobbles in the two-dimensional ISAR plane and the three distinct tip halo tracks are observed corresponding to each blade. Figure 4.5 (c) shows the case for out-of-plane vibrations. The flashing behavior remains identical to the case without

vibrations. Also, the slightly jagged nature of the tip vibrations is clearly seen for this case. Figure 4.5 (d) is the case when the blades flex during rotation. The flexing of the blades is evident in the curvature of the positive and negative flashes. Also, the tip is observed to be slightly distorted. The weaker flashing strength for the cases of 5 (c) and (d) is due to the variation in the spread of the flash energy in range and cross range. Figure 4.5 (e) is the case for tower vibrations. This motion is observed in the range dimension in the form of shifted blade flashes. Also, due to the motion of the tower, the tip is distorted.

In order to provide some validation of the simulated phenomenology, we again use a re-sampling of the measured data from the laboratory model to emulate the effect of in-plane vibration. Figure 4.6 (b) shows the ISAR image resulting from simulated in-plane vibrations. In order to acquire Figure 4.6 (b), the data were re-sampled from Figure 4.6 (a) (note that Figure 4.6 (a) is the same as Figure 4 (h)). The data were re-sampled using the motion models in equations (4) and (5). We set $\Delta\theta$ and ω_{vib} to 1.5 degrees

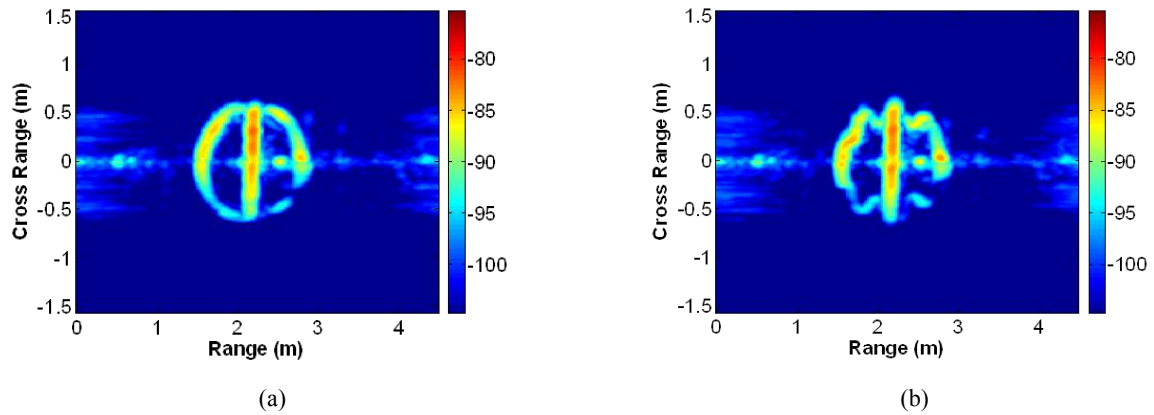


Figure 4.6: Measured composite ISAR image. (a) Uniformly rotating turbine. (b) With in-plane vibrations injected.

and $8/66*2^*$, respectively, as was done for the data shown in Figure 4.3 (b). We observe that the tip trace in Figure 4.6 (b) shows distortion in the ISAR plane. This is consistent with the findings from Figure 4.5 (b).

In addition to injecting vibrations into the data for a smoothly rotating turbine, we also performed an experiment where the turbine underwent physical vibrations. The experimental set-up is shown in Figure 4.7. A red plastic straw is placed along the path of motion of the turbine. Upon encountering the straw, the blades undergo in-plane vibrations.



Figure 4.7: Measurement set-up to cause physical in-plane vibrations.

Figure 4.8 shows the case where we perform a measurement and the turbine physically undergoes in-plane vibrations. Since the majority of the turbine signature is contained within the blade tips which are generally weak in strength, we attach a series of aluminum blades on our blades to increase blade visibility. We attach 5 bulbs to each blade. As the turbine rotates, its motion is impeded by a plastic straw. Upon overcoming the impedance, the blade undergoes in-plane vibrations. The results are shown in Figure

4.8. Due to the addition of the aluminum bulbs, the blade appears as four aligned point

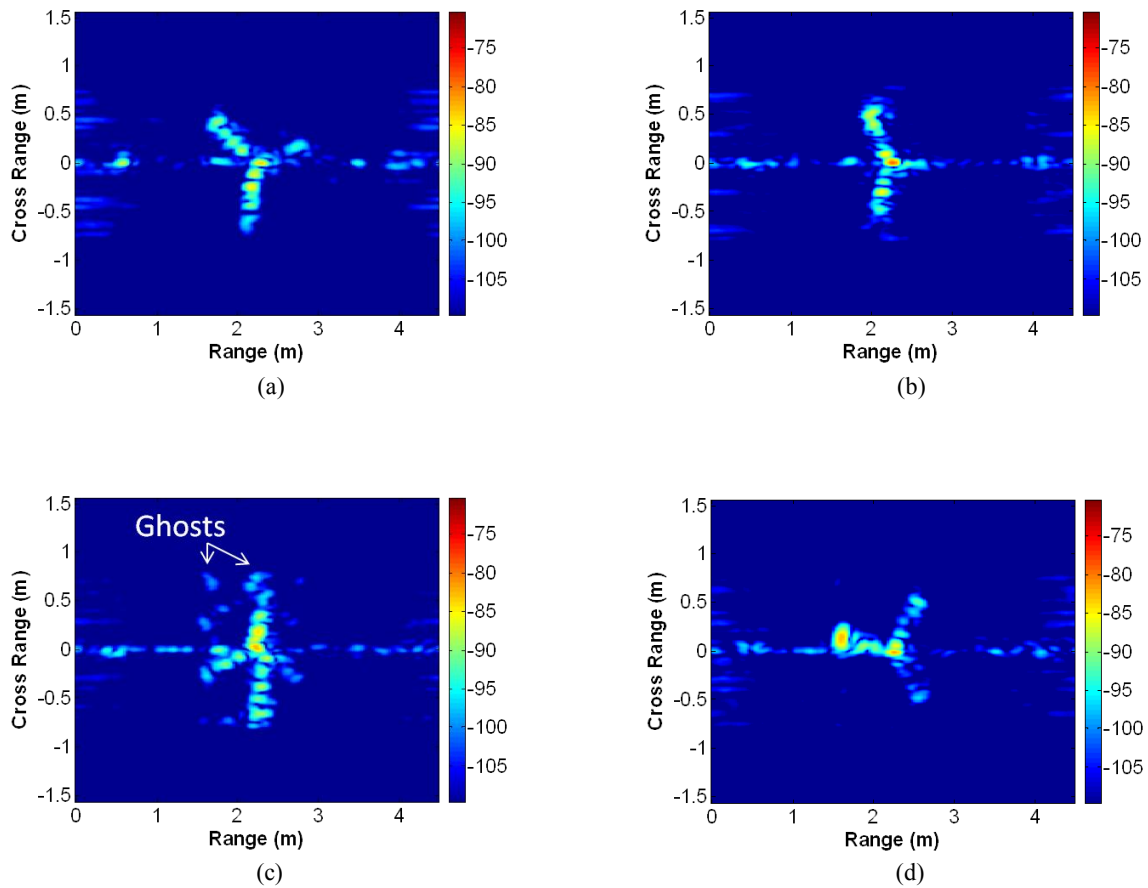


Figure 4.8: Measured ISAR images of turbine rotating clockwise with aluminum bulbs on blades that undergoes physical in-plane vibrations. (a) A snap shot before the turbine motion is impeded. (b) A snap shot at the onset of the impedance. (c) Undergoing in-plane vibrations that shows up as blade ghosts due to large disturbance relative to the imaging window. (d) After the blades go back to rotating in a uniform circle.

scatterers. The blade loses its flashing behavior due to loss of coherent return from the blade at flashing point, but we obtain larger visibility at all rotational angles. Figure 4.8 (a) shows a single snap shot of the blades rotating uniformly. Figure 4.8 (b) shows

smearing of the point scatterer as the blades have just encountered the impedance along their motion. Figure 4.8 (c) shows the ISAR image while the blades are undergoing vibrational motion. In this case, relative to the period of the turn-table, 66 seconds, the vibrational frequency is very large, 4 Hz. Therefore, the vibrations are not localized by a 24 degree window and show up as FM modulations spaced 0.4 m apart in cross range, corresponding to 4 Hz Doppler. These modulations appear as ghosts of the turbine shifted in cross range. Finally, Figure 4.8 (d) is the snap shot of the after the vibrations have been damped completely blade motion has gone back to normal. Here, the composite ISAR image is not shown due to the crowded nature of each snapshot, however, the vibrations can be clearly seen in a single image.

4.4 TURBINE ISAR CHARACTERISTICS IN THE PRESENCE OF GROUND

Real turbines are located on top of ground, and therefore turbine-ground interactions exist. In this section, the ISAR characteristics of the turbine blades rotating above an infinite ground plane are studied. With the presence of ground, additional returns due to single and double ground bounce are expected. The detailed physics of the ground interactions was studied and detailed in [73]. Single and double ground bounce are incorporated in our model by using image theory and appropriately incorporating the wave's travel distance for each interaction as the blades rotate [68]. The cases of turbine in the presence of stationary as well as moving ground are considered. The incident elevation angle is set to 20 degrees for the ground studies. The center frequency and the bandwidth width is kept the same as in Section 4.4, however, the frequency sampling is increased to 937.5 KHz to obtain a larger range window. The blade height is set to 60 m above the ground.

4.4.1 HIGHER ORDER MOTIONS IN THE PRESENCE OF A STATIONARY GROUND

Real turbines are located on top of ground, and therefore turbine-ground interactions exist. In this section, the ISAR characteristics of the turbine blades rotating above an infinite ground plane are studied. With the presence of ground, additional returns due to single and double ground bounces are expected. The detailed physics of the ground interactions was studied and detailed in [16]. Single and double ground bounces are incorporated in our model by using image theory [20] and appropriately accounting for the wave's travel distance for each interaction as the blades rotate. The cases of a turbine in the presence of a stationary as well as a moving ground are considered. The latter case may have implications in the Doppler features of offshore turbines situated on a moving sea surface. The incident elevation angle is set to 20 degrees for the ground studies. The center frequency and the bandwidth width is kept the same as in Section 4, however, the frequency sampling is decreased to 937.5 KHz to obtain a larger range window. The blade height is set to 60 m above the ground. Again, we focus on the blade contribution only.

The case of a stationary ground is analyzed first. Figure 4.9 are the simulated ISAR images for each motion. Figure 4.9 (a) shows the case of uniformly rotating blades in the presence of ground. We notice that in addition to the direct return, two additional sets of flashes encompassed by a circular tip halo are present. The first range-delayed return is due to the single ground-bounce effect. The second range-delayed return is due to the double ground-bounce effect. Figures 4.4.9 (b), (c), (d), and (e) respectively are the cases of in-plane vibrations, out-of-plane vibrations, blade flexing, and tower

vibrations. We notice that the key difference in presence of

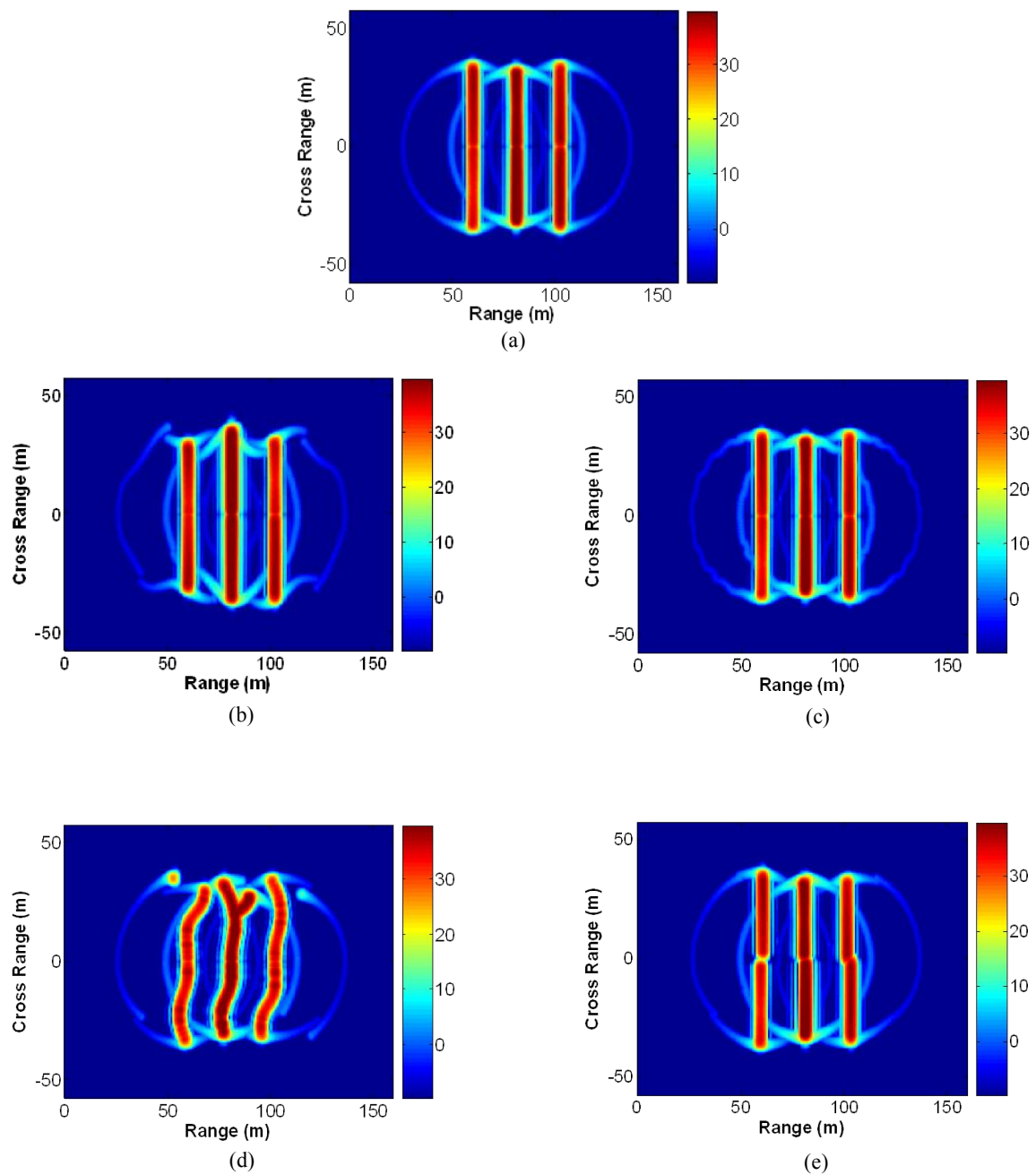


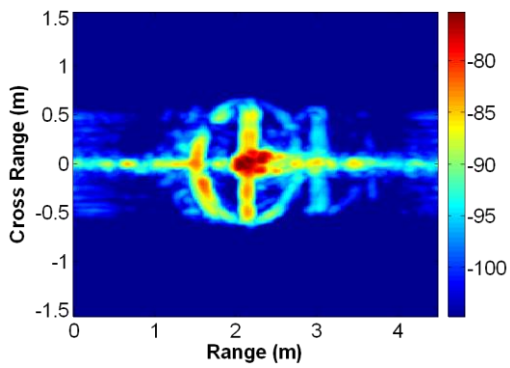
Figure 4.9. Composite ISAR images of turbine in the presence of ground. (a) Uniform circular rotation. (b) In-plane vibrations. (c) Out-of-plane vibrations. (d) Blade flexing. (e) Tower vibrations.

ground is that the single and ground bounce interactions are added to the image while the vibrational motions in each interaction manifest themselves in very similar manner as for the case of no ground.

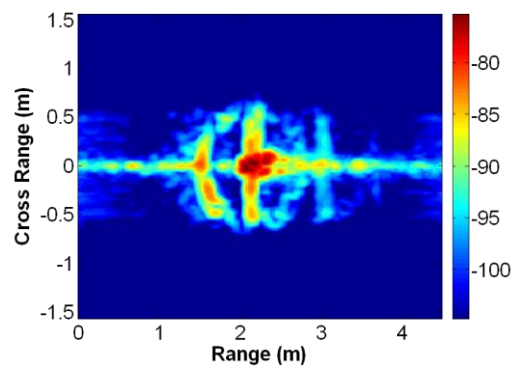
Experimental corroboration of the ISAR in the presence of ground for the case of turbine uniformly blades as well as the blades that undergo in-plane vibrations is provided by



(a)



(b)



(c)

Figure 4.10: Measured composite ISAR images of turbine in presence of ground. (a) Measurement set up. (b) Uniform circular roation. (b) In-plane vibrations injected.

Figure 4.10. Figure 4.10 (a) shows the measurement set-up. A large metal ground plane was added to the scene during the measurement. As with earlier measurements, we processed our raw data through a near-field to far-field transform algorithm to eliminate the phase distortion in the near field measurement. The direct and single ground bounce returns are observed to be present in the measured results. The single ground bounce is weaker in return because the wave decays in strength due to the larger space loss. Space loss is also the reason for the very faint double ground bounce return. Note that in the earlier simulation results, space loss was not included since the radar was assumed to be in the far field of the turbine. Figure 4.10 (a) shows the case of uniform rotation of the blades. Figure 4.10 (b) shows the case with injected in-plane vibrations. We observe the familiar features for the cases of direct and single ground bounce returns.

4.4.2 HIGHER ORDER MOTIONS IN THE PRESENCE OF MOVING GROUND

In this section, the composite ISAR images of the motions in the presence of a moving ground are constructed. The moving ground effects may make contributions in ground bounced returns for the case of offshore turbines situated on a moving sea surface. The detailed physics of the turbine motion in the presence of moving ground have been reported in [16]. Figure 4.11 shows the set of ISAR images for each motion in the presence of moving ground. In this case, the maximum ground displacement is set to 10 m and the vibrational frequency is set to 1.8 Hz. Although the ground parameters are exaggerated, they serve to clearly illustrate the features behind the motion of the ground.

Figure 4.11 (a) shows the case of a uniformly rotating turbine.

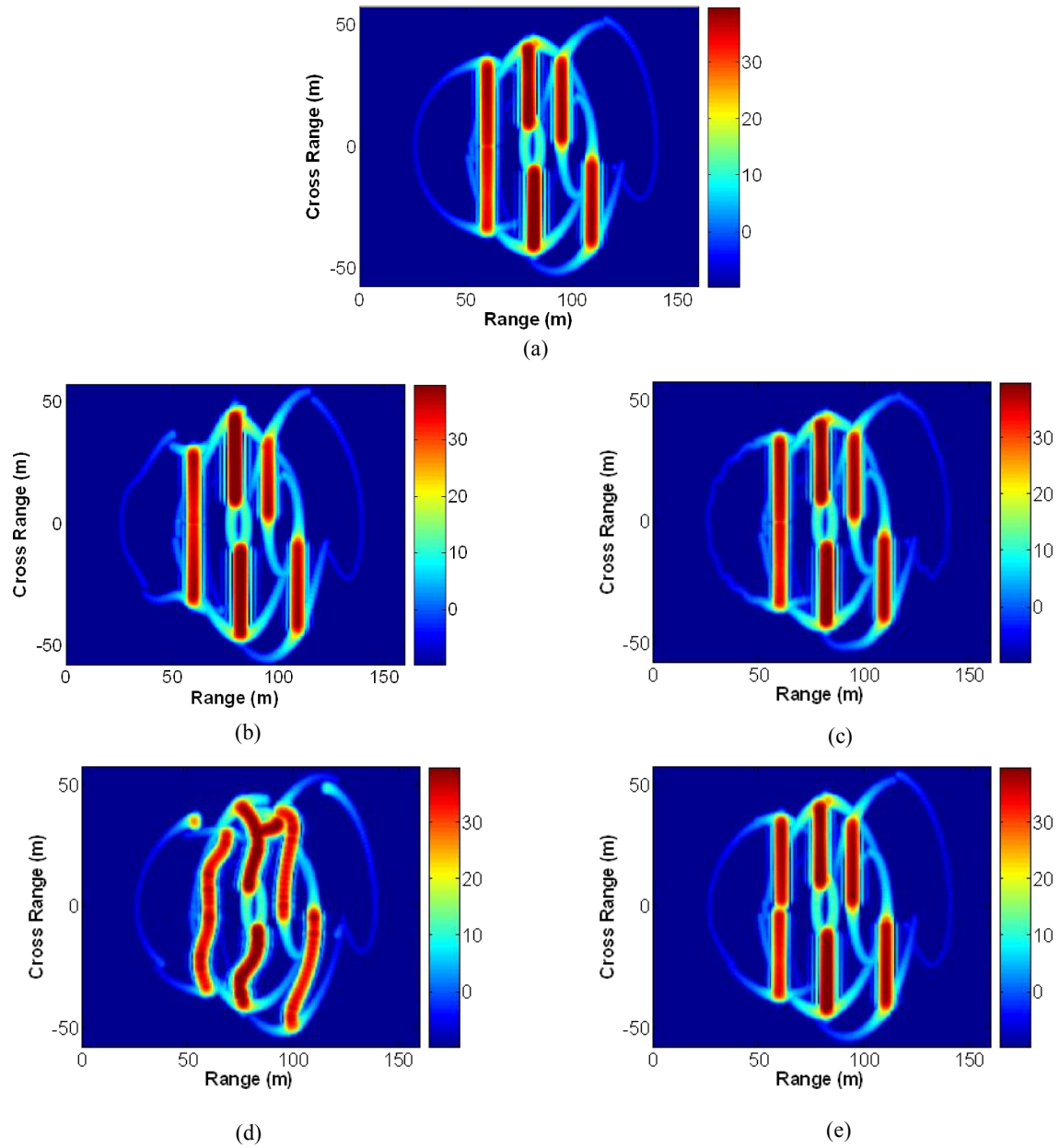


Figure 4.11. Composite ISAR images of turbine in the presence of moving ground. (a) uniform circular rotation. (b) in-plane vibrations. (c) out-of-plane vibrations. (d) blade flexing. (e) tower vibrations.

It is observed that the motion of the direct return is not affected by the motion of ground. The signature due to the ground motion is manifested in the single and double ground bounce. The ground motion is manifested in the single and the double ground bounce case in the form of a circle centered at 0 m in cross range. It is observed that the ground motion causes the flashes to ride on the ground motion circles. Also, the flashes are located at different range position due to the different path lengths the wave travels due to the ground motion. Figures 4.11 (b), (c), (d), and (e) respectively are the composite ISAR images of in-plane vibrations, out-of-plane vibrations, blade flexing, and tower vibrations motions. In these figures, we notice the ground bounce flashes riding on top of the ground motion, the asymmetry of the flashes in range, and similar tip distortion as for the case of static ground returns.

4.5 SUMMARY

We reported on higher order motions of turbine. First, motion models of higher order motions were proposed. The proposed higher order motions are in-plane vibrations, out-of-plane vibrations, blade flexing, and tower vibrations. Following the proposed models, the JTF characteristics of the models are presented and analyzed. Following the JTF characteristics, the analysis is broadened into the range dimensions and the ISAR characteristics of the motions are presented. Next, the ISAR characteristics

of a turbine in the presence of stationary and moving ground are reported. Selected simulations are corroborated by measurements.

Chapter 5: A Signal Filtering Technique to Remove Doppler Clutter Caused by Wind Turbines

5.1 INTRODUCTION

Previous chapters have probed in detail the wind turbine scattering characteristics. With increasing number and the size of individual turbines the clutter produced by turbines can be expected to increase as well. A number of studies have taken steps to probe and mitigate this problem. Previously, phenomenological studies have analyzed the Doppler clutter from a single turbine in-situ as well as in a controlled environment [18-21], [63]. Proposed mitigation measures to alleviate the clutter include introducing radar absorbing material in the turbine design, shaping of turbine components, as well as signal processing approaches [44-62]. However, detailed phenomenological as well as mitigation studies have yet to examine the scattering from a cluster of wind turbines, as is typically encountered on a wind farm.

In this work, we explore signal-processing based mitigation techniques to minimize Doppler clutter resulting from a cluster of wind turbines. Our approach employs the matching pursuit (MP) technique [77], which is a well-established algorithm to decompose a signal into a sparse expansion of basis functions. It has been applied in [78-83] to a variety of feature extraction problems, each employing its own physics-based basis. We first explore the feasibility of employing a chirplet basis to remove turbine clutter. Following the chirplet basis analysis, we propose a specialized basis function that models the backscattering from a single turbine's rotating blades. The MP technique is

applied to search for the parameters of the basis including the angular velocity and initial angular orientation of the turbine blades. The matched basis function is then subtracted from the radar signal to remove the backscattering from a single turbine. This process is iterated multiple times in order to remove the contributions from multiple turbines. We test this technique using simulated backscattered data from a single as well as multiples turbines, obtained using the high-frequency electromagnetic simulation code Ahilo [71].

The chapter is organized as follows. Section 1 discusses basis parameterization using the MP process. In Section 5.2 we construct a simple basis function and demonstrate the similarity of its time-frequency characteristics to a turbine's. Section 5.3 presents the attempt at removing turbine clutter using chirplet basis. In Section 5.4, we use the simplified basis function as training data and use MP algorithm to remove the simulated clutter. Section 5.5 presents the time-varying Doppler characteristics from a single turbine and a cluster of turbines obtained using Ahilo simulation. In Section 5.6, the filtering algorithm is tested using Ahilo data for a cluster of turbines. It is shown that the presence of multiple turbines overwhelms the return from a weak moving target. However, the target is revealed once the MP filtering algorithm is applied.

5.2 BASIS PARAMETERIZATION VIA MATCHING PURSUIT

In this section, we discuss the generalized process for basis parameterization. The MP algorithm is an iterative algorithm to parameterize an unknown signal based on basis projection. The implementation of the algorithm is as follows. The basis is first normalized such that the inner product of the normalized basis with itself is unity:

$$\phi'_k(t) = \frac{\phi_k(t)}{\sqrt{\langle \phi_k(t), \phi_k(t) \rangle}} \quad (4)$$

where the inner product is defined as

$$\langle \phi_k(t), \phi_k(t) \rangle = \int \phi_k(t) \phi_k^*(t) dt \quad (5)$$

The subscript, k , represents a basis with a particular set of ω and θ_o values.

In the first iteration ($n=1$) of the matching pursuit, the signal $E(t)$ is set to $E_n(t)$ and projected onto bases containing different appropriate parameter values. The basis parameters, that maximize the projection of $E_n(t)$ onto the basis are searched, i.e.

$$\{\omega_n, \theta_{on}\} = \arg \max \left| \langle E_n(t), \phi'_k(t) \rangle \right| \quad (6)$$

The corresponding projection coefficient of the basis is given by

$$c_n = \langle E_n(t), \phi'_n(t) \rangle \quad (7)$$

Upon finding the proper $\phi'_n(t)$, the contribution from this basis is subtracted from the signal:

$$E_{n+1}(t) = E_n(t) - c_n \phi'_n(t) \quad (8)$$

In the next iteration, $E_{n+1}(t)$ is set to $E_n(t)$ and the steps in Eqs. (6), (7), and (8) are repeated. This process is iterated to filter out as many turbine bases as required. In our case, this means that the process should continue until the turbine clutter is sufficiently removed and the contribution from the real target is revealed.

5.3 MP USING POINT SCATTERER TRAINING DATA

Having described the MP algorithm, we test the algorithm by projecting the point scatterer basis onto itself and perform iterative subtraction of the signal to attempt to eliminate the simulated clutter. Figure 5.1 shows a spectrogram of a cluster of four turbines with a weak point scatterer moving at a constant velocity buried inside the clutter.

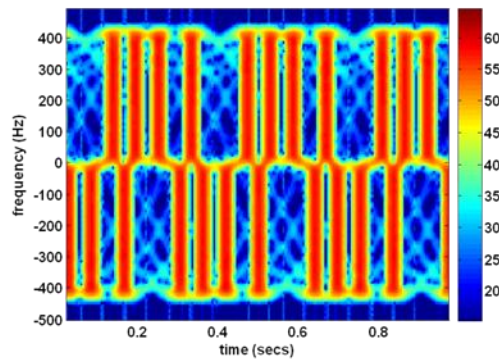
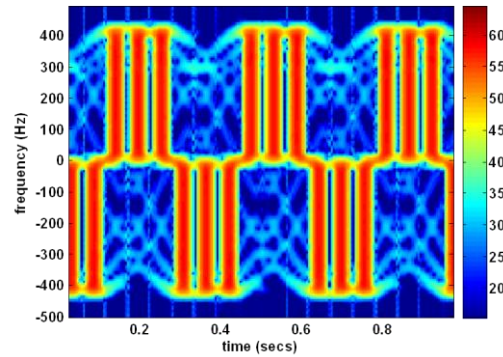


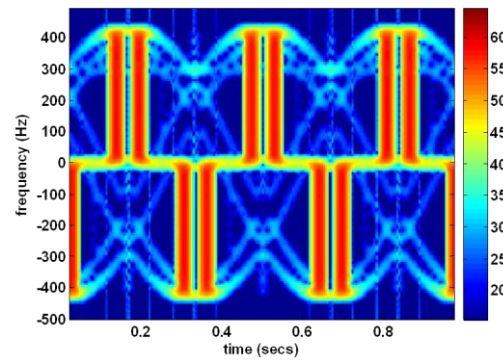
Figure 5.1: Spectrogram for four turbines with a weak target moving at constant velocity.

Having simulated the signal from a cluster of turbines, we now proceed to employ MP algorithm to eliminate the turbine clutter by projecting the by searching for the appropriate ω and θ_o for each turbine in the turbine basis. Figure 5.2 (a)-(e) respectively are the spectrograms of the residual signal after the 1st, 2nd, 3rd, 4th, and 10th iteration respectively. Figure 5.2 (f) shows the residual signal energy as a function of residual iteration. It is observed that the MP algorithm is successfully implemented in this case and the turbine clutter is eliminated completely by the tenth iteration. The subtraction

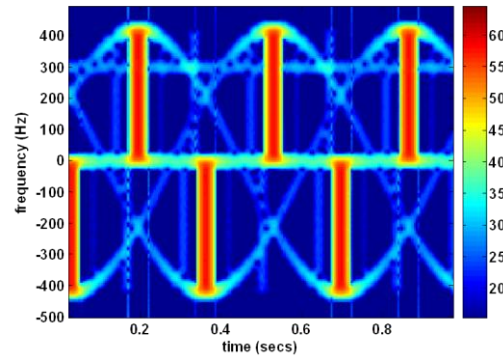
iteration causes the moving point scatterer to become visible as well.



(a)

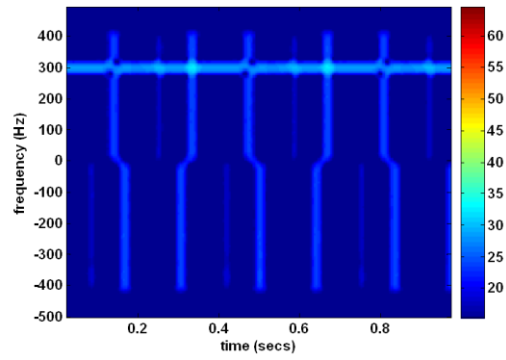


(b)

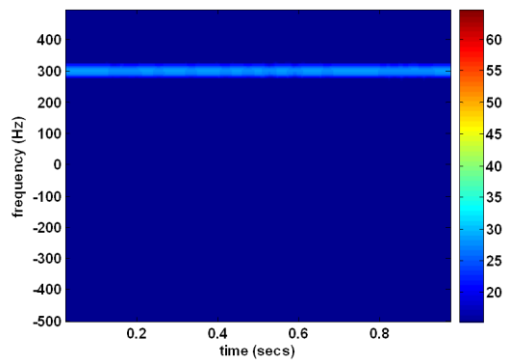


(c)

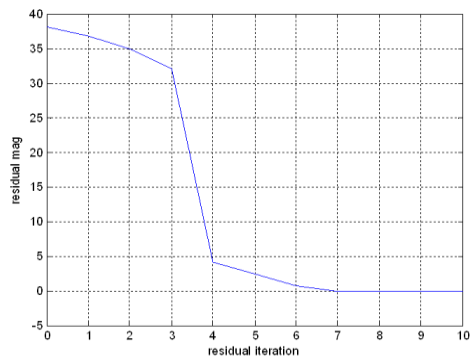
Figure 5.2



(d)



(e)



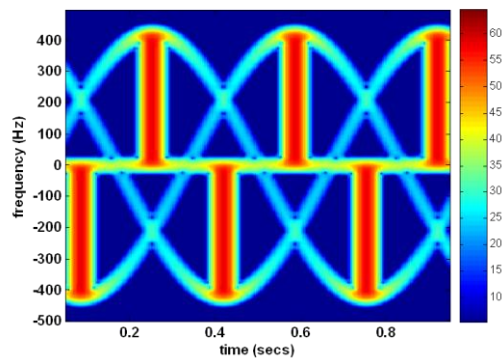
(f)

Figure 5.2: MP using point scatterer basis on itself. Residual after: (a) 1st iteration. (b) 2nd iteration. (c) 3rd iteration. (d) 4th iteration. (e) 10th iteration. (f) Residual energy as a function of iteration.

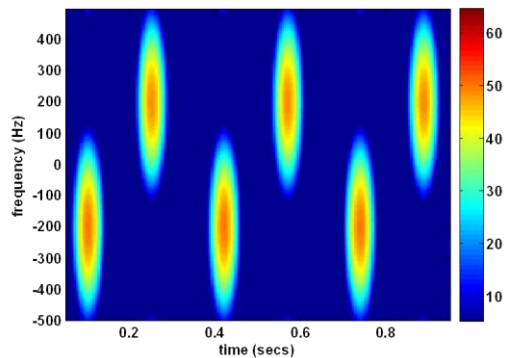
Figure 5.2 (f) shows that the residual energy decreases with each iteration and stabilizes after the 7th iteration. The leftover energy is largely from the moving point scatterer.

5.4 MP USING CHIRPLET BASIS

Having successfully implemented MP algorithm on training data, we now attempt to use the chirplet basis to subtract the turbine signal. The chirplet basis has been discussed in detail previously in []. Here we attempt to slightly modify the chirplet basis in order to introduce the flashing periodicity that is the trademark presence in the turbine signal.



(a)



(b)

Figure 5.3: Simulated signals. (a) Point scatterer basis. (b) periodic chirplet.

Figure 5.3 (a) and (b) respectively show the point scatterer simulated signal and the periodic chirplet signal. Although the chirplet basis is very flexible and is able to take on many arbitrary shapes, here we force it to resemble flashes in order to eliminate the most dominant turbine signatures.

Following the introduction of periodicity in the chirplet, we now set out to subtract the turbine clutter using our periodic chirplet. In our analysis, the Doppler extent and the centered point of chirplet are free parameters. These parameters are selected based on which parameter leads to largest clutter removal in a given iteration. Figure 5.4 (a), (b), (c), and (d) shows respectively the 1st, 10th, 50th, and 100th subtraction iteration of the chirplet project onto the turbine signal. Finally, Figure 5.4 (d) shows the residual energy as a function of each subtraction iteration. The spectrograms show that the largest decrease in the signal occurs after the first iteration. However, with increasing iteration, the spectrograms are not completely clean even after the 100th residual as shown in Figure 5.4 (d). Figure 5.4 (e) shows that although signal energy decreases as a function of residual iteration, the slope of the plot decreases as the iteration increases. Therefore, it is observed that although the chirplet basis can help reduce the turbine clutter, it doesn't completely eliminate it. From here on, we proceed with the point scatterer basis to try to eliminate simulated clutter using Ahilo.

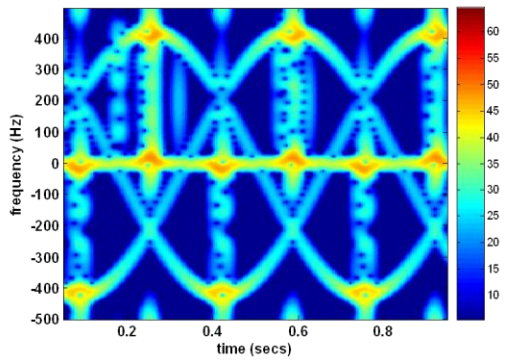
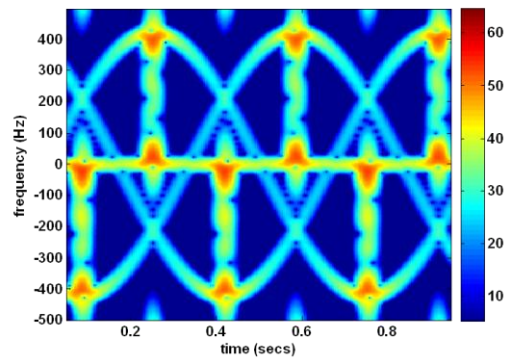
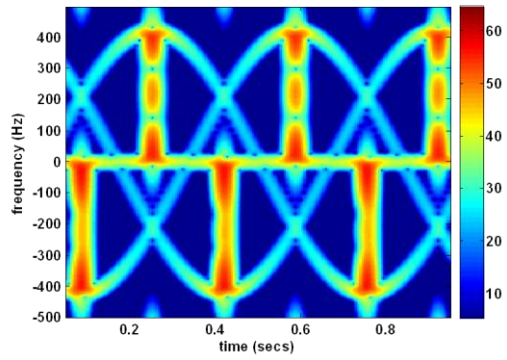
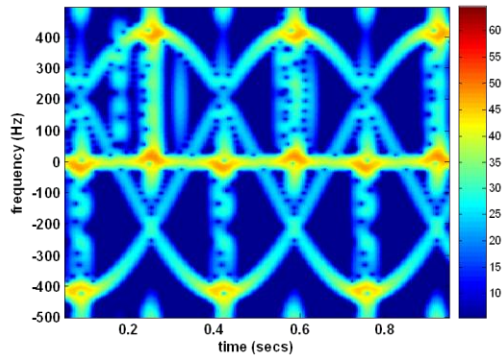
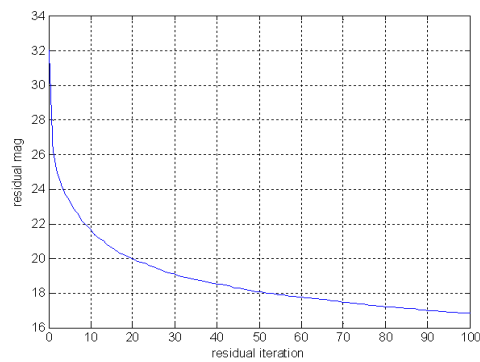


Figure 5.4



(d)



(e)

Figure 5.4: Iterative subtraction using chirplet basis. (a) 1st residual. (b) 10th residual. (c) 50th residual. (d) 100th residual. (e) Residual magnitude vs. residual iteration.

5.5 AHILO SIMULATIONS

We first examine the time-varying Doppler return from a single rotating wind turbine. The simulated signal is generated using the high-frequency electromagnetic ray-tracing code Ahilo. Figure 5.5(a) shows the CAD model of the turbine. It contains the simplified form of major components in a commercial turbine, including the 3 blades, the

nacelle and the tower. The size of the tower is 60 m while the radius of the nacelle is 2 m. The blades are modeled as rectangular plates of dimension 30 m x 1 m. The radar frequency is 1 GHz. During the Ahilo calculation, 3000 snapshots of the CAD model are generated, each with the blade position advanced by 0.12° relative to the previous position, for one complete revolution of the blades. The sampling is chosen to ensure an angular (or time) sampling of the return signal above the Nyquist rate. The total computation time is 35 minutes on a quad-core Intel i7-920 computer. Figure 5.5(b) shows the resulting spectrogram from the backscattering at edge-on incidence, or 90 degree yaw angle. This corresponds to the case when the radial velocity of the turbine blades relative to the radar is at its maximum. The blade rotation rate is assumed to be 12 rpm. The complex backscattered data are processed using the short-time Fourier transform (STFT) to arrive at the spectrogram. A Gaussian window is applied and a time window of 0.3 second is used to process the data. The spectrogram contains strong blade flashes that occur when the blade is perpendicular to the radar line-of-sight as well as weaker sinusoidal tracks that correspond to blade tip returns. Each of these tip “halos” weakens in strength as the blade rotates away from the flash position. The spectrogram also contains a strong DC component, which is due to scattering from the stationary tower and nacelle. In addition, white Gaussian noise (WGN) is introduced into the data, which shows up as a uniform background noise in the spectrogram.

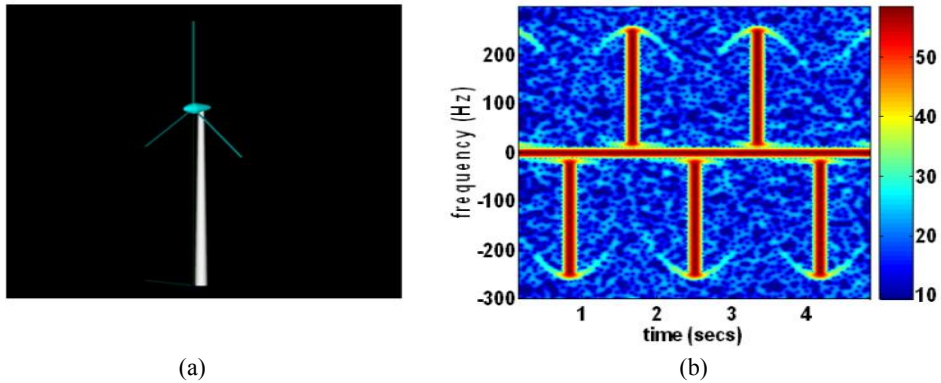


Figure 5.5: Simulation of a single turbine rotating at 12 rpm. (a) Turbine CAD model. (b) Spectrogram of the backscattered signal with WGN.

Next, we generate the Doppler clutter from a group of ten turbines. Since it is too computationally costly to compute the entire ensemble using Ahilo, we use a simple superposition of returns to generate the data. In making this approximation, we assume that there is no significant interaction between the turbines. Given the distance between the turbines (typically more than 6 blade lengths) and the small optical footprint of the turbines from edge-on, we believe this is not an unreasonable assumption. Figure 5.6 depicts the turbine returns from a cluster of ten turbines. Eight out of the ten turbines shown in the spectrogram are rotating at 12 rpm while the other two are rotating at 10 rpm. Backscattering from only a single turbine rotating at 12 rpm and 10 rpm are generated independently first. The other turbines seen in the signal are then added by appropriately time shifting the backscattered signal from a single turbine in order to give the blades of the other turbines a different starting angular orientation. In this case, the initial orientation angles of the blades for the turbines rotating at 12 rpm are 12, 24, 42, 60, 72, 90, 102, and 114 degrees. The initial orientation angles of the other two turbines

are 0 and 17 degrees. The return signal shown in Figure 5.6 also contains WGN as well as a weak moving target that is concealed in the spectrogram due to the dominating turbine signal. In Section 5, we will demonstrate that the moving target is revealed after applying the MP filtering algorithm.

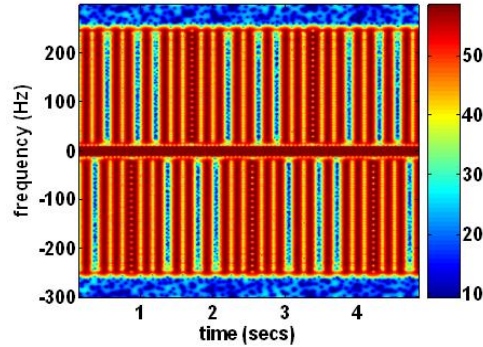


Figure 5.6: Simulated spectrogram of backscattering from a cluster of 10 turbines. Eight of the turbines are rotating at 12 rpm and the other two at 10 rpm.

5.6 BASIS CONSTRUCTION

In this section we present the steps of the basis construction and demonstrate its compatibility with the Ahilo-generated data. Mathematically, the signal from a single blade can be written as:

$$\phi(t) = \sum_{m=1}^M A_m (\hat{n}_m \cdot \hat{k}) \exp(-2jkR_m \sin(\omega t + \theta)) \quad (5.2)$$

Note that an extra dot product has been introduced in the magnitude, where \hat{n}_m is the surface normal of the blade and \hat{k} is the unit vector in the direction of the radar. The dot product between \hat{n}_m and \hat{k} controls the amount of scattering from the blades which is

expected to be maximum when the blade is perpendicular to the radar line-of-sight and zero when it is parallel. This model is consistent with the physical-optics contribution from an induced current element on the blade. Eq. (5.2) can be generalized to account for the signal from the three blades of a turbine by adding an additional index, l , in eq. (5.3), to account for the angular spacing between the blades:

$$\phi(t) = \sum_{l=0}^2 \sum_{m=1}^M A_m (\hat{n}_m \cdot \hat{k}) \exp(2jR_m \sin(\omega t + \theta_o + 2\pi l / 3)) \quad (5.3)$$

In the case of a turbine, given the initial position of one blade, θ_o , the angular spacing of adjacent blades is 120 degrees apart. Figure 5.7 shows the spectrogram of this basis function. The spacing of the adjacent scatterers is set to $\lambda/4$. Clearly the basis contains the blade flashes and tip halos very similar to those observed in Ahilo simulations. However, the basis function is missing the strong DC contribution of the tower and the nacelle. The mismatch due to the DC contribution can be eliminated by high pass filtering. Figures 5.8(a) and 5.8(b) show, respectively, the spectrograms of the Ahilo data and the basis function after high pass filtering. They closely resemble each other.

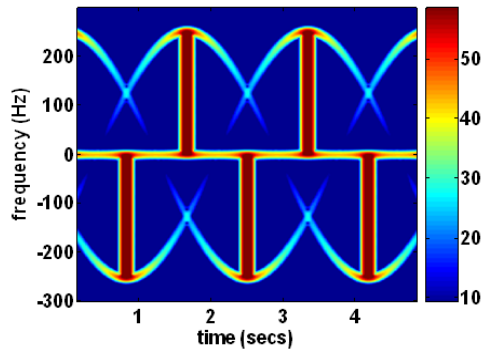


Figure 5.7: Time-frequency characteristics of the turbine basis.

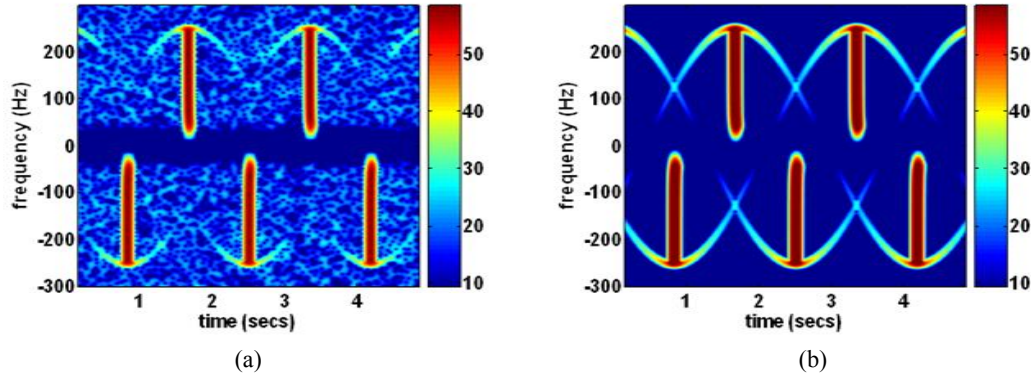


Figure 5.8: Single turbine backscattering, after high-pass filtering. (a) Ahilo data. (b) Turbine basis.

5.7 RESULTS AND DISCUSSION

The MP algorithm is first applied on Ahilo simulated data from a single turbine discussed in Section 5.6, Figure 5.8(a). Figure 5.9(a) shows the spectrogram after applying the MP filtering process. Clearly, the blade flashes and the tip halos are removed. Figure 5.9(b) shows the residual energy in the signal after each MP iteration. The energy of the original Ahilo return plus noise is 34 dB. The first MP iteration removes a large part of the signal, reducing the residual signal energy to 9 dB. This is very close to the energy of the background WGN, which is at 8 dB. The slight mismatch inherent in the make-up of the basis and the Ahilo signal is the reason for the 1dB difference from the noise floor. Since our simple physical basis has taken out the most

dominant feature of the signal in the first iteration, the residual magnitude thereafter is mostly noise and remains essentially unchanged.

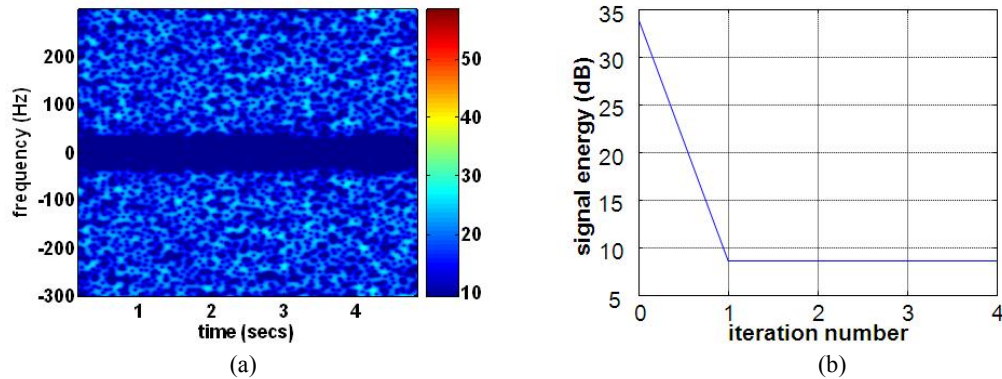


Figure 5.9: Signal filtering applied to the backscattering from a single turbine. (a) Spectrogram after MP filtering. (b) Signal energy as a function of iteration number.

Next, the MP filtering technique is applied to signal from a cluster of turbine discussed in Section 5.7. High-pass filtering is applied to remove the strong DC return seen in Figure 5.6. MP filtering is then applied iteratively in order to remove the contribution from each turbine. Figures 5.10(a), (b), (c), (d), and (e) are the original signal, the 1st, 4th, 9th, and 25th residual, respectively. It is evident that the turbine signal is very effectively removed in the iteration process. Figure 5.10(f) shows the signal energy vs. iteration number. The residual energy remains constant after 12 iterations and reaches a level at 13 dB. This is higher than the case for a single turbine and is again attributable to the fact that although the basis matches very well with the Ahilo signal, a very slight mismatch is present in the two signals. Figure 5.10(e) clearly reveals the

weak moving (constant acceleration) target hidden behind the multiple turbine clutter, which completely overshadows the target return in the original signal.

In the MP filtering process, it is found that the filtering efficacy is very sensitive to the slight mismatch of the parameters between the basis and Ahilo signal. Therefore, in order to find the precise parameter values contained in the signal, we have implemented a zoom-in algorithm to improve the efficiency of the search. The algorithm first searches for the parameters on a coarse grid and finds the approximate parameters that maximize the projection value, $|c_n|$. The next level of search is centered on the approximate parameters over a much smaller search space to allow for a finer search grid. This multi-level zoom-in procedure is repeated until the parameters are found with high precision.

The MP process could also be quite sensitive to the shape of the turbine blades. As reported in [4], different blade shapes can result in curved blade flashes. It is possible to modify our basis to account for more complex blade shapes. This can be accomplished by assigning each point scatterer a corresponding θ_o such that the blades of the basis better match those of the actual turbine. A preliminary step toward this measure is shown in Figure 5.11. Figure 5.11 (a) shows the case of turbine blades without curvature. Figure 5.11 (b) is the case of a curve blade while Figure 5.11 (c) is a case of a single blade with a triangular shape. Therefore, given the exact shape of the blade, the model is able to create any arbitrary blade shape.

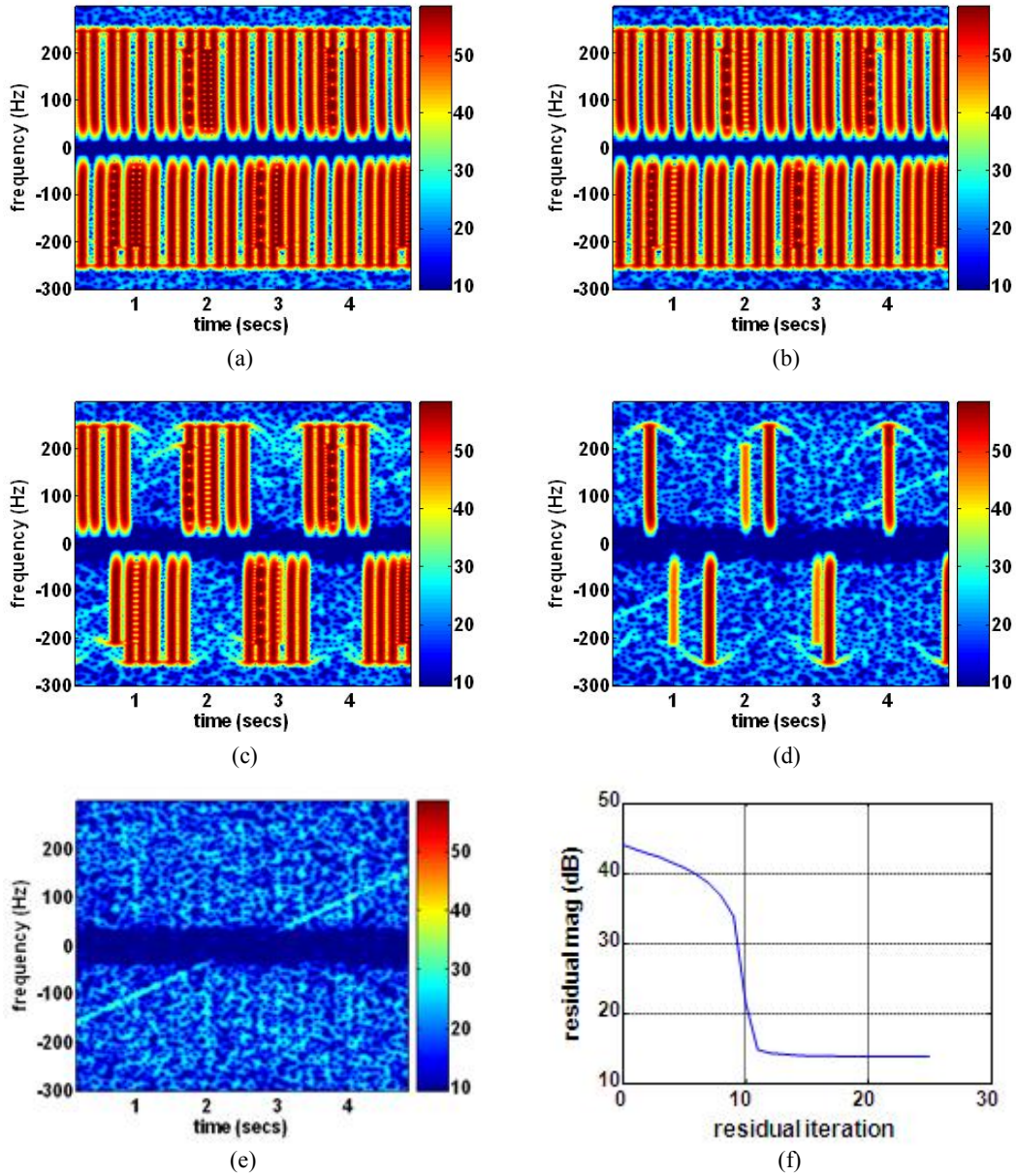
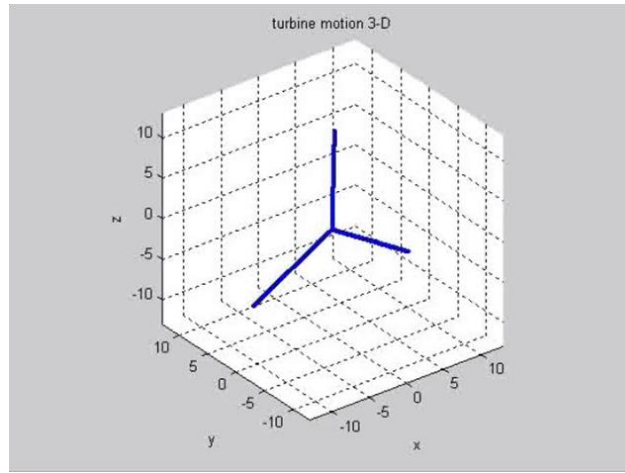
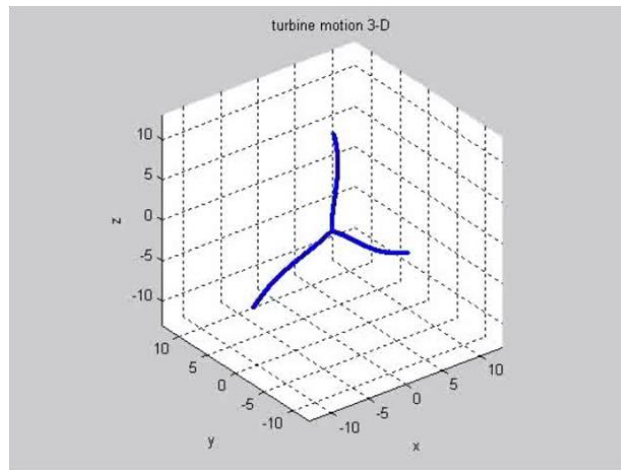


Figure 5.10 Signal filtering applied to the backscattering from a cluster of ten turbines. (a) Original signal after high pass filtering. (b) 1st residual. (c) 4th residual. (d) 9th residual. (e) 25th residual. (f) Signal energy as a function of iteration number.

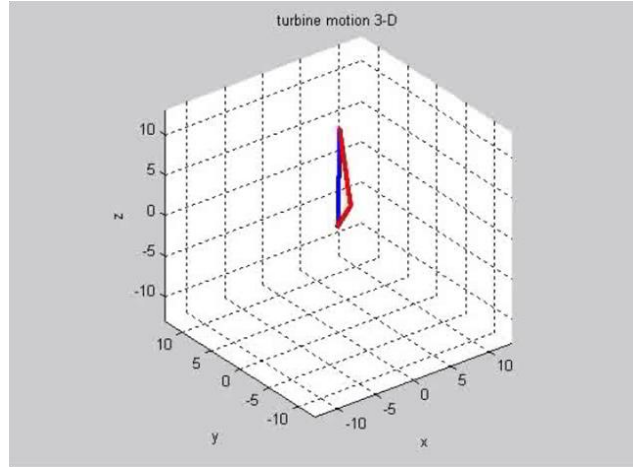


(a)



(b)

Figure 5.11



(c)

Figure 5.11: Introducing blade shape into the point scatterer basis. (a) Linearly shaped blade. (b) Curved blades. (c) Triangular shaped blade.

5.8 SUMMARY

In summary we proposed a technique to eliminate turbine clutter by employing the matching pursuit algorithm. First, the MP algorithm was tested by projecting the point scatterer basis onto itself to eliminate the simulated clutter. Second, attempts were made to eliminate the point scatter simulated turbine clutter using chirplet basis. The chirplet basis was moderately successful in eliminating the simulated clutter. Following that, we proceeded to eliminate Ahilo simulated turbine clutter using the point scatterer basis. The point scatterer basis was successful at eliminating the turbine clutter for

multiple turbines. The clutter elimination process was found to be robust and unaffected by the presence of white noise in the Ahilo simulated clutter.

Chapter 6: Radar Features of Wind Turbines at HF Frequency Region

6.1 INTRODUCTION

In addition to turbines interfering with military and ATC radars, concerns have been raised more recently regarding the role of offshore wind farms in diminishing the accuracy of the existing HF radars built for coastal monitoring [36, 37]. At the same time however, radar networks operating in the high-frequency (HF) region are being installed to help in construction of offshore wind turbines [37]. The dual role of the HF radar systems necessitates understanding the HF radar features of wind turbines in order to circumvent the unwanted turbine clutter produced by offshore wind farms. Since the wavelength at HF is comparable to the turbine size, scattering phenomenology may be distinct from earlier documented features [37]. The preliminary documentation of the turbine clutter features at HF was undertaken by [36, 37]. The aliased turbine clutter was observed to clutter the Doppler spectrum and interfere with the Bragg Peak.

In this chapter, we carry out a more extensive simulation study of the radar scattering from wind turbines in the HF frequency band. We broaden the scope of the work in [37] by studying the clutter behavior in the range-Doppler plane, extending the analysis to scattering from a wind farm instead of a single turbine, investigating potential shadowing created by the farm, and examining some detailed electromagnetic modeling issues. This paper is organized as follows. In Section 2, the modeling methodology and simulation results for a single turbine in the range-Doppler plane are presented first. Next, the analysis is extended to a wind farm modeled as an array of turbines. Section 3 discusses the aliasing of the Doppler spectrum as a result of limited pulse repetition

frequency (PRF) of typical HF radars. In Section 4, we study the electromagnetic shadowing caused by wind farms. In Section 5 we discuss some electromagnetic modeling details including the effects of the wire radius, the dielectric material comprising the blades, and the ocean surface. Section 6 is the conclusion.

6.2 RANGE-DOPPLER FEATURES

Full-wave electromagnetic simulation of a realistic, full size turbine is very time consuming even at HF frequencies, especially if time-varying scattering under blade rotation is to be modeled. To alleviate the computational burden, we model the wind turbine using thin wires, similar to the work of [37]. In Section 5, we shall further discuss the adequacy of using thin wires to model the structure. Full-wave simulations under the thin-wire model are carried out using the method of moment solver in the commercial software FEKO [84]. For our study, the following parameters are used: tower height=90m, blade length=63m, rotation speed=15rpm. The dimensions correspond to the nominal dimensions of a baseline 5-MW offshore wind turbine described in [85]. The entire turbine structure is assumed to be perfectly conducting. An infinite, perfect conducting ground plane is assumed to model the water surface, which is highly reflecting at HF frequencies. For the HF radar, we assume the antenna is a monopole located at 3000m from the turbine, and the transmitted wave is incident at edge-on relative to the rotation plane of the turbine blades. The frequency bandwidth is assumed to be 12-14MHz, leading to a radar range resolution of 75m. The wire radius in the thin-wire model is assumed to be 0.26m, which is the maximum allowable under the thin-wire approximation (1/80 of a wavelength at 14MHz). The range-Doppler image is acquired as follows. First frequency sweep data from 12-14MHz are collected in steps of

25KHz. The blades are subsequently rotated 3 degrees and the process is repeated for a complete rotation of the turbine blades. This corresponds to a time sampling rate of 30Hz at the 15rpm rotation rate. The simulated data in frequency and aspect are then 2-D Fourier transformed into the range-Doppler plane. A Hanning window is applied to both frequency and aspect dimensions of the data before the Fourier transform.

Figure 6.1 shows the resulting image in the range-Doppler plane due to a single turbine. The color in the figure is the strength of the scattered signal normalized into dBsm. The strongest feature seen is at the zero Doppler bin, which is due to the stationary tower. The turbine motion has ± 9 Hz of Doppler spread for the assumed 15rpm blade rotation rate at 14MHz. The periodic nature of the turbine blade return as a function of time causes the Doppler from the rotating blades to be localized in distinct Doppler bins spaced at 3 times the blade rotation rate, or 0.75Hz. It is observed that even though the electrical size of the turbine is on the order of the wavelength, range ringing due to resonant scattering is not very prominent.

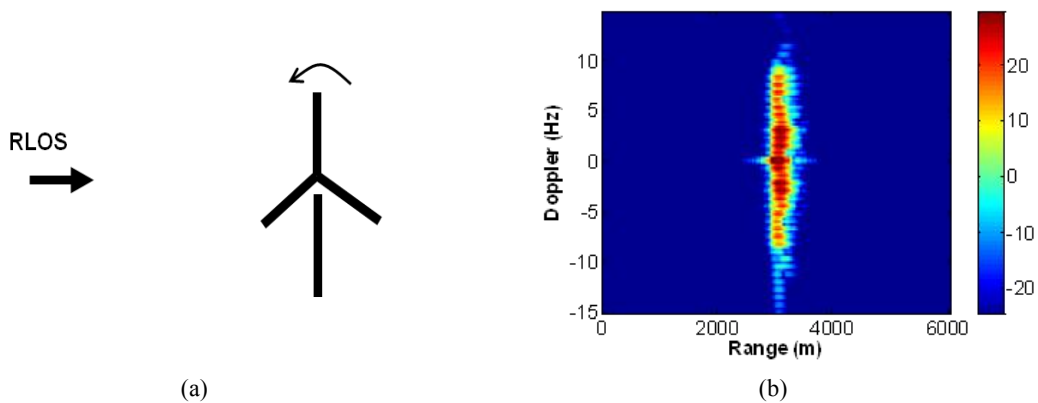


Figure 6.1. Radar features of a wind turbine rotating above an infinite ground plane. The turbine rotation speed is 15rpm and the radar frequency range is between 12 and 14MHz. (a) Simulation set-up using a thin-wire model. (b) Range-Doppler image.

We next simulate the case of an array of turbines. The spacing between each turbine is assumed to be 1000m and the source is located 3000m away from the center turbine. The simulation setup and the resulting range-Doppler image for this case are shown in Figure 6.2. Figure 6.2(a) shows the 3x1 turbine array setup. Note that the tower is not shown for clarity in this and the subsequent figures although it is always present in the simulation. In this case, the starting position of a blade of the center turbine is vertically upright while that of the top and bottom turbines is rotated by 20 and 40 degrees respectively. Figure 6.2(b) is the range-Doppler image for this case. The direct return from the center and the two outer turbines are located respectively in range at 3000m and 3162m.

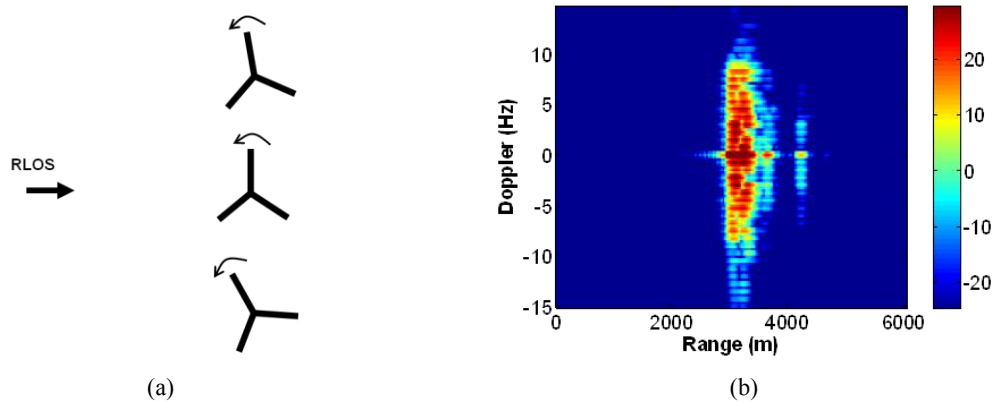


Figure 6.2. Radar features of a 3x1 wind turbine array. (a) Simulation set-up using thin-wire models. (b) Range-Doppler image.

In addition to the direction returns, additional weaker tracks delayed in range are observed that are due to multiple interactions between the turbines. Of the two range-delayed multiple returns seen, the earlier one is due to the interaction between adjacent turbines and is delayed by an extra 581m as a result. The later return is due to the wave that is re-scattered from a turbine at one edge of the array and is subsequently re-scattered by the turbine on the other edge before returning to the radar resulting in a range delay of 1162m. Note that these multiple returns are not only weaker, but they show less Doppler content, implying that majority of the multiples take place between the stationary tower structures.

Next, we study the case of a 1x3 turbine array. Figure 6.3(a) and (b) respectively are the turbine positions and range-Doppler image of the 1x3 turbine arrangement. The starting position of the blade of the center turbine is upright while those to its left and right are rotated clockwise by 20 and 40 degrees respectively. In this case, only the direct return from all the turbines is clearly seen. The multiple interactions are expected to be delayed by 1000m and 2000m respectively relative to the turbine return in the front.

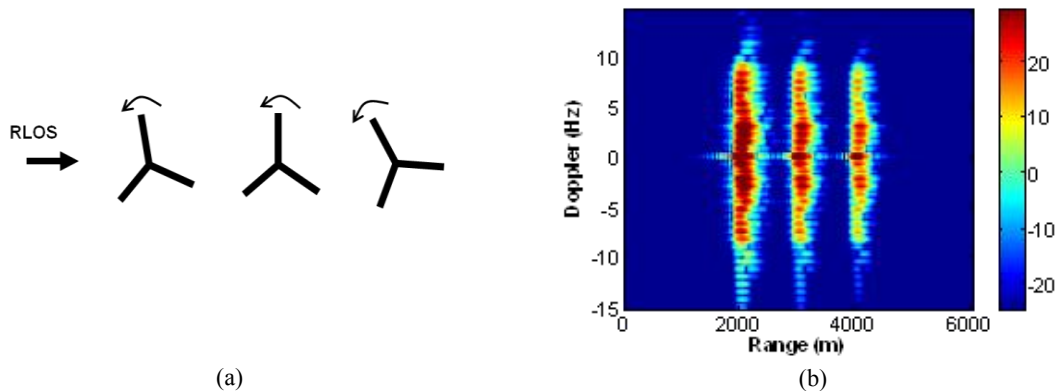


Figure 6.3. Radar features of a 1x3 wind turbine array. (a) Simulation set-up using thin-wire models. (b) Range-Doppler image.

Lastly, we simulate the case of a 3x3 turbine array. The starting position of a blade of the turbines in the second row is upright while the blades of the turbines in the first and third row are rotated 20 and 40 degree clockwise with respect to the initial blade position of the turbine in the front row as shown in Figure 6.2(a). Figure 6.4(a) shows the setup of the 3x3 array. Figure 6.4(b) shows the range-Doppler image of the array being excited at edge-on incidence. The features seen can be understood based on the understanding acquired for the case of 1x3 and 3x1 array cases. The return from each column of turbine is clustered together and each cluster is 1000m apart in range, which corresponds to the physical spacing of the turbine. Additionally, multiple interactions are observed that are due to the wave re-scattering from the tower as discussed for the case of 1x3 turbine array. Figure 6.4(c) shows the range-Doppler image of the 3x3 case when the position of the monopole excitation is moved such that it makes a 45 degree angle with respect to the horizontal and is located 3000m away from the center turbine. The maximum radial velocity of the blades relative to the radar decreases, resulting in a decrease in the maximum Doppler spread for the turbines. Six distinct turbines tracks are observed. The 3 missing tracks are due to the returns from turbines overlapping in range.

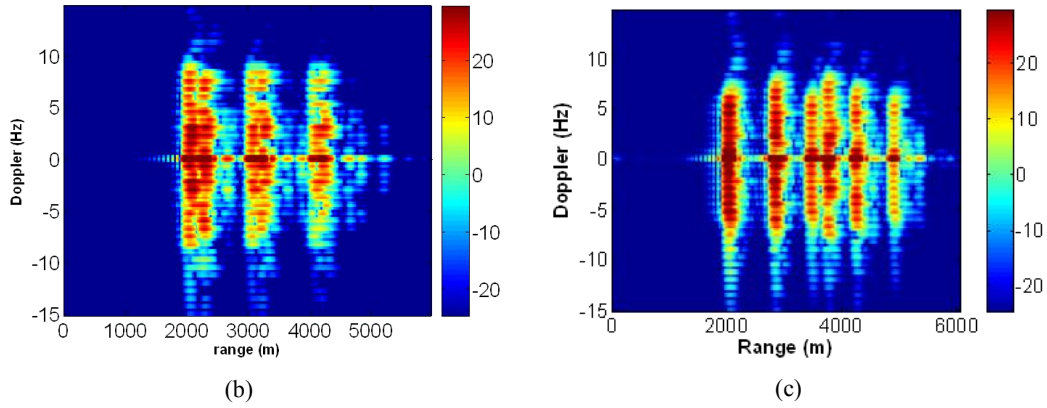
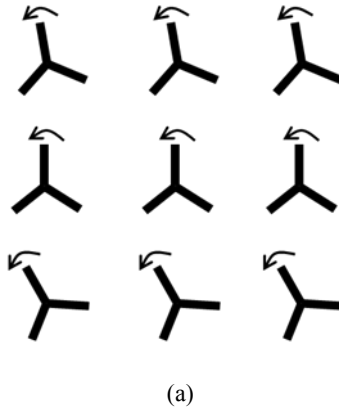


Figure 6.4. Radar features of a 3x3 wind turbine array. (a) Simulation set-up using thin-wire models. (b) Range-Doppler image under edge-on incidence. (c) Range-Doppler image under 45° oblique incidence.

Overall, we conclude that wind-farm-induced radar scattering is confined in the Doppler dimension to the maximum Doppler of the blades, and in range to the total range extent of the farm. Range-delayed returns due to either intra-turbine or inter-turbine multiple scattering, while present, are fairly weak.

6.3 DOPPLER ALIASING

The previous section showed non-aliased range-Doppler images of wind turbines. However, the typical PRF of the Coastal Dynamics Applications Radar (CODAR) is 2Hz. As a result, strong aliasing is possible from the turbine signal. This issue was discussed by Teague and Barrick in [37]. The aliasing crowds the Doppler spectrum and can make discerning the turbine features difficult from those of the ocean due to their comparable strengths. Here we simulate the aliasing effect in the Doppler spectrum of a single turbine at a single frequency, 13.5MHz, in order to get a simple and clear interpretation of the phenomenon.

Figure 6.5(a) shows the case of the unaliased Doppler spectrum for a turbine rotating at 13rpm. The signal is sampled at 30Hz. The expected Doppler harmonics are located at frequency bins spaced by the rotational frequency of the blades multiplied by three, or 0.65Hz, since the turbine has 3 blades. Figure 6.5(b) shows the Doppler spectrum for the same turbine sampled at 2Hz. As expected, the signal is severely aliased. The first Doppler line is located at the expected value of 0.65Hz while the next harmonic wraps back to -0.7Hz in the ± 1 Hz window. With the wrapping process continuing for all the higher harmonics, the spectrum becomes very crowded in the window.

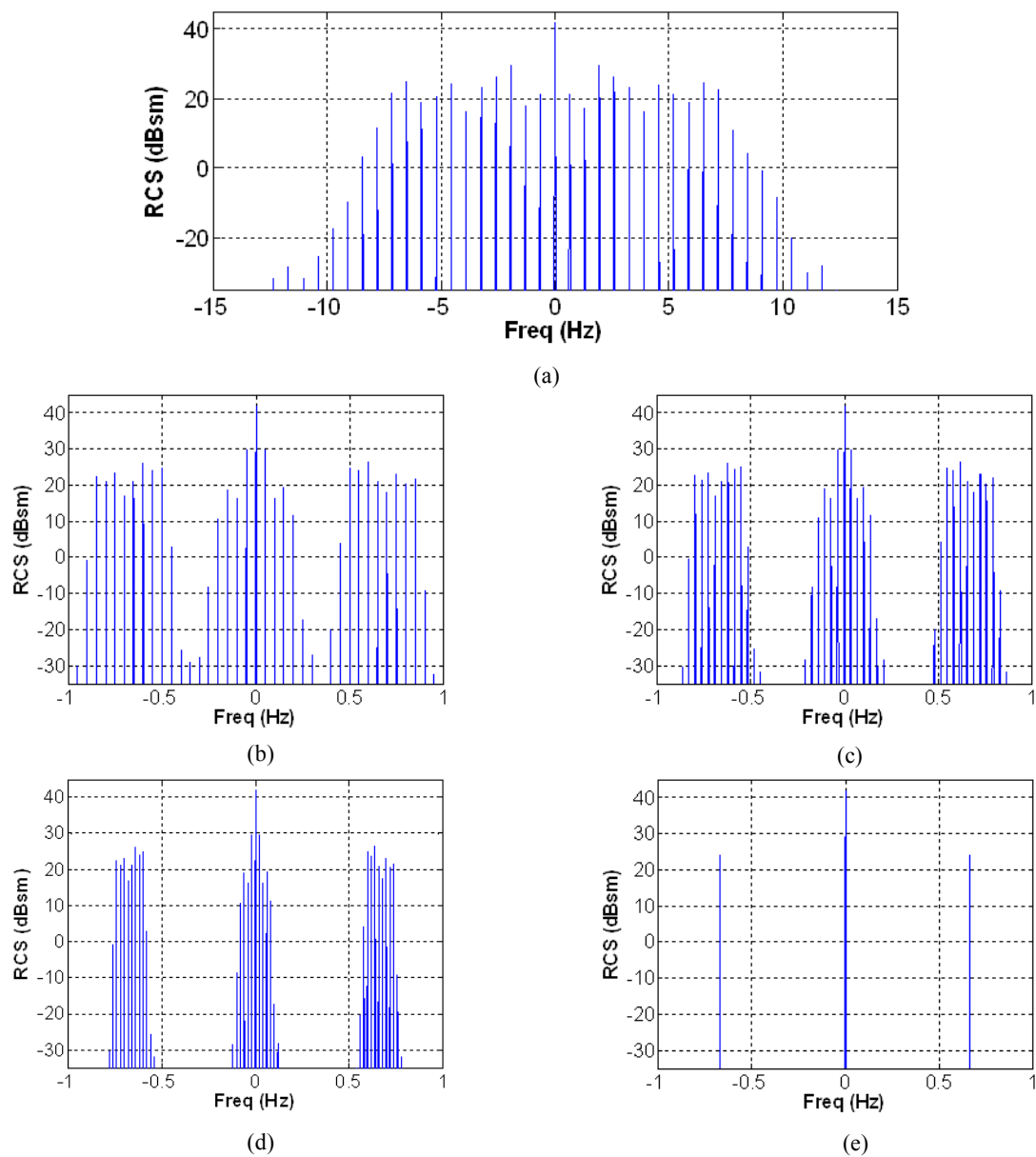


Figure 6.5. Doppler spectra of a rotating turbine at 13MHz. (a) 13rpm rotation speed sampled at 30Hz. (b) 13rpm rotation speed sampled at 2Hz. (c) 13.1rpm sampled at 2Hz. (d) 13.2rpm sampled at 2Hz. (e) 13.333rpm sampled at 2Hz..

Figures 6.5(c), (d), and (e) show the Doppler spectra of a turbine rotating at 13.1, 13.2, and 13.333rpm sampled at 2Hz. As the rotation rate gets closer to 13.333rpm, the Doppler lines begin to bunch up. At exactly 13.333rpm, the Doppler spectrum in Figure 6.5 (e) shows an interesting phenomenon where all the Doppler lines are completely focused into a single frequency bin at 0.667Hz, which leaves the spectrum very clean. This phenomenon was first observed in [37] and it offers the possibility to focus the Doppler clutter from wind turbines by varying the PRF of the radar. If these lines can be focused at a frequency away from the Bragg peaks due to ocean returns, this scheme could potentially alleviate the interference from wind turbines. Of course, it would require that the turbine rotation rate is fairly steady and that the PRF of the radar can be readily adjusted with high precision to achieve such Doppler focusing.

6.4 ELECTROMAGNETIC SHADOWING

In addition to examining the radar clutter produced by wind farms, it is also important to study the obstruction (or shadowing) effect produced by wind farms on the potential target (in this case the ocean surface) return. To do so, we simulate the field within and around a wind farm at 13MHz using FEKO, and compare the results to the field strength in the absence of the farm. Since we expect the tower structure to give the strongest shadowing effect [86], a static blade configuration is assumed in the simulation. Otherwise, the same wind farm parameters are used. The near field plots in two dimensions in the vicinity of a 3x1 turbine array are shown in Figure 6.6. The horizontal and vertical axes respectively are the range and cross range measured in meters. The fields are calculated at increments of 10 m in both range and cross range. Figure 6.6(a)

shows the field plot (in dB) from a monopole above an infinite conducting plane located on the left at 3000m away from the plot origin. Figure 6.6(b) shows the total field plot in the near field of a 1x3 turbine array. Figure 6.6(c) plots the difference between the field strengths in 6.6(a) and 6.6(b). From the figure, it can be seen that the depth of the electromagnetic shadow, which is the deepest immediately behind each turbine, is less than 2dB at this frequency.

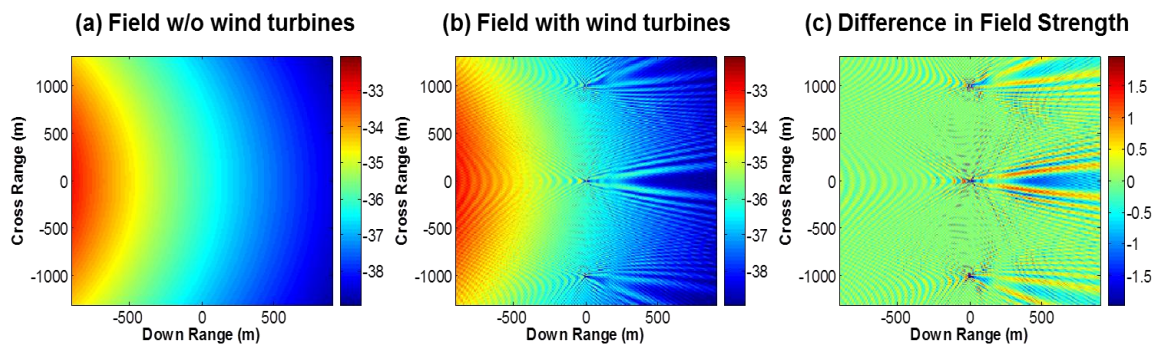


Figure 6.6. Shadowing effect of wind turbines. (a) Field without wind turbines. (b) Field with a 3x1 wind turbine array. (c) Difference in field strength with and without the turbines.

Additional results are generated for a 3x3 wind farm and shown in Figure 6.7. Similar to Figure 6.6, Figure 6.7(a) shows the field without the farm, 7(b) shows the total field with the farm, and 7(c) shows the difference between the two field strengths. The results are similar to those observed in Figure 6.6. We do notice a moderate increase in shadow depth for the turbines in the middle row. This means that when a series of turbines are perfectly lined up with respect the radar line-of-sight (RLOS), the shadowing depth gets progressively darker. However, even in this case, the darkest shadow is still

within 2dB of the unperturbed field, and is confined to immediately behind each turbine. Figure 6.8 shows the situation for the same 3x3 farm when the radar is moved to a 45 degree oblique angle with respect to the center of the farm. Similar findings are observed.

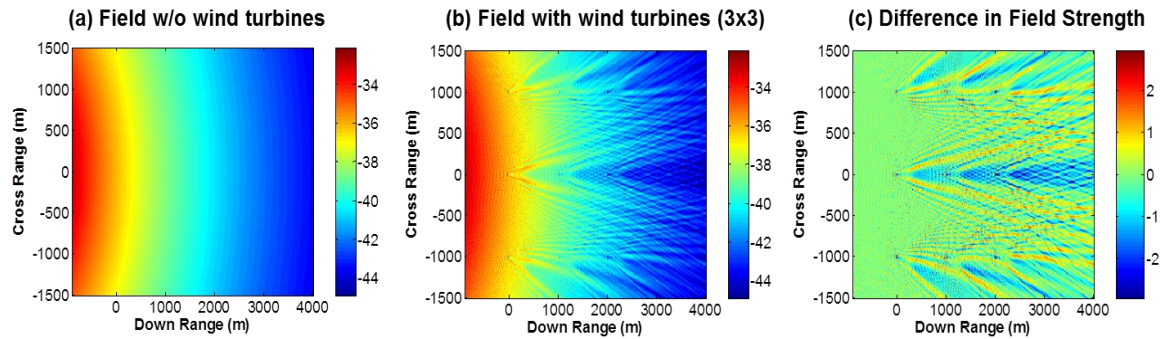


Figure 6.7. Shadowing effect of wind turbines. (a) Field without wind turbines. (b) Field with a 3x3 wind turbine array. (c) Difference in field strength with and without the turbines.

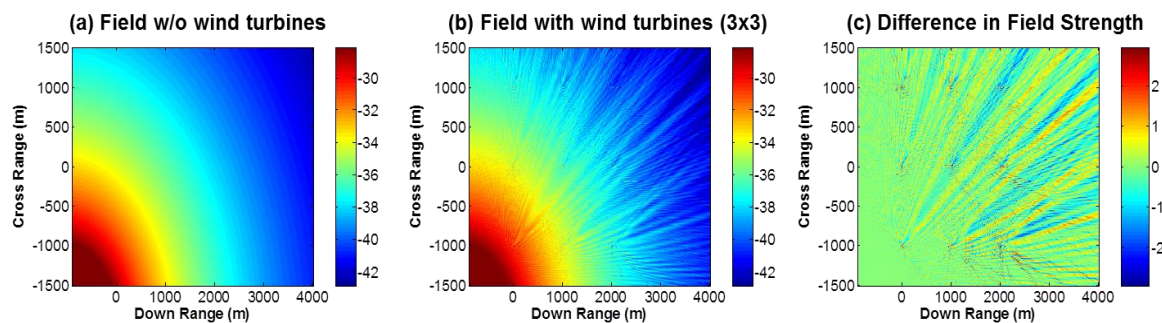


Figure 6.8. Shadowing effect of wind turbines under 45° oblique incidence. (a) Field without wind turbines. (b) Field with a 3x3 wind turbine array. (c) Difference in field strength with and without the turbines.

6.5 MODELING DISCUSSION

In this section, the electromagnetic modeling methodology used to generate the simulation results will be discussed in more detail. First the thin-wire approximation is used in this study to save computation time. To address the accuracy of the thin-wire model, we compare the thin-wire result to that from a full surface-mesh model. The components in the surface-mesh model are modeled as circular cylinders with radius of 0.26m. The length of the components in each model is the same as in the previous sections. Figures 6.9(a) and 6.9(b) show the range profiles generated from the thin-wire and surface-mesh models, respectively. A Hanning window is used on the 12-14MHz data before the inverse Fourier transform. The resulting radar cross section (RCS) is expressed in dBsm. Figures 6.9(c) and 6.9(d) show the range-Doppler plots generated from the thin-wire and surface-mesh models, respectively. It can be seen that the results from the two types of modeling are very similar. Of course, the thin-wire model takes much less time to simulate (a factor of approximately 40 for a 3x3 wind farm).

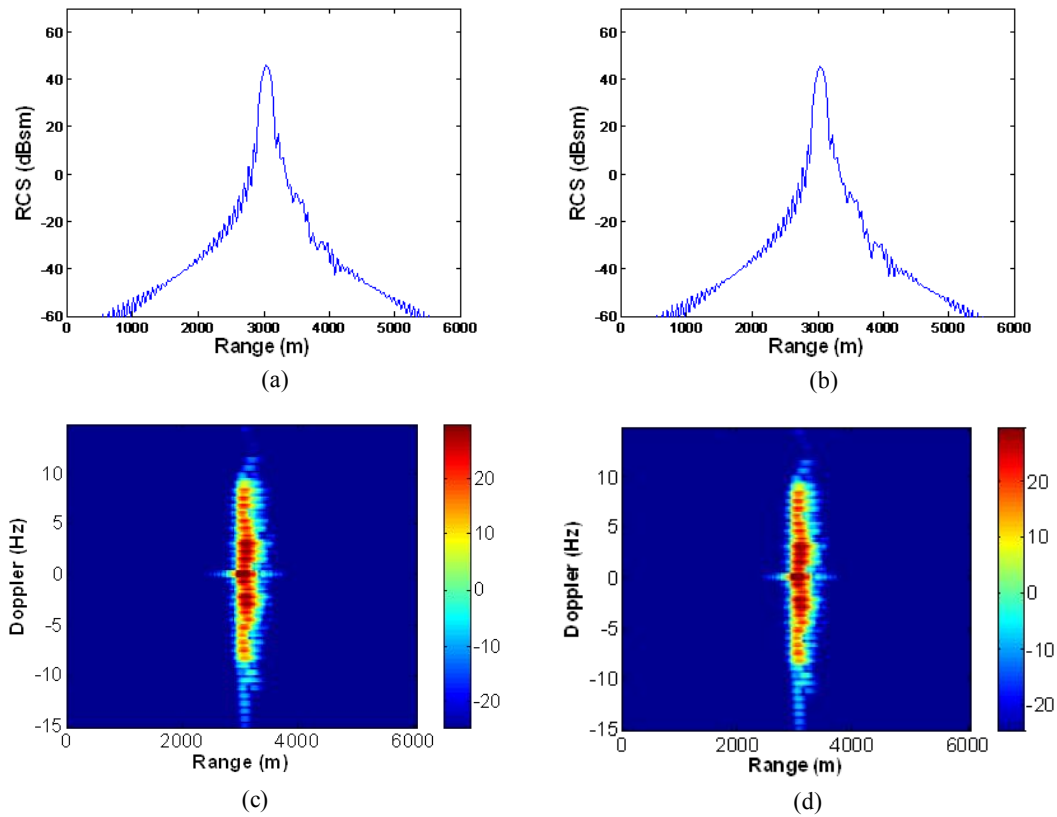


Figure 6.9. Comparison between the full surface-mesh model and the approximate thin-wire model computed using FEKO. The blades and tower of the model have a radius of 0.26m. (a) Range profile from the surface-mesh model. (b) Range profile from the thin-wire model. (c) Range-Doppler plot from the surface-mesh model. (d) Range-Doppler plot from the thin-wire model.

Next, we investigate the effect of wire radius in the thin-wire model. To remain within the validity of the thin-wire approximation, the upper limit on the wire radius is

$\lambda/80$, or 0.27m at 14MHz. However, as Figure 6.10 shows, there does not appear to be a significant change in the RCS level as the cylinder radius is extended from 0.27m to 1m for the full-surface mesh model. In this case, only the 90m cylindrical tower structure is analyzed for simplicity. On the other hand, when the thin-wire radius is reduced from 0.27m down to 0.027m then to 0.0027m, there begins to be stronger resonant ringing in range, as shown in Figures 6.11(a) to 6.11(c). This is caused by the strongly guided traveling wave along a very thin wire, which makes multiple traversals along the wire. This traveling wave is not expected to be strongly supported in a real turbine structure due to both its larger radius and non-uniform cross section. Therefore, it is a good practice to keep the wire radius at close to its upper limit ($\lambda/80$) for the thin-wire modeling of wind turbines.

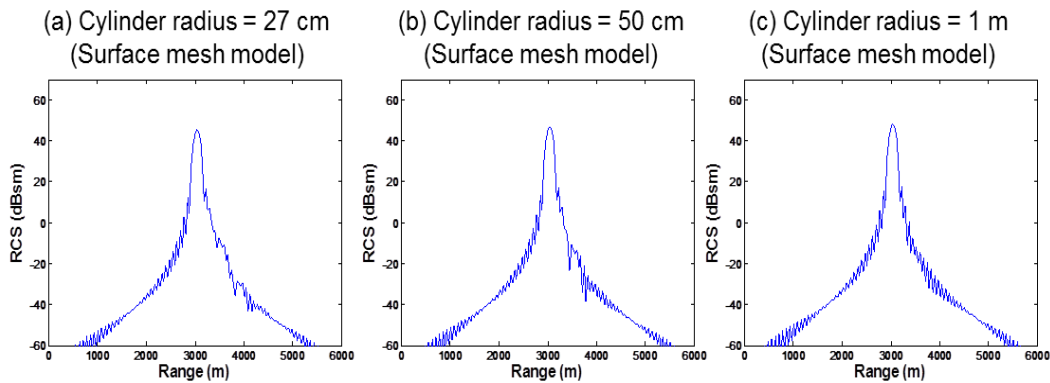


Figure 6.10. Effect of increasing the cylinder radius in the surface-mesh model on the range profile of a 90m tower. The frequency range is from 12 to 14MHz.

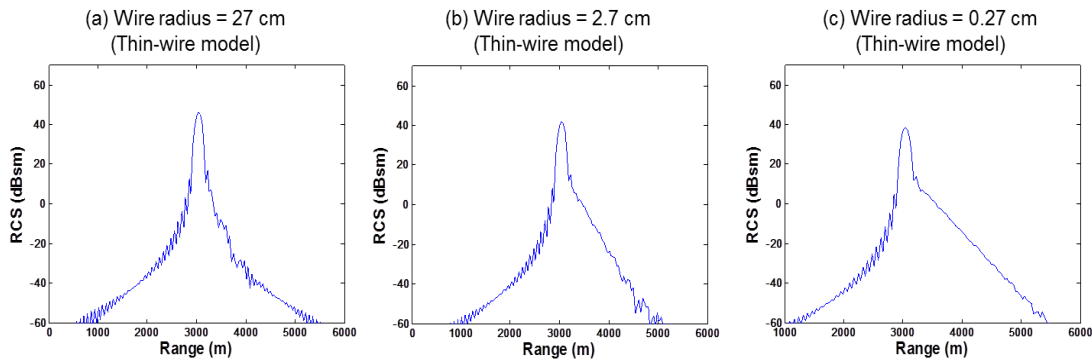


Figure 6.11. Effect of decreasing the wire radius in the thin-wire model on the range profile of a 90m tower. The frequency range is from 12 to 14MHz.

Next, we investigate the effects of non-perfect-conducting material of the turbine components on the scattered signal from the turbine, since perfect conducting wires were used to generate the results in the previous sections. Figure 6.12 presents a comparison between a dielectric and a perfect electric conducting (PEC) cylinder of height 90m and radius 1m computed using the surface mesh model. The full-wave surface integral equation solver is used in FEKO for the dielectric cylinder. The material is assumed to be carbon fiber and the real part of the relative permittivity is taken to be 20 while the imaginary part is 0.15 [87]. Figures 6.12(a) and (b) show the frequency responses for respectively the dielectric and PEC cases from 10 to 20 MHz. It is observed that the dielectric scattering is higher by about 3 dB. The conducting cylinder shows slight undulations over the whole range. Figures 6.12(c) and (d) are the corresponding range profiles of the 12-14MHz data of the two cases. It is observed that the range characteristics are largely similar, except the range peak due to the dielectric material is about 3dB higher than the case of the PEC cylinder.

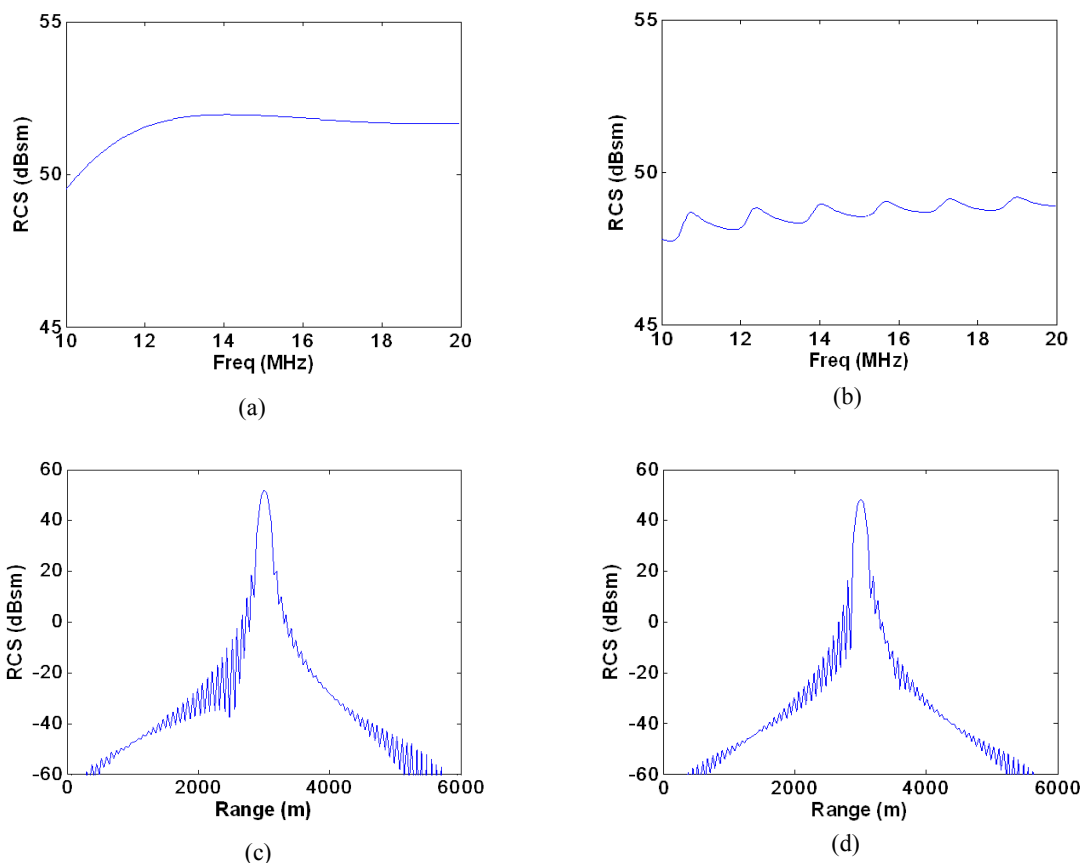


Figure 6.12. Effect of turbine material on the RCS. (a) Dielectric cylinder frequency response. (b) PEC cylinder frequency response. (c) Dielectric cylinder range profile. (d) PEC cylinder range profile.

Finally, we examine the effect of the ground plane, which is used to model the sea surface, on the observed RCS level. A detailed study on the ground plane effect to wind turbine RCS at microwave frequency range was reported in [64]. Here, we extend the analysis to the HF frequency range. For the configuration at hand where the transmitter is a monopole located on the surface of the ground plane, the scattered field strength is

approximately increased by a factor of four from that of the free-standing structure. This comes from the additional single and double ground bounced returns as shown in Figure 6.13(a). Due to the vertical polarization and the on-surface nature of both the transmitter and the scatterer, these four contributions add coherently in phase. This factor-of-four amplification in field leads to a factor of 16, or 12dB, increase in RCS. Of course, this argument ignores the interaction between the scatterer and its image. Figures 6.13(b)-(c) illustrates this point. The simulation is conducted both with the ground (Figure 6.13(b)) and without the ground (Figure 6.13(c)) and the range profiles are plotted for different blade rotation angles. The difference in dB scale between the result in Figure 6.13(b) and four times that of Figure 6.13(c) is shown in Figure 6.13(d). We can see that the difference is not large, demonstrating that the approximate 12dB argument is obeyed. Nonetheless, the difference is not zero, as there exist non-negligible higher-order interactions between the turbine and the ground plane.

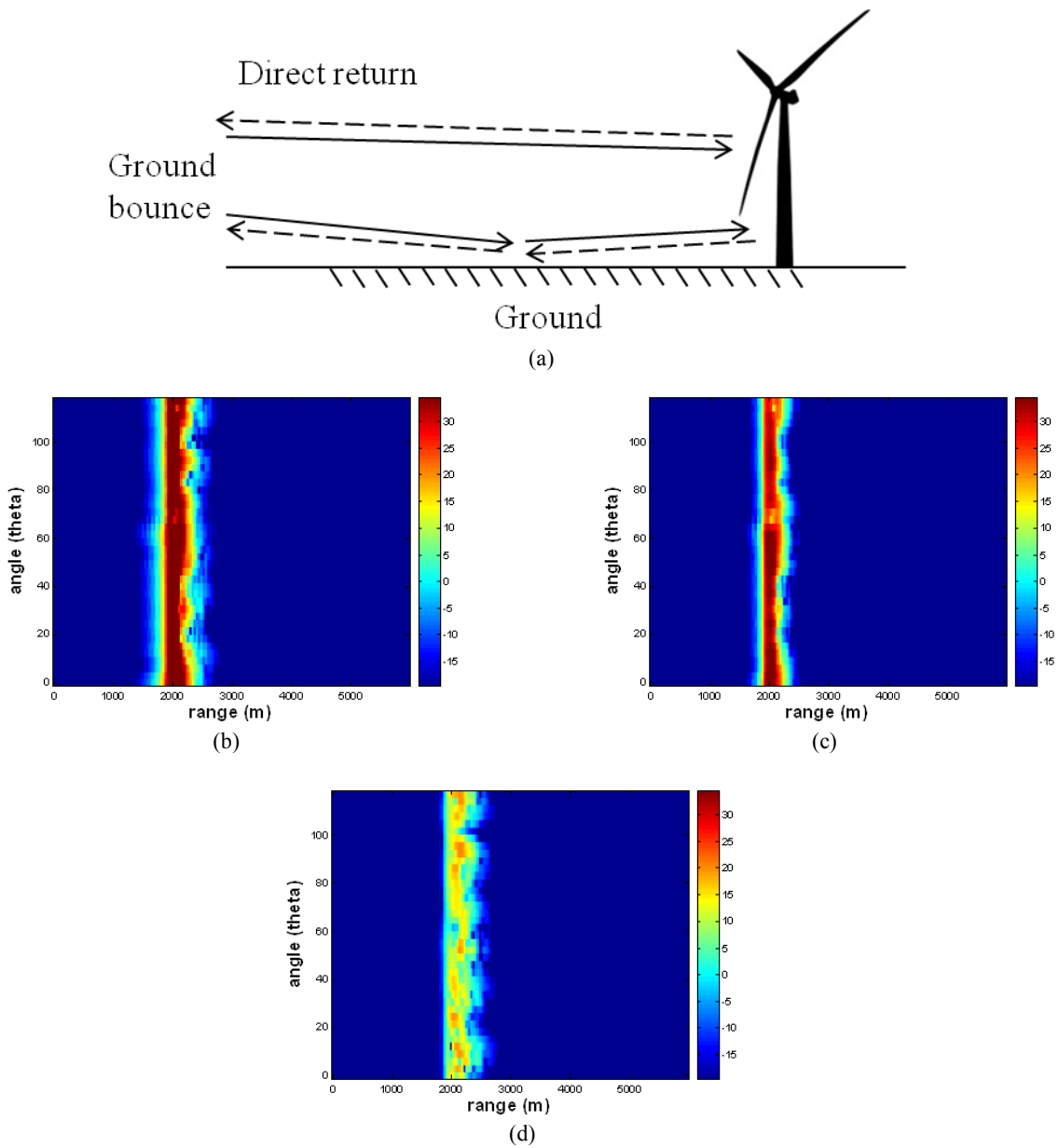


Figure 6.13. Effect of the conducting ground surface on the turbine RCS. (a) Possible ground bounce mechanisms. (b) RCS versus range and blade angle in the presence of ground. (c) RCS versus range and blade angle without ground. (d) Difference between the with-ground case and four times the without ground case.

6.6 SUMMARY

The radar features of a single and an array of wind turbines have been simulated and studied in the HF frequency band. It was found that wind-farm-induced radar scattering is confined in the Doppler dimension to the maximum Doppler from the blades, and in range to the total range extent of the farm. Range-delayed returns due to either intra-turbine or inter-turbine multiple scattering, while present, are fairly weak. It was also found that when the radar PRF is low compared to the maximum Doppler from the blades, strong aliasing occurs that results in a crowded Doppler spectrum. If the PRF of the radar can be precisely controlled relative to the blade rotation rate, it may be possible to focus the Doppler lines into a few Doppler frequency bins. In addition, the overall shadowing effect of a wind farm was found to be not very prominent in the HF regime. The shadow depth is at most 2dB in the immediate vicinity behind each turbine away from the radar. There is a moderate increase in shadow depth behind a turbine that is in the shadow of another turbine. Finally, electromagnetic modeling details including the effects of thin-wire modeling, non-conducting turbine components, and the presence of a conducting ground surface were examined.

Chapter 7: Conclusions and Future Work

7.1 CONCLUSIONS

This dissertation first investigated the radar scattering features from wind turbine scaled models. Dynamic CW radar measurements were performed in the laboratory and the resulting data were analyzed using the short-time Fourier transform to study their Doppler scattering features. For the 1:160 scaled model turbine, it was found that our measurements captured the gross Doppler features including blade flashes and tip halos observed in a large wind turbine reported in [11-15]. For the 3-arm wire model, additional multiple scattering and near field effects were observed and interpreted with the aid of simulations performed using NEC. It was also found that only multiple scattering gives rise to non-zero forward Doppler. For the Bergey Windpower turbine, we observed unequally spaced, curved flashes. They are attributable to the unique shape of the turbine blade.

Second, the Doppler characteristics of electromagnetic backscattering from a wind turbine in the presence of ground are simulated and studied. We employed a ray-tracing simulation and image theory to acquire backscattered data. It was shown that the presence of ground gives rise to two additional blade flashes between the radar and the turbine. No other flashes or higher-order features with strong intensities were found. The observed features were corroborated with measurements of a simplified wire model. The effects of a moving ground were also simulated and interpreted in detail. Although the geometries analyzed in this paper are for a perfectly conducting, flat ground plane, an effective reflection coefficient approach can be used to model non-perfect-conducting, rough, or even non-flat terrains. Appropriate reflection coefficient can be applied to

modify the strength of the return signal based on the size of the Fresnel zone projection on the ground relative to the scale-length of the ground roughness. However, that is not expected to change the Doppler features reported in this paper.

Next, the radar scattering characteristics of wind turbine's higher order motions were modeled and analyzed using a simplified point scatterer basis. The higher order motions model include in-plane vibrations, out-of-plane vibrations, blade flexing, and tower vibrations. We used the model to simulate the time frequency and ISAR characteristics of the motions. The cases of an isolated turbine and turbine in the presence of stationary and moving ground were studied. The principles of image theory were used to incorporate ground effects into our point scatterer basis. Selected simulated cases are corroborated by measurements.

Having studied the features of wind turbines, we next took some preliminary steps towards clutter mitigation. A simple physics-based model of the radar backscattering from a wind turbine described in chapter 4 was employed. This basis was used in conjunction with the matching pursuit algorithm to iteratively remove the Doppler clutter due to a cluster of wind turbines. The algorithm was tested using data generated using the high-frequency electromagnetic simulation code Ahilo. It was shown that the presence of multiple turbines overwhelmed the return from a weak moving target. However, the target could be revealed once the filtering algorithm was applied.

Finally, we reported on the turbine radar features in the HF frequency region. We first justified modeling of a turbine using wires. We show a technique that can potentially be used to localized turbine clutter. Next, modeling our turbines as wires, we analyzed the ISAR features of arrays of wind turbines. Finally, shadowing characteristics of arrays of turbines is studied.

7.2 FUTURE WORK

With new and more innovative turbine component designs, the form of wind turbines can be expected to rapidly change in the future. Therefore, the first possibility of extending this work is to analyze the features of the turbines with newer designs. In addition to the newer features, environmental effects, e.g. ground bounce, may also produce newer scattering features that may be very different from the features documented in this work. The JTF and ISAR signature characterization approach used in this work can be applied again to study the features of the new models.

Second, although we have made preliminary advances in introducing complexity in the shape of the blade in our turbine basis, the efficacy of the proposed models has yet to be tested on real or simulated data. The point scatterer model of the turbine blades has the potential to mimic any arbitrary shape given the exact shape of a turbine blade. Therefore, matching pursuit algorithm along with the complex blade shape shown in chapter 5 as our basis needs to be applied to triangular shaped blades that can be constructed in FEKO. Following that, the approach can be extended to more complex blade shapes.

The HF study at the moment is in very early stages. The blades were modeled as wires and assumed to be PEC. To extend this work, we first plan to introduce dielectric properties into the wires. This can be done by modeling the components using cylinders having the dielectric properties of the blades that are made of carbon fiber based material. Furthermore, the prediction of the features can be further improved by using realistic CAD models of the blades.

References

- [1] D. L. Sengupta and T. B. A. Senior, "Electromagnetic Interference to Television Reception Caused by Horizontal Axis Windmills," *Proc. IEEE*, vol. 67, pp. 1133-1142, Aug. 1979.
- [2] D. L. Sengupta and T. B. A. Senior, "Electromagnetic Interference from Wind Turbines," in *Wind Turbine Technology*, D. A. Spera, New York: ASME Press, 1994, pp. 447-486.
- [3] C. Salema and C. Fernandes, "Co-Sitting Criteria for Wind Turbine Generators and Transmitter Antennas," *Proc. Conftelle 1999 – II Conf. de Telecomunicacoes*, Sesimbra, Portugal, pp. 466-470, 1999.
- [4] C. Salema, C. Fernandes, and L. Fauro, "TV Interference from Wind Turbines," *Proc. 3rd Conference on Telecommunications*, Figueira da Foz, Portugal, pp. 47-51, 2001.
- [5] I. Angulo, J. Montalban, J. Canizo, Y. Wu, D. de la Vega, D. Guerra, P. Angueira, and A. Arrinda, "Emprical Doppler Characterization of Signals Scattered by Wind Turbines in the UHF Band under Near Field Conditions," *Int. Journal of Ant. and Propag.*, vol. 2013, Article ID 804690, 11 pages, 2013.
- [6] J. Hills, "Greta Valley Wind Farm—Compatibilty with Radio Services," Final Report to Meridian Energy Limited, 2009.
- [7] P. Tognolatti and A. Orlandi, "Analysis of the EMI Impact of an Array of Wind Generators on the Performances of Secondary Surveillance Radar System," *2008 Int. Symposium on Electromagnetic Compatibility-EMC Europe*, pp. 1-4, Hamburg, Sep. 2008.
- [8] F. Krug and B. Lewke, "Electromagnetic Interference on Large Wind Turbines," *Energies*, vol. 2, pp. 1118-1129, Nov. 2009.
- [9] *Special Evaluation Report to Assess Effect of Wind Turbine Farm on Air Route Surveillance Radar-4 at King Mountain, Texas*, USAF 84 RADES & FAA, May 30, 2002.
- [10] *Wind Turbines and Radar: Operational Experience and Mitigation Measures*, Spaven Consulting, Report to a Consortium of Wind Energy Companies, Dec. 2001.
- [11] J. J. Lemmon, J. E. Carroll, F. H. Sanders, D. Turner, "Assessment of the Effects of Wind Turbines on Air Traffic Control Radars," NTIA Technical Report TR-08-454 to the U. S. Department of Commerce, Jul. 2008.
- [12] *The Effects of Wind Turbine Farms on ATC RADARS*, Air Warfare Center, Royal Air Force, UK, May 10, 2005.
- [13] *Further Evidence of the Effects of Wind Turbine Farms on AD RADARS*, Air Warfare Center, Royal Air Force, UK, Aug. 12, 2005.

- [14] M. Brenner, "Wind Farm and Radar," The MITRE Corp., Report JSR-08-125 to the Dept. of Homeland Security, Jan. 2008.
- [15] Report of the Effect on Radar Performance of the Proposed Cape Wind Project and Advance Copy of USCG Findings and Mitigation, U. S. Department of the Interior Minerals Management Service, Jan. 2009.
- [16] The Effect of Windmills on Military Readiness, United States Department of Defense Report to the Congressional Defense Committees, 2006.
- [17] G. J. Poupart, "Wind Farms Impact on Radar Aviation Interests," QinetiQ Corp., Final Report to the Dept. of Trade and Industry, UK, Sept. 2003.
- [18] B. M. Kent, K. C. Hill, A. Buterbauch, G. Zelinski, R. Hawley, L. Cravens, T. Van, C. Vogel, and T. Coveyou, "Dynamic Radar Cross Section and Radar Doppler Measurements of Commercial General Electric Windmill Power Turbines," *IEEE Antennas Propagat. Mag.*, vol. 50, pp. 211-219, Apr. 2008.
- [19] B. M. Kent, A. Buterbaugh, K. C. Hill, G. Zelinski, R. Hawley, L. Cravens, T. Van, C. Vogel, and T. Coveyou, "Dynamic Radar Cross Section and Radar Doppler Measurements of Commercial General Electric Windmill Power Turbines Part 2 – Predicted and Measured Doppler Signatures," *Proc. 2007 AMTA Symposium*, St. Louis, MO, 2007.
- [20] K. C. Hill, G. Zelinski, T. Van, and C. Vogel, "Computational Electromagnetics (CEM) Prediction of a Windmill," *2007 Electromagnetics Code Consortium Annual Meeting*, May 2007.
- [21] *The Air Force Research Laboratory (AFRL) Mobile Diagnostics Laboratory (MDL) Wind Farm Turbine Measurements Fenner, NY*, Final Report, July 2006.
- [22] A. Theil, L. J. van Ewijk, "Radar Performance Degradation due to the Presence of Wind Turbines," *Proc. 2007 IEEE Radar Conference*, pp. 75-80, Boston, MA, 2007.
- [23] L. S. Rashid, A. K. Brown, "Impact Modelling of Wind Farms on Marine Navigational Radar," *Proc. 2007 IET Int. Conference on Radar Systems*, pp. 1-5, Edinburgh, UK, Oct. 2007.
- [24] C. Lute and W. Wieserman, "ASR-11 Radar Performance Assessment over a Wind Turbine Farm," *Proc. 2011 IEEE Radar Conference (RADAR)*, pp. 226-230, Kansas City, MO, May 2011.
- [25] A. Huuskonen, "OPERA Final Report," Finnish Meteor. Inst., Mar. 2007.
- [26] *Impact of Wind Turbines on Weather Radars*, OPERA II WP 1.8, 2006.
- [27] D. W. Burgess, T. Crum, and R. J. Vogt, "Impacts of Wind Farms on WSR-88D Operations," *24th Int. Conf. on Interactive Information Processing Systems (IIPS) for Meteorology, Oceanography, and Hydrology*, Amer. Meteor. Soc., Paper 6B.3, New Orleans, LA, 2008.
- [28] J. B. Sandifer, T. Crum, E. Ciardi, and R. Guenther, "A Way Forward: Wind Farm Weather Radar Coexistence," WINDPOWER 2009, Chicago, IL, May 2009.

- [29] L. Norin and G. Haase, "Doppler Weather Radars and Wind Turbines," in *Doppler Radar Observations-Weather Radar, Wind Profiler, Ionospheric Radar, and Other Advanced Applications*, J. Bech, Rijeka, InTech, 2012, pp. 333-354.
- [30] R. J. Vogt, T. D. Crum, W. Greenwood, E. J. Ciardi, R. G. Guenther, "New Criteria for Evaluating Wind Turbine Impacts on NEXRAD Radars," Preprints, *WINDPOWER 2011, American Wind Energy Association Conference and Exhibition*, Anaheim, CA, 2011.
- [31] K. Hood, S. Torres, and R. Palmer, "Automatic Detection of Wind Turbine Clutter for Weather Radars," *Journal of Atmospheric and Oceanic Technology*, vol. 27, pp. 1868-1880, May 2010.
- [32] G. Hutchinson and R. Miles, "The Protection of Weather Radar Networks. The UK Experience," *Proc. ERAD 2008-The Fifth European Conference on Radar in Meteorology and Hydrology*, pp. 1-5, Helsinki, 2008.
- [33] B. Gallardo-Hernando, J. M. Munoz-Ferreras, F. Perez-Martinez, and F. Aguado-Encabo, "Wind Turbine Clutter Observations and Theoretical Validation for Meteorological Radar Application," *IET Radar, Sonar and Navigation*, vol. 5, pp. 111-117, 2011.
- [34] G. Gopalakrishnan, "Surface Current Observations Using High Frequency Radar and Its Assimilation into the New York Harbor Observing and Prediction System," Ph.D. dissertation, Civil, Environmental, and Ocean Eng., Stevens Institute of Technology, Hoboken, NJ, 2008.
- [35] R. H. Stewart and J. W. Joy, "HF Radio Measurements of Surface Currents," *Deep-Sea Research*, vol. 21, pp. 1039-1049, 1974.
- [36] L. R. Wyatt, A. M. Robinson, and M. J. Howarth, "Wind Farm Impacts on HF Radar Current and Wave Measurements in Liverpool Bay," *Proc. 2011 IEEE Oceans*, pp. 1-3, Santander, June 2011.
- [37] C. C. Teague and D. E. Barrick, "Estimation of Wind Turbine Radar Signature at 13.5 MHz," *Proc. 2012 IEEE Oceans*, pp. 1-4, Oct. 2012.
- [38] H. E. Green, "Electromagnetic Backscattering from a Helicopter Rotor in the Decametric Wave Band Regime," *IEEE Trans. Antennas Propagat.*, vol. 42, pp. 501-509, Apr. 1994.
- [39] R. Bhalla and H. Ling, "A Fast Algorithm For Simulating Doppler Spectra of Targets With Rotating Parts Using the Shooting and Bouncing Ray Technique," *IEEE Trans. Antennas Propagat.*, vol. 46, pp. 1389-1391, Sept. 1998.
- [40] T. Thayaparan, S. Abrol, E. Riseborough, L. Stankovic, D. Lamothe, and G. Duff, "Analysis of Radar Micro-Doppler Signatures from Experimental Helicopter and Human Data," *IET Proc. Radar Sonar Navigat.*, vol. 1, pp. 289-299, Aug. 2007.
- [41] M. R. Bell, R. A. Grubbs, "JEM Modeling and Measurement for Radar Target Identification," *IEEE Transactions on Aerospace and Electronics Systems*, vol. 29, pp. 73-87, Aug. 2002.
- [42] P. Pouliguen, L. Lucas, Franck Muller, S. Quete, and C. Terret, "Calculation and Analysis of Electromagnetic Scattering by Helicopter Rotating Blades," *IEEE Transactions on Antennas and Propag.*, vol. 50, pp. 1396-1408, Oct. 2002.

- [43] R. Bhalla, H. Ling, S. Lee, D. J. Andersh, "Dynamic Simulation of Doppler Spectra of Targets with Rotating Parts," *Microwave and Opt. Tech. Lett.*, vol. 7, pp. 840-842, Dec. 1994.
- [44] A. Theil, M. W. Schouten, A. de Jong, "Radar and Wind Turbines: A Guide to Acceptance Criteria," *2010 IEEE Radar Conference*, pp. 1355-1361, Washington, DC, May 2010.
- [45] L. Rashid and A. Brown, "Partial Treatment of Wind Turbine Blades with Radar Absorbing Materials (RAM) for RCS Reduction," *Proc. 4th European Conference on Antennas and Propag.*, pp. 1-5, Apr. 2010.
- [46] L. S. Rashid, A. K. Brown, "Radar Cross-Section Analysis of Wind Turbine Blades with Radar Absorbing Materials," *Proc. 2011 European Radar Conference (EuRAD)*, pp. 97-100, Manchester, Oct. 2011.
- [47] J. Pinto, J. C. G. Matthews, and G. C. Sarno, "Stealth Technology for Wind Turbines," *IET Radar, Sonar & Navigation*, vol. 4, pp. 126-133, Feb. 2010.
- [48] J. J. McDonald, B. C. Brock, S. E. Allen, P. G. Clem, J. A. Paquette, W. E. Patitz, W. K. Miller, D. A. Calkins, and H. J. Loui, "Radar-Cross-Section Reduction of Wind Turbines (Part 1)," Sandia Report, Mar. 2012.
- [49] A. Tennant and B. Chambers, "Signature Management of Radar Returns from Wind Turbine Generators," *Smart Materials Structures*, vol. 15, pp. 468-472, Feb. 2006.
- [50] E. Aarholt and C. A. Jackson, "Wind Farm Gapfiller Concept Solution," *Proc. 7th European Radar Conference*, pp. 236-239, Paris, Oct. 2010.
- [51] M. Brenner, S. Cazares, M. J. Cornwall, F. Dyson, D. Eardley, P. Horowitz, D. Long, J. Sullivan, J. Vesecky, P. J. Weinberger, "Wind Farms and Radar," The Mitre Corp., Jan. 2008.
- [52] B. M. Isom, R. D. Palmer, G. S. Secrest, R. D. Rhoton, D. Saxion, T. L. Allmon, J. Reed, T. Crum, and R. Vogt, "Detailed Observations of Wind Turbine Clutter with Scanning Weather Radars," *Journal of Atmospheric and Oceanic Technology*, vol. 26, pp. 894-910, May 2009.
- [53] M. M. Butler and D. A. Johnson, "Feasibility of Mitigating the Effects of Windfarms on Primary Radar," Alenia Marconi Systems Limited, 2003.
- [54] A. Tennant and B. Chambers, "Radar Signature Control of Wind Turbine Generators," *IEEE Antennas Propagat. Soc. Int. Symp.*, pp. 489-492, Washington, DC, July 2005.
- [55] J. C. G. Matthews, J. Pinto, and C. Sarno, "Stealth Solutions to Solve the Radar-Wind Farm Interaction Problem," *2007 Loughborough Antennas Propagat. Conf.*, pp. 101-104, Loughborough, UK, Apr. 2007.
- [56] K. V. Mishra and V. Chandrasekar, "Signal Analysis and Modeling of Wind Turbine Clutter in Weather, IGARSS, pp. 3561-3564, 2010.
- [57] L. Sergey, O. Hubbard, Z. Ding, H. Ghadaki, J. Wang, and T. Ponsford, "Advanced Mitigating Techniques to Remove the Effects of Wind Turbines and Wind Farms on Primary Surveillance Radars," *Proc. 2008 Radar Conference*, pp. 1-6, Rome, May 2008.

- [58] J. Perry and A. Biss, "Wind Farm Clutter Mitigation in Air Surveillance Radar," *Proc. 2007 IEEE Radar Conference*, pp. 93-98, Boston, MA, Apr. 2007.
- [59] B. M. Isom, R. D. Palmer, G. S. Secrest, R. D. Rhoton, D. Saxion, J. L. Winslow, J. Reed, T. Crum, and R. Vogt, "Characterization and Mitigation of Wind Turbine Clutter on the WSR-88D Network," *Proc. 33rd Conference on Radar Meteorology*, paper 8B.8, Aug. 2007.
- [60] R. D. Palmer, K. D. Le, B. Isom, "Wind Turbine Clutter Mitigation Using Fully Adaptive Arrays," *Proc. 5th European Radar Conference*, pp. 356-359, Oct. 2008.
- [61] F. Nai, R. D. Palmer, and S. M. Torres, "Range-Doppler Domain Signal Processing to Mitigate Wind Turbine Clutter," *Proc. 2011 IEEE Radar Conference*, pp. 841-845, Kansas City, MO, May 2011.
- [62] Y. F. Lok, A. Palevsky, and J. Wang, "Simulation of Radar Signal on Wind Turbine," *IEEE Aerospace and Electronic Systems Mag.*, vol. 26, pp. 39-42, Aug. 2011.
- [63] A. Naqvi, S. Yang, and H. Ling, "Investigation of Doppler Features from Wind Turbine Scattering," *IEEE Antennas Wireless Propag. Lett.*, vol. 9, pp. 485-488, 2010.
- [64] A. Naqvi, N. Whiteloni, H. Ling, "Doppler Features of Wind Turbines in the Presence of Ground," *Progress In Electromagnetics Research Letters*, vol. 35, 1-10, 2012.
- [65] A. Naqvi and H. Ling, "Time Frequency and ISAR Characteristics of Wind Turbines with Higher Order Motions," *Progress In Electromagnetics Research*, vol. 143, 331-347, 2013.
- [66] A. Naqvi and H. Ling, "Signal Filtering Technique to Remove Doppler Clutter Caused by Wind Turbines," *Microwave Opt. Tech. Lett.*, vol. 54, pp. 1455-1460, 2012.
- [67] A. Naqvi and H. Ling, "A Study of Radar Features of Wind Turbines in the HF Band," *Progress In Electromagnetics Research*, vol. 143, 331-347, 2013.
- [68] G. Greving, W. Biermann, R. Mundt, "Wind Turbines as Distorting Scattering Objects for Radar-Clutter Aspects and Visibility," in *Proc. Int. Radar Symp. 2010*, Vilnius, Lithuania, June 2010.
- [69] G. Greving, W. Biermann, R. Mundt, "On the Relevance of the Measured or Calculated RCS for Objects on the Ground – Case Wind Turbines," in *Proc. 3rd European Conf. Antennas Propagat.*, Berlin, DE, 2009, pp. 2216-2220.
- [70] S. S. Ram, R. Bhalla, and H. Ling, "Simulation of Human Radar Signatures in Presence of Ground," in *IEEE Antennas Propagat. Soc. Int. Symp. Dig.*, Charleston, June 2009.
- [71] *AHILO: computer code for solving electromagnetic problems*. Web. Jan. 12, 2012. <http://www.ahilo.net/AHILO_web/Overview.html>.
- [72] C. A. Balanis. *Advanced Engineering Electromagnetics*. New Jersey: Wiley, 1989, pp. 314-325.

- [73] X. Wang, C.-F. Wang, Y.-B. Gan, and L.-W. Li, "Electromagnetic Scattering from Circular Target Above or Below Rough Surface," *Progress Electromagnetics Research*, vol. 40, pp. 207–227, 2003.
- [74] L. Vaitilingom and A. Khenchaf, "Radar Cross Sections of Sea and Ground Clutter Estimated by Two Scale Model and Small Slope Approximation in HF-VHF Bands," *Progress Electromagnetics Research*, vol. 29, pp. 311-338, 2011.
- [75] N. Whiteloni, S. Yang, and H. Ling, "Application of near-field to far-field transformation to Doppler features from wind turbine scattering," *IEEE Trans. Antennas Propagat.*, vol. 60, pp. 1660-1665, Mar. 2012.
- [76] V.C. Chen, F. Li, S.-S. Ho and H. Wechsler, "Analysis of micro-Doppler Signatures," *IEE Proc.-Radar Sonar Navig.*, vol. 150, Aug. 2003.
- [77] S. G. Mallat and Z. Zhang, "Matching Pursuits with Time-Frequency Dictionaries," *IEEE Trans. Sig. Proc.*, vol. 41, pp. 3397-3415, 1993.
- [78] Y. Wang, H. Ling, and V. C. Chen, "Application of Adaptive Joint Time-Frequency Processing to ISAR Image Enhancement and Doppler Feature Extraction for Targets with Rotating Parts," *Proc. SPIE-Int. Soc. Optic. Eng.*, vol. 3462, pp. 156–163, 1998.
- [79] J. Li and H. Ling, "Application of Adaptive Chirplet Representation for ISAR Feature Extraction from Targets with Rotating Parts," *IEE Proc.-Radar Sonar Navigat.*, vol. 150, pp. 284-291, Aug. 2003.
- [80] L. C. Trintinalia and H. Ling, "Joint Time-Frequency ISAR Using Adaptive Processing," *IEEE Trans. Antennas Propag.*, vol. 45, pp. 221-227, 1997.
- [81] L. C. Trintinalia, R. Bhalla, and H. Ling, "Scattering Center Parameterization of Wide-Angle Backscattered data Using Adaptive Gaussian Representation," *IEEE Trans. Antennas Propag.*, vol. 45, pp. 1664-1668, 1997.
- [82] Y. Wang and H. Ling, "Efficient Radar Signature Prediction Using a Frequency-Aspect Interpolation Technique Based on Adaptive Feature Extraction," *IEEE Trans. Antennas Propag.*, vol. 50, pp. 122-131, 2002.
- [83] J. Li and H. Ling, "ISAR Feature Extraction from Non-rigid Body Targets using Adaptive Chirplet Signal Representation," *IEE Proc. – Radar, Sonar, Navigation*, vol. 150, pp. 284-291, 2003.
- [84] FEKO version 6.2, Stellenbosch, South Africa: EM Software & Systems Inc. 2012.
- [85] J. Jonkman, S. Butterfield, W. Musial, and G. Scott, "Definition of a 5-MW Reference Wind Turbine for Offshore System Development," National Renewable Energy Laboratory, Tech. Rept. NREL/TP-500-38060, Feb. 2009.
- [86] S.-T. Yang and H. Ling, "Electromagnetic Simulation of the Near-Field Distribution Around a Wind Farm," *Int. J. Antennas Propagat.*, vol. 2013, Article ID 105071, 9 pages, 2013.
- [87] Z. Dang, J. Wu, H. Xu, S. Yao, and M. Jiang, "Dielectric Properties of Upright Carbon Fiber Filled Poly (Vinylidene Fluoride) Composite with Low Percolation

Threshold and Weak Temperature Dependence,” *App. Phys. Lett.*, vol. 91, pp. 072912 1-3, 2007.

Vita

Aale Naqvi completed his bachelors degree in physics from University of Texas at Arlington with a minor in electrical engineering in 2008. He enrolled in the university of Texas at Austin and completed his masters degree in electrical engineering in 2010. He has since been working towards completing his doctorate degree in electrical engineering.

Permanent email: aalenaqvi@yahoo.com

This dissertation was typed by the author.